2D structurally-constrained CSEM inversion and seismic modelling for anisotropic media

विद्या वाचस्पति की
उपाधि की अपेक्षाओं की आंशिक पूर्ति में प्रस्तुत शोध प्रबंध

A thesis submitted in partial fulfillment of the requirements of the degree of Doctor of Philosophy

द्वारा
इकतेश चौहान
By
Iktesh Chauhan

पंजीकरण सं. / Registration No.: **20193630**

शोध प्रबंध पर्यवेक्षक / Thesis Supervisor
Dr. Rahul Dehiya

भारतीय विज्ञान शिक्षा एवं अनुसंधान संस्थान पुणे
INDIAN INSTITUTE OF SCIENCE EDUCATION AND RESEARCH PUNE
2024

Certificate

Certified that the work incorporated in this thesis entitled '2D structurally-constrained CSEM inversion and seismic modelling for anisotropic media' submitted by Iktesh Chauhan, was carried out by the candidate, under my supervision. The work presented here or any part of it has not been included in any other thesis submitted previously for the award of any degree or diploma from any other University or institution.

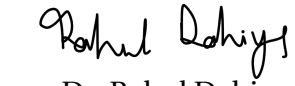

Dr. Rahul Dehiya
Thesis Supervisor
Indian Institute of Science Education and Resaerch
Pune, Maharashtra

Date: 15/08/2024

Declaration by Student

Name of Student: Iktesh Chauhan

Reg. No.: 20193630

Thesis Supervisor(s): Dr. Rahul Dehiya

Department: Earth and Climate Science department

Date of joining program: 01/01/2019

Date of Pre-Synopsis Seminar: 16/07/2024

Title of Thesis: 2D structurally constrained CSEM inversion and seismic modelling for anisotropic media

I declare that this written submission represents my idea in my own words and where others' ideas have been included; I have adequately cited and referenced the original sources. I declare that I have acknowledged collaborative work and discussions wherever such work has been included. I also declare that I have adhered to all principles of academic honesty and integrity and have not misrepresented or fabricated or falsified any idea/data/fact/source in my submission. I understand that violation of the above will be cause for disciplinary action by the Institute and can also evoke penal action from the sources which have thus not been properly cited or from whom proper permission has not been taken when needed.

The work reported in this thesis is the original work done by me under the guidance of

Dr. Rahul Dehiya

Date: 20/08/2024

iktesh chauhan

Signature of the student

To

The most beautiful thing in the world that is everyone pure soul and character

Abstract

Inverse modelling is an ill-posed problem, and the regularisation technique is used to solve the inverse problem by biasing the solution with prior information. In the absence of prior information about the model, a constraint that seeks the smoothest model is enforced. However, a regularisation scheme that imposes information obtained from other geophysical methods has the potential to produce a more realistic model with sharp boundaries of anomalies. This thesis presents a study on the development of a structurally constrained inversion algorithm of controlled-source electromagnetic (CSEM) data. We have devised an efficient space-domain forward and gradient computation algorithm for CSEM data. The space-domain simulation is achieved by imposing novel boundary conditions on the plane perpendicular to the strike direction that passes through the transmitter position. In this study, the boundary conditions for various transmitter types are derived using the symmetric/antisymmetric character of the electric and magnetic fields. For all the other boundaries, a homogenous Dirichlet boundary condition is applied. The devised strategy facilitates efficient computation as one needs to discretise the space only on the side of the source position along the strike direction. Furthermore, the benchmarking experiment reveals that only six to eight grids are sufficient for discretisation in the strike direction for the accuracy required in geophysical data analysis.

A Gauss-Newton optimisation-based inverse modelling algorithm is developed for two-dimensional (2D) CSEM data inversion by employing the proposed forward modelling algorithm. The algorithm can perform inversion for the vertical transverse isotropy (VTI) subsurface model. The adjoint approach is used for the computation of the Jacobian matrix. A Gauss-Newton method is employed to calculate updated model parameters where the Hessian matrix is solved using a conjugate gradient solver. The developed algorithm is tested for synthetic and real-field CSEM data, and the inversion experiment agrees with the benchmarking of forward modelling, indicating that around eight are sufficient for discretisation in the strike direction. The comparison of the proposed algorithm with a published algorithm shows that our algorithm is at least one order faster in terms of computation time and requires less memory.

A structurally constrained 2D inversion algorithm for CSEM data inversion is developed that incorporates structural information using a cross-gradient method. The cross-gradient method enforces the structural similarity between the two models by optimising the 2-norm of cross-product of spatial gradients of both models. Using the developed algorithm, a detailed analysis is carried out to test the advantages and limitations of the structurally constrained inversion based on the cross-gradient method. The structurally constrained inversion improves the inverted model but does not produce a sharp boundary due to the smoothing operator employed in our code for regularisation.

We also developed an algorithm to simulate a 2D frequency-domain acoustic wave response in a transversely isotropic medium with a tilted symmetry axis. The algorithm employs a support-operator finite-difference method for modelling. This method constructs a nine-point stencil finite-difference scheme for second-order elliptic equations for generalised anisotropic physical properties. The modelling scheme is benchmarked using the analytical responses of the half-space model for isotropic and anisotropic media.

Acknowledgements

The divine blessings and unwavering support of my father, Bachan Singh Chauhan, my Mother, Satlesh Chauhan, my sister, Vartika Chauhan, and one of my best friends, Deepanshu Chauhan, empowered me to overcome all obstacles encountered during my research work.

I am deeply grateful to Dr. Rahul Dehiya, my research supervisor, for his unwavering support, invaluable guidance, and continuous encouragement throughout this endeavor. His scientific acumen, balanced approach, and discerning critique have significantly contributed to my growth as a researcher, aiding in developing and refining my ideas and research.

I am pleased to express my sincere thanks to Dr. Gyana Ranjan Tripathi, Head, Department of Earth and Climate Science, Indian Institute of Science Education and Research (IISER), Pune, for providing the necessary amenities required for my research work.

I would also like to express my gratitude to my advisory committee, Prof. Bharat Shekhar and Dr. Arjun Dutta, for their invaluable comments and suggestions. Their guidance has contributed significantly to the enhancement of my skills and the improvement of my research work. I am thankful to the Indian Institute of Science Education and Research (IISER), Pune, for their financial assistance. I want to express my gratitude and extend my thanks to all the administrative staff of the Department of Earth and Climate Science, IISER, Pune.

I would like to offer special thanks to my Grandfather, Late Rampal Singh, and my Grandmother, Somti Devi.

I would like to express my deepest gratitude to my friends, Suraj Lakhchaura and Dhruv Khatri, for always being there and bearing with me during the good and bad times of my academic career.

Special thanks to my seniors, Dr. Deepak Suryavanshi, Dipak Kumar Chaubey, and my lab members for being with me in every difficult situation.

Last but not least, I am grateful to all my silent helpers who have supported me at various stages of difficulties during my research work, whether directly or indirectly.

Table of contents

List of figures

Chapter 1

Introduction

1.1 Motivation

In the realm of geophysical exploration, achieving a precise and comprehensive understanding of the subsurface is paramount. It involves measuring various geophysical data types, which are often sparse due to the difficulty of installing sensors in solid parts of the Earth. The observed geophysical data is processed and analysed using techniques such as inverse modelling to obtain the physical properties of the subsurface. Accurately knowing these physical properties affects the success of identifying and extracting valuable resources such as hydrocarbons and ores. Individual geophysical methods, while effective, often have limitations in accurately capturing the complexity of the Earth's subsurface due to the sparsity of data, resolution of the geophysical method and the ill-posed nature of inverse modelling. The joint analysis of various geophysical data has great potential to add value to subsurface imaging. This thesis aimed to develop algorithms for joint analysis of seismic and Controlled Source Electromagnetic (CSEM) data. Such joint analyses are considered to emerge as a game-changer, offering a synergistic approach that leverages the strengths of both techniques to provide superior imaging and characterisation of subsurface structures. For example, seismic data has long been the cornerstone of subsurface imaging due to its high resolution and detailed insights into geological formations. Seismic methods predominantly measure the elastic properties of the subsurface, which depend on both lithology and fluid content. However, one significant challenge in seismic interpretation is the difficulty in determining fluid saturation, leading to ambiguities and uncertainties in reservoir characterisation; consequently, distinguishing between commercial and non-commercial hydrocarbon reserves becomes challenging. On the other hand, CSEM methods are sensitive to the electrical resistivity of the subsurface, which varies significantly with hydrocarbon saturation. While CSEM data can provide

clear indications of resistivity anomalies associated with hydrocarbon deposits, it generally offers lower spatial resolution than seismic data and may struggle with complex geological settings. Sub-basalt and sub-salt are other areas where integrating seismic and CSEM data can elevate the subsurface imaging significantly. Furthermore, combining seismic and CSEM data is advantageous in subsurface CO2 sequestration projects, including during the monitoring phase. Nevertheless, by integrating seismic and CSEM data through joint inversion, we can exploit the complementary nature of these methods to overcome their individual limitations. Joint inversion combines the high-resolution structural information from seismic data with the fluid sensitivity of CSEM data, leading to a more accurate and detailed subsurface model. In an era striving for sustainable energy solutions, such advancements in exploration technologies play a pivotal role in ensuring efficient and sustainable resource utilisation and meeting energy demands while minimising environmental impact.

To highlight the contribution of this thesis, first, a detailed review of CSEM and seismic methods with emphasis on forward and inverse modelling is presented. Subsequently, the literature survey of joint analysis, mainly the joint inversion of these methods, is discussed. Finally, the thesis's objective and contribution are presented at the end of this chapter.

1.2 Controlled source electromagnetic method

The CSEM method is a geophysical technique (Constable, 2010; Cox, 1981) used primarily in subsurface imaging up to 3 to 4 km. It has been used successfully for hydrocarbon exploration (Constable, 2010), offshore freshwater mapping (Evans, 2007), gas hydrate studies (Schwalenberg et al., 2010), CO2 sequestration (Bhuyian et al., 2012) and mineral exploration (Constable, 2010). The CSEM method involves generating electromagnetic fields using a controlled source and measuring the resulting electromagnetic (EM) response at various distances from the source. The CSEM method can be applied in the time or frequency domain. The frequency domain method suffers from the airwave problem (Amundsen et al., 2006). Consequently, various techniques have been developed to eliminate the airwave signal from seafloor CSEM data (Amundsen et al., 2006). Insights from land-based EM surveys indicate that addressing the airwave issue is most effectively achieved using time-domain EM methods rather than frequency-domain approaches (Weiss, 2007). However, the frequency domain methods are most effective in deep water marine environments (>300 m) where the conductive marine water suppresses the airwave significantly since the transmitter and receives are placed at/near the sea floor. The typical frequency range in marine CSEM experiments is 0.01 Hz to 10 Hz. The EM

wave propagated as a diffusion regime in the earth's subsurface for this frequency range. The primary EM field from the source induces secondary EM fields in the surrounding medium. The transmitter is towed as close to the sea floor as possible (generally 30 to 50 m). The EM is detected by receivers placed on the seafloor. Since the recorded EM field also contains the secondary components, the observed data has the sensitivity of the subsurface resistivity around the transmitter and receivers. Therefore, geophysicists can infer the resistivity distribution within the subsurface by analysing the recorded data, providing valuable information about its composition and structure. However, the data must be transformed into the resistivity model to obtain the subsurface image, which is achieved by the inverse modelling of the observed data. Inverse modelling is a data fitting technique which requires a forward modelling algorithm for data simulation.

1.2.1 CSEM forward modelling

The forward modelling of CSEM data involves solving Maxwell's equations, which govern the behaviour of electromagnetic fields in the subsurface. The Maxwell's equations in the time domain in a source-free media can be written as

$$\nabla \cdot \mathbf{D} = 0 \quad \text{(Gauss's Law for Electricity)} \tag{1.1}$$

$$\nabla \cdot \mathbf{B} = 0 \quad \text{(Gauss's Law for Magnetism)} \tag{1.2}$$

$$\nabla \times \mathbf{E} = -\frac{\partial \mathbf{B}}{\partial t} \quad \text{(Faraday's Law)} \tag{1.3}$$

$$\nabla \times \mathbf{H} = \sigma \mathbf{E} + \frac{\partial \mathbf{D}}{\partial t} \quad \text{(modified Ampère's Law)}, \tag{1.4}$$

where, **E** is the electric field, **B** is the magnetic field, **H** is the magnetic field intensity, **D** is the electric displacement field and σ is electrical conductivity. For a complex media, an analytical solution of the above equation is not attainable. Therefore, numerical methods are used to solve these equations for the forward modelling of CSEM data.

The forward modelling of EM data aims to solve Maxwell's equation to simulate the response of the subsurface accurately and efficiently. Maxwell's equations may be solved in the frequency or time domains depending on the geophysical method or due to computational considerations. Maxwell's equations can be solved simultaneously for both the electric and magnetic fields, where one has to solve the first-order partial differential equation (PDE). Alternatively, a second-order PDE (Helmholtz equation) can be derived

using Maxwell's equations in terms of either the electric field or the magnetic field. The advantage of working with the Helmholtz equation is that the number of unknowns becomes half compared to the first approach. Most studies prefer to work with the Helmholtz equation expressed for the electric field for frequency domain simulation. Irrespective of the approach, the PDE must be solved using numerical techniques. All the numerical methods involve discretizing the subsurface model, and the solution is obtained at the discrete nodes within the computation domain. Since the modelling domain is very small compared to the earth, except for global sounding, the computation domain needs to be expressed as an unbounded region. Consequently, absorbing boundary conditions are applied on all sides of the computation domain. Since low-frequency EM propagation is a diffusion process and, the field decays as it travels into a finite conductivity medium. Therefore, boundary conditions are applied by padding a highly sparse grid on all sides of the modelling domain such that the field at the boundary can be approximated with a known field. Some studies have also applied perfectly matched layer boundary conditions for EM simulation. In the case of controlled sources, the source term needs to be handled carefully, as the EM fields are undefined at the source position. A Dirac delta defines the source term; therefore, an approximate Dirac delta function can be used to address the source singularity. However, such an approach requires very fine discretization around the receiver position. Another technique is primary/secondary field decomposition, which can handle source singularity effectively. However, it requires an efficient computation of the primary field, which may become challenging if the transmitter is in contact with a rugged topography. The choice of the strategy to manage source singularity also impacts the choice of a numerical method to be used for forward modelling. Several numerical methods have been employed for EM simulation, delivering reasonable accuracy for complex geological settings. Some of the most used numerical methods are:

1. **Finite Element Method:**
   The Finite Element Method (FEM) in EM modeling involves discretizing the computational domain into small elements to solve Maxwell's equations. It transforms these equations into a weak form by integrating them over each element. The finite element method is highly effective in handling irregular geometries and varying resistivity contrasts, making it a popular choice for CSEM forward modelling. da Silva et al. (2012) developed a finite element algorithm that he also used for the 3D CSEM inversion algorithm. Cai et al. (2017) developed a 3D anisotropic CSEM inversion algorithm using an edge-based finite element method. Kong et al. (2008) solve a 2.5D FEM approach for marine CSEM applications in layered anisotropic media, utilizing delta sources to solve the governing PDEs. An open-source, parallel

Python tool PETGEM for efficient and precise 3D CSEM modelling was developed by Castillo-Reyes et al. (2018).

2. **The Finite Difference Method:**
   The Finite Difference Method (FDM) is a widely adopted approach for tackling Maxwell's equations in geophysical modelling. It involves approximating the differential operator using difference formulas. The staggered grid concept introduced by Yee (1966) is employed, which led to improved accuracy. This method strategically defines electric fields at the edge centre of cells and magnetic fields at the cell centre or vice versa, resulting in a sparse, symmetric, and non-hermitian system matrix characterized by complex diagonal elements. FDM's notable advantage lies in its simplicity of implementation, which has spurred the development of various forward modelling algorithms for solving EM problems (Sasaki, 1999; Siripunvaraporn et al., 2002; Smith, 1996; Streich, 2009). A 3D Magnetotelluric (MT) modelling scheme, conserving electric current and magnetic flux on a staggered grid, was developed by Fomenko and Mogi (2002). Bergmann et al. (1996) solved Maxwell's equation for ground penetrating radar using the staggered grid finite difference method. Lampe et al. (2003) developed a finite-difference time-domain simulation tool specifically designed for the antennas used in ground-penetrating radar systems. Mackie et al. (1994) designed a finite difference algorithm, employing the minimum residual relaxation technique, to calculate the magnetotelluric response of various models. A radiation boundary-based FDM algorithm is developed for CSEM (Dehiya, 2021) and MT (Singh and Dehiya, 2022) data simulation.

3. **Integral Equation Method (IEM):**
   Integral equation methods (IEM) are constructed by writing Maxwell's equations in integral form with matrix Green's functions by creating so-called secondary or scattering sources. Because Maxwell's equations are linear in the source, the electric and magnetic fields can be written as sums of background and scattered fields. The background model distribution of the conductivity must be taken such that the electric and magnetic fields can be computed quickly and accurately everywhere in space. Several developers have utilized the IEM for 3D modelling purposes (Avdeev et al., 2002; Gribenko et al., 2010; Gribenko and Zhdanov, 2007).

Once the EM fields are computed at all the nodal positions, the next step is to calculate the response at the receiver locations. The EM responses are interpolated and transformed into the same form as the observed data. For example, if the Helmholtz equation is solved for the electric field and the observations are magnetic fields, the magnetic field response

at each observation position is calculated by transforming the electric field into the magnetic field using Faraday's law. Since some components may be discontinued at the observation position, the interpolation must be performed by considering discontinuity. For example, in marine CSEM, the normal component to the seafloor of the electric field is discontinuers at the observation position (Ward et al., 1988).

1.2.2 CSEM Inversion

Inverse modelling aims to search for a model that fits the data within a threshold which is mainly governed by the noise in the data. It is an ill-posed problem, making it difficult to solve. Specifically, the EM data inversion is a non-linear inverse problem. Various inversion techniques have been developed to address the challenges encountered by EM data inversion. Broadly, this technique can be divided into two categories: stochastic and deterministic inversion algorithms. Stochastic inversion represents a random walk into model space in search of a model that fits data. One of the useful random search methods is Markov Chain Monte Carlo (MCMC), which has been applied to EM data analysis (Malinverno, 2002; Minsley, 2011). The Bayesian inversion is considered the most robust in a class of stochastic inversion, which provides a probability distribution function (pdf), not just a model. Consequently, the evaluated pdf can be used to obtain useful characteristics of the model, including the assessment of model uncertainties and generating multiple possible solutions. Therefore, such inversion algorithms provide valuable insights into the reliability and variability of the inversion results, aiding in the interpretation of complex subsurface features (Sambridge and Mosegaard, 2002). However, in Bayesian inversion, the probabilistic approach necessitates the evaluation of numerous probable models to evaluate the posterior distribution correctly. This requires repeatedly solving the forward problem for each model iteration. Consequently, fast computation is crucial to make this process feasible within a reasonable time frame, ensuring that the inversion results are obtained timely and trustworthy (Wu et al., 2023). Efficient forward CSEM computation allows for the exploration of a large model space, leading to more robust and comprehensive probabilistic interpretations. Due to the high computation demand, the Bayesian inversion has not been used extensively, particularly for 2D and 3D inversion.

On the other hand, deterministic inversion requires much less computation time than Bayesian inversion. The EM deterministic inversion is achieved by linearizing the non-linear problem around a model, and most of the algorithms converge to the nearest minima (Tarantola, 2005). Therefore, the global minimum is only attainable if the initial model is in the neighborhood of the initial model. Thus, the initial resistivity model

needs to be derived from geological knowledge, preliminary data, or reasonable assumptions about the subsurface. The iterative nature of EM inversion, combined with the need for accurate forward modelling and sophisticated numerical techniques, makes it a computationally demanding task. However, advancements in computational power and algorithms have significantly enhanced the efficiency and effectiveness of CSEM inversion. High-performance computing and parallel processing allow for the handling of large-scale models and extensive datasets, enabling detailed imaging of the subsurface (Cai et al., 2022; Liu and Yin, 2016). These schemes optimize an objective function that involves minimizing the 2-norm misfit between observed and predicted data for the current model. Regularization techniques are essential for stabilizing the inversion process and mitigating the effects of noise and non-uniqueness in the data. Common regularization methods include Tikhonov regularization and total variation regularization, which impose additional constraints on the model to promote smoothness or sparseness. These constraints help to ensure that the inversion results are geologically plausible and not overly influenced by noise in the data (Tarantola, 2005). The gradient of the objective function is used to update the model. Therefore, the gradient calculation is required for a model update at each iteration. The steepest descent method updates the model in the reverse direction of the gradient that points to a maximum reduction of the objective function at the current position. The line search approach is used to calculate the step length for the model update. However, the steepest descent shows very slow convergence in case of an ill-conditioned problem, which is generally the case of EM inversion. Therefore, the non-linear conjugate gradient algorithm is preferred for EM inversion, which is more efficient than the steepest descent technique. In this method, a maximum correction is applied in a direction. Therefore, this algorithm is assumed to be cover in the maximum N state in the case of N-dimensional model space. However, in practice, many few updates are required as problems need to be solved up to a certain accuracy. Furthermore, the clustering of singular values drove significantly faster convergence. Therefore, the preconditioned conjugate gradient methods have also been developed for EM inversion. He et al. (2010) used a non-linear conjugate-gradient method for mapping the reservoir of the Qaidan basin (China) based on resistivity and induced polarization derived from continuous 3D magnetotelluric profiling. There are algorithms which use the non-linear conjugate gradient method for magnetotelluric inversion (He et al., 2010; Rodi and Mackie, 2001). Sasaki (2001) employed the Incomplete Cholesky biconjugate gradient (ICBCG) method in order to create a comprehensive 3-D inversion algorithm for electromagnetic data.

Including the curvature information in the gradient-based method can speed up the convergence significantly. Consequently, the Newton optimization-based methods can solve the optimization problem in very few iterations. However, it requires the calculation of the Hessian matrix, which is a computationally intensive task. In the Gauss-Newton method, the Hessian is approximated by the Jacobian matrix. The Jacobian matrix includes the derivative of all simulated data points with respect to each model parameter as its elements. Gauss-Newton method has been employed by several researchers for CSEM (Dehiya, 2024; Wang et al., 2018) and MT (Nádasi et al., 2022) inversion. The research conducted by Günther et al. (2006) involved the application of a Gauss-Newton method with inexact line search to effectively model the data within error constraints, leading to the creation of a 3D modelling and inversion algorithm for DC resistivity data. A practical algorithm for generating smooth models developed by Constable et al. (1987) is generally known as Occam inversion, which is analogous to the Gauss-Newton method. deGroot Hedlin and Constable (1990) used Occam's inversion to generate a smooth, 2D model for magnetotelluric data. Siripunvaraporn and Egbert (2000) and Siripunvaraporn et al. (2005) present data space OCCAM'S inversion scheme for 2D and 3D magnetotelluric data, respectively. Another variant of Newton's method is the quasi-Newton algorithm, in which the inverse of the Hessian matrix is computed using the information from the previous iterations. It reduces the computation per iteration substantially, but the convergence rate is less than the Gauss-Newton method. Haber (2004) discussed the Quasi-Newton methods for large-scale electromagnetic inverse problems. The three-dimensional magnetotelluric inversion algorithm developed by Avdeev and Avdeeva (2009) employs a limited-memory quasi-Newton optimization technique, which uses information from only the last few iterations for computing the inverse Hessian matrix.

1.3 Seismic method

The seismic method stands as one of the fundamental techniques in geophysical exploration, providing valuable insights into the subsurface structure of the Earth. It relies on the propagation of seismic waves generated by artificial sources or natural phenomena, such as earthquakes, and their subsequent detection through sensitive instruments called seismometers. By analyzing the characteristics of these seismic waves as they travel through different geological layers, researchers can infer crucial information about subsurface properties like rock types, layer thicknesses, and structural features.

1.3.1 Theory of seismic wave equation

The linearized set of partial differential equations that govern the motion of homogeneous elastic solids Payton (1983) are :

Force-Equilibrium equation:

$$\frac{\partial \tau_{ji}}{\partial x_j} + \rho f_i = \rho \frac{\partial^2 u_i}{\partial t^2}, \tag{1.5}$$

momentum-equilibrium equation:

$$\tau_{ij} = \tau_{ji}, \tag{1.6}$$

Strain-displacement relation:

$$e_{ij} = \frac{1}{2}(\frac{\partial u_i}{\partial x_j} + \frac{\partial u_j}{\partial x_i}), \tag{1.7}$$

Stess-strain relation:

$$\tau_{ij} = c_{ijkl} e_{kl}. \tag{1.8}$$

The equations presented above, applicable within the solid's interior, are expressed in terms of a stationary Cartesian reference frame with t representing time. τ_{ij} and e_{ij}denote the Cartesian components of the stress and strain tensors, respectively, while u_i denotes the components of the displacement vector. The components of the body force vector, per unit mass, are f_i and ρ is the constant mass density of the solid. The fourth order tensor of the elasticity's c_{ijkl} satisfy the (Green) symmetry conditions

$$c_{ijkl} = c_{jikl} = c_{klij}, \tag{1.9}$$

so, there are 21 independent constants needed to describe the stress-strain relations for a general anisotropic elastic solid. Equations (1.5)-(1.8) constitute a set of 15 equations for the 15 unknowns τ_{ij}, e_{ij} and u_i. Since the equations are linear with constant coefficients, it is an easy matter to reduce this set to 3 equations for the 3 components of the displacement vector u_i,

$$c_{ijkl} \frac{\partial^2 u_k}{\partial x_l \partial x_j} + \rho f_i = \rho \frac{\partial^2 u_i}{\partial t^2}, \tag{1.10}$$

1.3.2 Anisotropic Acoustic wave equation

In the case of an isotropic solid, the c_{ijkl} tensor is constrained to satisfy;

$$c_{ijkl} = \lambda\delta_{ij}\delta_{kl} + \mu(\delta_{ik}\delta_{jl} + \delta_{il}\delta jk), \tag{1.11}$$

if the medium is isotropic, the seismic wave propagates equally fast in all directions. The most straightforward anisotropic symmetry system in the physical realm is axisymmetric anisotropy, commonly called transverse isotropy. A transversely isotropic medium can be subdivided into three categories: one with a vertical symmetry axis, another with a horizontal symmetry axis, and a third with a tilted symmetry axis. The axis of symmetry is an axis of rotational invariance, about which the formation may be rotated by any amount and still leave the material indistinguishable from what it was before (Ikelle and Amundsen, 2018). The direction of symmetry is typically linked to either gravity or regional stress. If gravity plays the primary role, the symmetry direction is vertical, resulting in VTI (transverse isotropy with a vertical symmetry axis). When regional stress is the dominant factor, the symmetry axis may be horizontal, leading to HTI (transverse isotropy with a horizontal symmetry axis). Alternatively, the symmetry axis can be tilted concerning the vertical and horizontal axes, resulting in TTI(transverse isotropy with a tilted symmetry axis). For a detailed formulation of the c_{ijkl} expression about transverse isotropic media, I recommend the book Introduction to Petroleum Seismology written by Ikelle and Amundsen (2018).

Alkhalifah (1998) first derived the anisotropic acoustic wave equation, that is, simple dispersion relations, which is the vertical slowness to the horizontal one in transversely isotropic media, and then by using this dispersion relation Alkhalifah (2000) derived the anisotropic acoustic wave equation for vertical transversely isotropic media. Zhou et al. (2006) derived the equation for the anisotropic acoustic wave equation in two dimensional titled transverse isotropic media. Further, Operto et al. (2009) modified the TTI acoustic wave equation provided by Zhou et al. (2006). The anisotropic acoustic wave equation in the frequency domain can be written as

$$\begin{aligned} &\frac{\omega^2}{\kappa} p - (1+2\delta) Hp - H_0 p = (1+2\delta) Hq \\ &\frac{\omega^2}{\kappa} q - 2(\epsilon-\delta) Hq = 2(\epsilon-\delta) Hp, \end{aligned} \tag{1.12}$$

where κ is the bulk modulus; b is the inverse of mass density, termed buoyancy; the δ and ϵ are dimensionless parameters defining the anisotropy (Thomsen, 1986). H and H_0 are differential operator and the cross derivative term in these both differential operator are responsible for angular rotation of the symmetry axis in TTI medium, p is the pressure

wavefield, and q is the auxiliary pressure wavefield introduced by Zhou et al. (2006) to recast the fourth-order equation proposed by Alkhalifah (1998) into a coupled second-order equations which are much easier to solve.

1.3.3 Seismic Forward modelling

Seismic forward modelling is a computational technique used in geophysics to simulate the propagation of seismic waves through Earth's subsurface. It involves mathematical algorithms that calculate how seismic waves travel and interact with different geological structures, such as rock layers and faults. For input parameters like wave source, velocity models, and subsurface properties, forward modelling predicts the expected seismic response recorded by receivers at the surface or borehole locations. Seismic Forward modelling includes discretization of the wave equation, methods to numerically solve wave equation, stability criterion, numerical dispersion, accuracy and efficiency of the forward modelling algorithm and the implementation of absorbing boundary conditions.

1.3.4 Methods to numerically solve wave equation

There are several numerical method to discretize the wave equation:

1. **Finite Difference Method:**
   The finite difference method is widely recognized as the most direct approach and has been extensively utilized in seismological studies as the initial numerical method. The pioneers in the application of the finite-difference method to the investigation of elastic wave propagation are credited to Alterman and Karal Jr (1968), as documented in their work. Boore (1970), on the other hand, employed the finite difference method to simulate Love waves. Furthermore, Alford et al. (1974) conducted a comprehensive analysis of the finite difference approximation to the acoustic wave equation, comparing the numerical outcomes with analytical solutions. Robertsson et al. (1994) developed a finite-difference simulator to model wave propagation in viscoelastic media; he also shows that a staggered scheme of second-order accuracy in time and fourth-order accuracy in space appears to be optimal. Igel et al. (1995) presented an algorithm to solve anisotropic elastic wave equation using finite difference method. The staggered finite-difference method introduced by Virieux (1984) and Virieux (1986) for solving acoustic- and elastic-wave propagation is the most commonly used finite-difference method in exploration seismic applications. Reviews and practical guides to implementing the staggered finite-difference method are presented by Robertsson et al. (2012). Saenger and Bohlen (2004) describe the

application of the rotated staggered-grid finite-difference technique to the wave equations for anisotropic and viscoelastic media. Hustedt et al. (2004) compare different finite-difference schemes for two-dimensional acoustic frequency-domain forward modelling, and also discuss the idea of mixed-grid finite difference scheme. Galis et al. (2008) developed a new hybrid numerical method for 3-D viscoelastic modelling of seismic wave propagation and earthquake motion in heterogeneous media, based on the combination of the fourth-order velocity-stress staggered-grid finite-difference scheme.

2. **Psuedospectral Method:**
   The pseudospectral methods are based on discrete function approximations, allowing for precise interpolation at specified collocation points. Notably, the Fourier method utilizes trigonometric basis functions, while the Chebyshev method makes use of Chebyshev polynomials. This approach was the first to deviate from the finite difference method and found extensive application in various seismological studies. Pseudospectral methods emerged in the early 1980s as transform methods due to their reliance on Fourier transform for implementation. Initially applied to acoustic wave equations, these methods were later extended to elastic wave equations and three-dimensional scenarios (Kosloff and Baysal, 1982),. To enhance the accurate representation of curved internal interfaces and surface topography, grid stretching through coordinate transformation was introduced and successfully applied to acoustic and elastic wave propagation problems (Komatitsch et al., 1996; Tessmer et al., 1992).

3. **Finite Element Method:**
   The finite element method is a series expansion method. The continuous solution field is replaced by a finite sum over basis function. The finite element method is used to studied the surface wave propagation (Lysmer and Drake, 1972; Schlue, 1979). Marfurt (1984a) solved scalar wave equation using finite element method and also provide a comparison with finite difference method. Serón et al. (1990) developed a low order finite element method to solve the elastic wave propagation.

4. **Spectral Element Method:**
   The spectral element technique combines the adaptability of finite element approaches in terms of computational grids with the spectral accuracy of Lagrange basis functions implemented within the elements. The spectral element method was first applied in fluid dynamics (Maday and Patera, 1989; Patera, 1984). The initial publications on spectral element formulations for elastic wave problems can be

attributed to Priolo et al. (1994), Seriani and Priolo (1994) and Faccioli et al. (1996). Komatitsch and Vilotte (1998) present the spectral element method to simulate elastic wave propagation in realistic geological structures involving complicated free surface topography and material interfaces for two-and three dimensional geometries. Peter et al. (2011) demonstrate the great flexibility of the spectral element method for both modelling and inversion.

5. **Finite Volume Method:**
   The finite volume approach arises as a direct consequence of discretizing conservation equations while taking into account the fluxes between finite-volume cells containing averaged solution fields. For the first time Dormy and Tarantola (1995) solved elastic wave propagation using finite volume method. Tadi (2004) developed 2D elastic wave propagation algorithm using finite volume method. Brossier et al. (2008) proposed a new numerical technique for solving 2D elastodynamics equations based on finite volume frequency domain approach.

6. **Discontinous Galerkin Method:**
   The Discontinuous Galerkin method represents a variant of finite element methodologies, distinguished primarily by the characteristic that solution fields exhibit discontinuity at the interfaces of the elements. Käser and Dumbser (2006) present a discontinuous Galerkin numerical approach to solve the elastic wave equation in heterogeneous media in the presence of externally given source terms with arbitrary high order accuracy in space and time on unstructured triangular meshes. Dumbser and Käser (2006) used an arbitrary high-order discontinuous Galerkin method for simulation of elastic wave with unstructured meshes.

1.3.5 Stability Criterion and Numerical Grid Dispersion

The stability criterion is a fundamental concept to consider when dealing with space-time discretization and simulation task planning. The stability criterion is known as the Courant-Friedrichs-Lewy (CFL) criterion, is a dimensionless quantity that represents the ratio between physical velocity and grid velocity. While satisfying the CFL criterion is necessary, it is not sufficient to ensure the accuracy of the simulation. To achieve accurate simulation results, it is essential to meet the numerical grid dispersion criterion as well. The number of grid point per wavelength is the crucial factor to avoid dispersion. Note that, as the number of grid point per wavelength increase, the grid increment will be decreased, therefore computational cost increases. These two criterion plus other reason

gave rise to a debate whether the wave equation need to be solved in time domain or frequency domain.

1.3.5.1 Frequency Domain modelling

Despite the effectiveness of time-domain modelling, there is a renewed interest in frequency-domain methods, mainly driven by researchers interested in full waveform inversion and the accurate modelling of seismic attenuation. Frequency domain finite difference (FDFD) methods have been actively employed in wave equation analysis. Pratt (1990) did elastic wave modelling in the frequency domain using the finite difference method and provided a tool for cross-hole seismic imaging. Pratt and Worthington (1990) propose a second-order five-point finite-difference scheme for modelling 2D acoustic waves in the frequency domain. To ensure accurate results and avoid dispersion, the authors recommend a minimum of 13 grid points per wavelength for implementing this scheme. The second-order nine-point 2D acoustic wave extrapolator proposed by Jo et al. (1996) utilizes a unique approach. This technique approximates the spatial derivatives and mass acceleration term by integrating second-order five-point central difference stencils in Cartesian coordinates with the central difference scheme in a rotated 45-degree coordinate. This innovative combination significantly decreases the minimum number of grid points required per wavelength to 3.3. In order to enhance the precision of numerical calculations, Shin and Sohn (1998) devised a method that integrates rotated coordinate systems at angles of 26.6, 45, and 63.4 degrees. Additionally, they incorporated a nine-point extrapolator and introduced a second-order 25-point finite difference scheme. As a result, the necessary number of grid points per wavelength was reduced to 2.5. Hustedt et al. (2004) compare different finite-difference schemes for modelling the 2D acoustic wavefields and present a 13-point scheme without rotating the coordinates. Marfurt (1984b) used finite element frequency domain approach for seismic modelling. Shi et al. (2016) developed spectral element method for elastic and acoustic waves in frequency domain.

1.3.6 Accuracy and Efficiency

Accuracy and efficiency are two critical factors in evaluating the performance of an algorithm. Accuracy refers to how close an algorithm's output is to the true or desired output. Efficiency measures how well an algorithm utilizes computational resources such as time and memory. Crase (1990) developed an high order space and time finite-difference modelling of the elastic wave equation to increase the efficiency and accuracy of the modelling. De Basabe and Sen (2007) provide formulas of grid dispersion and stability

criteria of some finite-elements methods for acoustic and elastic wave equations based on the approach of generalized eigen value formulation. Seriani and Oliveira (2008) studied the numerical dispersion of spectral element methods of arbitrary order for the isotropic elastic wave equation in two and three dimensions by a simplified model analysis of the discrete wave operators. Moczo et al. (2010) provide a detailed analysis on accuracy of the finite-difference and finite-element schemes with respect to P-wave to S-wave speed ratio. De Basabe and Sen (2010) studied the stability of some higher-order finite element methods, namely the spectral element method and the interior-penalty discontinuous Galerkin method for acoustic or elastic wave propagation. Etgen and O'Brien (2007) provide a tutorial on computational methods for large-scale 3D acoustic finite-difference modelling.

1.3.7 Absorbing boundary condition

Absorbing boundary condition is crucial in seismic forward modelling. Absorbing boundary conditions (ABCs) minimize reflections, ensuring reflection-free boundaries. They prevent wave wrap-around in finite domain simulations. ABCs absorb waves leaving the computational domain, preventing artificial reflections. Their implementation enhances accuracy, stability, and numerical performance. They are essential for seismic modelling in various applications. Higdon (1991) provided absorbing boundary conditions for elastic waves based on compositions of simple first order differential operators. Liu and Sen (2010) proposed an efficient scheme to absorb reflections from the boundaries in numerical solutions of wave equations by dividing the computational domain into boundary, transition, and inner areas. Berenger (1994) developed perfectly matched layer (PML) boundary condition based on the use of an absorbing layer especially designed to absorb the reflection for electromagnetic waves. Komatitsch and Tromp (2003) developed a perfectly matched layer absorbing boundary condition for the second-order seismic wave equation.

1.4 Joint Inversion

In recent years, oil and gas exploration has moved into areas that contain geological units with similar characteristics as encountered in mineral exploration. Imaging the extent and structure of sediments beneath basalt layer and below and the flanks of salt domes is particularly problematic using seismic method only. Also, seismic data have constraints in accurately defining the interface between hydrocarbons and water due to the minimal

contrast in seismic velocities between the two fluids. In both basalt and salt case the problem are similar, the high velocity contrast between the basalt or salt and sediments above makes it easy to image the top of the structures due to high reflection coefficient. This high reflection coefficient though has the effect that little energy penetrates below and any topography on this interface will distort the seismic wave. One potential strategy to enhance the accuracy of seismic models is to conduct electromagnetic surveys in conjunction with seismic surveys. Joint inversion is a sophisticated computational technique in geophysics that integrates multiple types of geophysical data to produce a more accurate and comprehensive model of the subsurface. By combining data from different sources, joint inversion leverages the strengths and compensates for the weaknesses of individual geophysical methods, thereby enhancing the resolution and reliability of subsurface imaging. There are several types of joint inversion, categorized based on the nature of the integrated data sets and the inversion methodologies employed. There are mainly two types of joint inversion.

1. **Simultaneously joint inversion:**
   This type involves inverting multiple data sets together in a single, unified framework. It typically uses a single objective function that integrates all data types, providing a more coherent and mutually consistent subsurface model.

2. **Cooperative or Constrained inversion:**
   This type involves inverting single data sets while the information derived form the other geophysical properties are incorporated into the inversion.

1.4.1 Simultaneously Joint Inversion

In Simultaneously joint inversion, different types of datasets are inverted within a single computational algorithm, with a single objective function and where all model parameter are adjusted concurrently throughout the inversion. Simultaneous joint inversion is further classified into two parts.

1. **Inversion through direct parameter coupling:**
   Direct parameter coupling included making a cross-property relationship from the borehole, Petrophysical relationship (Chen and Hoversten, 2012; Heincke et al., 2006; Panzner et al., 2016). The initial classification is established on the correlation between conductivity and seismic velocity via petrophysical parameters such as fluid saturation and porosity (Harris and MacGregor, 2006; Hoversten et al., 2006).

Here the relationship is not expressed in terms of one geophysical parameter as a function of another, but all geophysical quantities (e.g., resistivity, velocity, density) are functions of quantities such as porosity and permeability. However direct parameter coupling requires accurate cross-property relationships, which might not be well-defined across different geological settings. Panzner et al. (2016) use a sequential analysis of different datasets, where inversion are performed individually, but information is exchanged between the inversions. These kinds of integrated workflows are often used in hydrocarbon exploration instead of full joint inversion. Heincke et al. (2017) perform a full joint inversion of three different datasets. Unfortunately, these petrophysical relationships are not superficial and may not be accurate or unique.

2. **Inversion through Structural Coupling:**
   Establishing accurate relationships between different types of geophysical properties is inherently challenging due to the complex nature of subsurface structures. One effective approach to address this challenge is to structurally coupled the different geophysical parameters without requiring an explicit functional relationship between them by employing the cross-gradient method. By using the cross-gradient approach, the inversion processes of multiple geophysical datasets are linked, allowing for the consistent integration of distinct geophysical properties and thereby improving the reliability and coherence of the resulting subsurface models. The cross-gradient function between two model vectors is defined as the cross-product of the spatial gradient of each model. Gallardo and Meju (2003) and Gallardo and Meju (2004) introduce and successfully apply this approach in two dimensions for joint interpretation of DC resistivity and seismic travel time data. Haber and Holtzman Gazit (2013) and Meju and Gallardo (2016) discuss some of the issues implementing this constraint for practical inversion. Gallardo et al. (2012) developed a robust geophysical integration algorithm that structurally combines different datasets. Linde et al. (2006) jointly invert the P-wave and S-wave velocities for local earthquake tomography. Colombo and De Stefano (2007) and Colombo et al. (2008) developed a structurally joint inversion algorithm for MT and seismic data in marine environments for reservoir-exploration applications. However, there are some limitations to structurally coupled joint inversion, e.g., it is difficult to combine different types of geophysical data, which may have different resolutions and sensitivities; it is computationally intensive due to the integration of multiple datasets and inversion

schemes.

1.4.2 Cooperative or constrained inversion

In cooperative inversion, the information is incorporated from other geophysical studies as constraints but does not perform a joint inversion. These constraints are based on prior information, which might be uncertain or incorrect, leading to biased results. This means that the information is considered as an estimation of ground truth, potentially with some uncertainty, but there is no feedback to modify it as a result of the inversion. Meju et al. (2019) developed 3D anisotropic structurally constrained CSEM inversion algorithm. Structure-guided 3D inversion of CSEM and MT data was developed by Miller et al. (2019). Ma et al. (2024) developed image-guided structure-constrained inversion of electrical resistivity data. 3D Structurally CSEM inversion algorithm using octree meshes developed by Liu et al. (2024).

1.5 Structure of the thesis

The joint analysis of multiphysics data using inverse modelling has great potential for solving challenging problems related to subsurface imaging. With evolving energy scenarios, projects like enhanced oil recovery and CO2 sequestration monitoring are the need of the hour. Therefore, the geophysical research community is actively pursuing the integration of multiphysics data. With a similar objective, this thesis aims to work on joint analysis of CSEM and seismic data, focusing on inverse modelling algorithm development and scrutinising their advantages and limitations. The objective includes developing algorithms that can invert for anisotropic subsurfaces which require more computational resources than isotropic cases. Furthermore, due to the varying resolutions of seismic and CSEM data, the discretisation may be governed by the higher resolution method. Consequently, considering anisotropy and the objective of integrating the seismic and CSEM data pose a computationally challenging problem. Therefore, the focus of the present thesis is on the 2D imaging of the subsurface. For joint inversion, we first focus on cooperative strategy, where the CSEM data inversion is constrained by prior structural information derived from other geophysical methods, say seismic. To this end, we present a novel algorithm and provide a comprehensive analysis using numerical experiments using a complex model. Secondly, we work towards the development of simultaneous joint inversion of seismic and CSEM data. For this objective, we developed a seismic modelling algorithm

for anisotropic modelling. The future goal is to integrate the algorithms developed in this thesis to devise a simultaneous joint inversion algorithm. A brief chapter-wise description of the content of the present thesis is as follows.

1. In the first chapter, the thesis provides an overview of the fundamental concepts related to the CSEM method. It begins with a basic introduction to the principles and applications of the CSEM method. The chapter also covers the basics of EM inversion methods. Additionally, the chapter introduces the seismic method, outlining the basics of seismic data acquisition and processing. It concludes with an explanation of seismic forward modelling techniques and methodologies.

2. The second chapter delves into the development of a space-domain forward modelling algorithm specifically designed for two-dimensional CSEM inversion. It starts with an introduction to the importance and challenges of forward modelling in geophysics. The chapter then presents the mathematical formulation of the problem, including the governing equations and numerical methods used. Following this, the implementation of the algorithm is discussed. The chapter also includes a section on the validation and testing of the inversion algorithm, benchmarking its performance against synthetic and real data. Finally, the results obtained from the forward modelling and inversion are analyzed and discussed in detail.

3. In the third chapter, the thesis focuses on the development of a structurally constrained inversion algorithm that integrates CSEM results with other geophysical data using the cross-gradient method. The chapter begins with an introduction to the concept of joint inversion, highlighting its motivation and objectives. It then explains the cross-gradient method, providing a detailed theoretical and mathematical formulation. The results from the constrained inversion are presented and analyzed through various case studies and performance evaluations.

4. The fourth chapter addresses the development of a two-dimensional anisotropic acoustic wave modelling algorithm. This chapter begins with an introduction to anisotropic acoustic wave modelling, emphasizing its significance and applications in geophysics. It then details the mathematical models and numerical techniques used to simulate wave propagation through anisotropic subsurface formations. The development and implementation of the algorithm are discussed, including the

computational challenges and solutions. The chapter also includes validation and testing of the algorithm, with results presented from various synthetic and real-world scenarios.

5. The final chapter of the thesis summarizes the key findings and contributions of the research. It revisits the objectives outlined in the introduction and discusses how they were achieved through the development of advanced geophysical inversion techniques. The chapter provides a comprehensive summary of the results from each of the preceding chapters, emphasizing the improvements and innovations introduced. It also discusses the limitations encountered during the research and provides suggestions for future work. The chapter concludes with an outlook on the potential future developments in the field, including the proposed development of a two-dimensional anisotropic seismic inversion algorithm and the simultaneous integration of seismic and CSEM results through a joint inversion algorithm. This integrated approach aims to further enhance subsurface imaging and characterization in geophysical exploration.

Chapter 2

2D CSEM algorithm based on a space-domain forward modeling approach

2.1 Abstract

We develop a two-dimensional controlled-source electromagnetic inversion algorithm employing a space-domain forward modeling algorithm. The space-domain forward modeling algorithm is devised by imposing boundary conditions on the plane perpendicular to the strike direction that passes through the source position. The boundary conditions for various source types are derived using the symmetric/ antisymmetric character of the electric and magnetic fields. The benchmarking analysis reveals that roughly eight grids are sufficient for discretizing space in the strike directions for accurate forward response computations. For inverse modeling, the Gauss-Newton optimization technique is utilized. Numerical inversion experiments of synthetic and real-field data clearly demonstrate the versatility and robustness of the developed algorithm. The inversion experimentations also concur with the forward response benchmarking analysis and suggest that only a few grids (around eight) are adequate to discretize space in the strike direction. The developed algorithm is more than one order efficient compared to a wavenumber domain code.

2.2 Introduction

The three-dimensional character of the source in a controlled-source electromagnetic (CSEM) method is considered to be the primary cause for less focus on the development

of 2D CSEM inversion algorithms Constable (2010). That's why several 3D forward Spitzer (2024); Wang et al. (2021); Yavich and Zhdanov (2020) and inverse modeling algorithms Long et al. (2024); Xue et al. (2023) have been developed for interpreting CSEM data. However, Weiss and Constable (2006) argued that CSEM data recorded along a profile can be very well analyzed using a 2D CSEM inversion code. Hoversten Jr et al. (2001) shows that 2D inversion of crosswell EM data can provide useful information in realistic 3D petroleum reservoirs. If a CSEM data set is indeed sensitive to 2D conductivity distribution, either due to the subsurface conductivity distribution or survey geometry, 2D inversion should be preferred for such data analysis because an unwarranted application of 3D inversion causes unnecessary over-parameterization of an inverse problem than required. The typical marine CSEM data recorded at inline receivers due to an electric dipole is generally sensitive to the subsurface between the transmitter and receivers Weiss and Constable (2006). In hydrocarbon exploration investigations, the inline electric field over a buried thin-resistive reservoir often matched well with CSEM data simulated by a 2D code Key (2016). 2D inversion can be very valuable in towed CSEM systems Anderson and Mattson (2010); Constable et al. (2016), where the source and receives are generally moved along a line. Furthermore, the thousands of source and receiver positions in a towed CSEM system make 3D inversion computationally expensive. Moreover, the subsurface resistivity recorded using a 2D inversion algorithm can also serve as an initial guess for 3D inversion, which can reduce the cost of 3D inversion Key (2016). Consequently, many 2D forward Li et al. (2020) and inverse Abubakar et al. (2008); Key (2016) modeling algorithms have been developed in the past. The 2D CSEM inversion has been applied in many studies as reported in the literature Chesley et al. (2021); Weitemeyer et al. (2010).

The computational complexity of 2D frequency-domain forward modeling in the presence of a controlled source is the primary hindrance of 2D inversion algorithms compared to plane-wave methods such as magnetotelluric. Though a general solution can be formulated in the space domain, nonetheless, to overcome the 3D nature of the source in a computationally efficient manner, the 2D frequency-domain CSEM problem is generally solved in the wavenumber domain. For reliable space-domain responses, wavenumber-domain simulations are required for tens of wavenumbers. For example, Key and Ovall (2011) uses 30 wavenumbers in the MARE2DEM code. Generally, a digital filter Anderson (1989) or Gauss quadrature method Chave (1983) is used for the space-domain transformation. A Gauss-Legendre quadrature-based inverse Fourier transform technique is employed by Zeng et al. (2018) for a logging experiment. Wu et al. (2019) used a Gauss-Hermite quadrature-based integration for inverse Fourier transform for logging-while-drilling electromagnetic (EM) method in 2-D anisotropic media. It involves

wavenumber-domain response calculation for a wide wavenumber band covering several decades Key and Ovall (2011) followed by hundreds of thousands of Fourier transforms. In the case of inverse modeling, the simulations are required to be performed for both forward and adjoint fields. For example, a Jacobian matrix corresponding to m parameter and n data would require mn Fourier transforms Key (2016). Consequently, 2D CSEM inversion algorithm implementation is a tricky and computationally expensive task, owing to the requirement of Fourier transform. Recently, Engebretsen et al. (2022) and Xiao et al. (2022) have presented a space-domain algorithm for time-domain electromagnetic data recorded by airborne systems using the symmetry of EM fields in 2D models. The present study develops an efficient 2D CSEM inversion algorithm based on a space-domain forward modeling scheme. The proposed algorithm is easy to implement. For theoretical foundation, boundary conditions devised for the forward modeling algorithm are discussed in detail. The numerical experiments are carried out for synthetic and field data to ascertain the robustness of the developed algorithm.

2.3 Forward and Inverse Modeling Methodology

In the frequency domain, Maxwell's curl equations that describe the electrodynamics can be written as (considering $e^{-\iota\omega t}$ time dependency)

$$\begin{aligned} \nabla \times \mathbf{E} &= \iota\omega\mu\mathbf{H} + \mathbf{J}^m\delta(\mathbf{r}-\mathbf{r}_s), \\ \nabla \times \mathbf{H} &= (\hat{\sigma} - \iota\omega\epsilon)\mathbf{E} + \mathbf{J}^e\delta(\mathbf{r}-\mathbf{r}_s), \end{aligned} \tag{2.1}$$

where $\mathbf{E}$ and $\mathbf{H}$, denote electric and magnetic field, respectively; ω is angular frequency; μ and ϵ represent magnetic permeability and electric permittivity, respectively; $\iota = \sqrt{-1}$; $\hat{\sigma}$ denotes conductivity tensor; $\mathbf{J}^m$ and $\mathbf{J}^e$ are magnetic and electric current densities due to sources; $\mathbf{r}_s = [x_s, y_s, z_s]$, is the source's position vector and $\delta()$ is Dirac delta function. The magnetic current density is not defined in EM field theory, here it is simply used to represent a magnetic source. For an anisotropic media, the $\hat{\sigma}$, is defined as Martí (2014)

$$\hat{\sigma} = \begin{pmatrix} \sigma_{xx} & \sigma_{xy} & \sigma_{xz} \\ \sigma_{yx} & \sigma_{yy} & \sigma_{yz} \\ \sigma_{zx} & \sigma_{zy} & \sigma_{zz} \end{pmatrix}. \tag{2.2}$$

The vector Helmholtz equation can be derived using equation (2.1), and in terms of electric field; assuming μ is constant in space, it is expressed as

$$\nabla \times \nabla \times \mathbf{E} - (\iota\omega\mu\hat{\sigma} + \omega^2\mu\epsilon)\mathbf{E} = \mathbf{s}(\omega)\delta(\mathbf{r} - \mathbf{r}_s), \tag{2.3}$$

where $\mathbf{s}(\omega)$ is the source term that can be an electric or magnetic transmitter. A source can be an array of transmitters, and using the linearity of equation (2.3), a joint response of the transmitter's array can be calculated concurrently. Conventionally, for a 2D medium, the EM field simulation is done by first transforming equation (2.3) into the wavenumber domain and then numerically solving the wavenumber-domain equation. The wavenumber domain equation contains only two space variables, leading to the requirement of discretization being restricted to 2D space only. Typically, the homogeneous Dirichlet boundary conditions (BCs) are applied on all sides of the model for CSEM modeling. After simulation using tens of wavenumber, the inverse Fourier transform is applied to obtain the space-domain response. The present study explores the prospect of an efficient inversion algorithm based on space-domain simulation of EM field for both forward and adjoint fields for 2D models. The subsequent part of this section explains the theory of the proposed forward modeling algorithm.

The vector equation given in equation (2.1) can be decomposed into six scalar equations. Furthermore, for a 2D model with a strike in the y-direction, these scalar equations can be transformed into the wavenumber domain (considering $e^{\iota k_y y}$ space dependency) as

$$\iota k_y E_z - \frac{\partial E_y}{\partial z} = \iota\omega\mu H_x + J_x^m e^{\iota k_y (y-y_s)}\delta(x-x_s)\delta(z-z_s), \tag{2.4}$$

$$\frac{\partial E_x}{\partial z} - \frac{\partial E_z}{\partial x} = \iota\omega\mu H_y + J_y^m e^{\iota k_y (y-y_s)}\delta(x-x_s)\delta(z-z_s), \tag{2.5}$$

$$\frac{\partial E_y}{\partial x} - \iota k_y E_x = \iota\omega\mu H_z + J_z^m e^{\iota k_y (y-y_s)}\delta(x-x_s)\delta(z-z_s), \tag{2.6}$$

$$\iota k_y H_z - \frac{\partial H_y}{\partial z} = (\sigma_{xx} - \iota\omega\epsilon)E_x + \sigma_{xy}E_y + \sigma_{xz}E_z + J_x^e e^{\iota k_y (y-y_s)}\delta(x-x_s)\delta(z-z_s), \tag{2.7}$$

$$\frac{\partial H_x}{\partial z} - \frac{\partial H_z}{\partial x} = \sigma_{yx}E_x + (\sigma_{yy} - \iota\omega\epsilon)E_y + \sigma_{yz}E_z + J_y^e e^{\iota k_y (y-y_s)}\delta(x-x_s)\delta(z-z_s), \tag{2.8}$$

$$\frac{\partial H_y}{\partial x} - \iota k_y H_x = \sigma_{zx}E_x + \sigma_{zy}E_y + (\sigma_{zz} - \iota\omega\epsilon)E_z + J_z^e e^{\iota k_y (y-y_s)}\delta(x-x_s)\delta(z-z_s). \tag{2.9}$$

For brevity, identical notations are used for the field in the wavenumber domain as in the space domain. For 2D models with the strike in the y-direction, the electric conductivity tensor spatially varies only on x and z-directions. Accordingly, for the 2D model, we aim to derive a set of BCs at a xz plane in the space domain, utilizing equations (2.4)–(2.9). First,

the symmetric and antisymmetric nature of the field in the wavenumber domain with respect to k_y is examined. Subsequently, the property of Fourier transform is employed to obtain BCs at a xz plane in the space domain. Foremost, the right-hand side terms of equations (2.4) to (2.9) need to be made independent of k_y, which is achieved by defining the plane as $y = y_s$. The next step is to obtain the relationship between the electric and magnetic fields at k_y and $-k_y$ under $y = y_s$. Since equation (2.5) does not contain k_y except in source term, and it relates E_x, E_z, and H_y field components; consequently, E_x, E_z, and H_y field components will have identical behavior in terms of symmetry/antisymmetry characteristic about $y = y_s$ plane. Likewise, the other group consisting of E_y, H_x, and H_z will have identical behavior. However, it requires decoupling the current density's y-component from the x- and z-components of the electric field. It is achieved by defining one of the principal directions of conductivity along the y-coordinate axis. Therefore, the conductivity tensor given in equation (2.2) requires to be redefined as

$$\hat{\sigma} = \begin{pmatrix} \sigma_{xx} & 0 & \sigma_{xz} \\ 0 & \sigma_{yy} & 0 \\ \sigma_{zx} & 0 & \sigma_{zz} \end{pmatrix}. \tag{2.10}$$

The grouping mentioned above is realized because for equations (2.4)–(2.9), if the k_y term is associated with the member of one group, the terms without k_y are always from another group in an equation. Now, for the conductivity tensor defined in equation (2.10), the BCs at a plane $y = y_s$ for different transmitter types can be obtained with a simple procedure. Let's compare the solution of coupled equations (2.4)–(2.9) at $\pm k_y$ considering a single transmitter oriented along any one coordinate axis. This implies that only one equation will be inhomogenous while all five other equations will be homogeneous. For the inhomogeneous equation, the field term with k_y as a coefficient will be an odd function of k_y, while the variables without k_y will be even functions. It occurs because the negative sign of $-k_y$ is absorbed by the variable term associated with it, leading to the same equation as for k_y. Since signs of the solution do not matter for homogeneous equations, the odd/even character of all the variables associated with these equations are only governed by the inhomogeneous equation. For example, in the case of a horizontal-electric dipole oriented in the x-direction (HED$_x$; here, subscript, $_x$, denotes the orientation), that means, except J_x^e, all other current density terms are zero, the E_x, E_z, and H_y will be even functions of k_y whereas E_y, H_x, and H_z will be odd functions. Now, from the property that the Fourier transform of even (odd) function is even (odd), for HED$_x$, the BCs at $y = y_s$ plane can be written as (see Appendix A.1 for more details)

$$\begin{aligned} E_x^{y_s^-} &= E_x^{y_s^+}; E_y^{y_s^-} = -E_y^{y_s^+}; E_z^{y_s^-} = E_z^{y_s^+} \\ H_x^{y_s^-} &= -H_x^{y_s^+}; H_y^{y_s^-} = H_y^{y_s^+}; H_z^{y_s^-} = -H_z^{y_s^+}, \end{aligned} \tag{2.11}$$

where the superscripts, $^{y_s^-}$ and $^{y_s^+}$ denote the field on the negative and positive sides but equidistant from plane $y = y_s$. These BCs are also applicable for a vertical-electric dipole (VED_z) and horizontal-magnetic dipole oriented in the y-direction (HMD_y) as these are members of the same group. Alternatively, we can follow the same procedure to derive the BCs for (VED_z) and (HMD_y). Likewise, for HED_y, where all current density terms except, J_y^e, will vanish, the E_x, E_z, and H_y will be odd functions whereas E_y, H_x, and H_z will be even functions. Hence, for HED_y, the BCs at $y = y_s$ plane can be expressed as,

$$\begin{aligned} E_x^{y_s^-} &= -E_x^{y_s^+}; E_y^{y_s^-} = E_y^{y_s^+}; E_z^{y_s^-} = -E_z^{y_s^+} \\ H_x^{y_s^-} &= H_x^{y_s^+}; H_y^{y_s^-} = -H_y^{y_s^+}; H_z^{y_s^-} = H_z^{y_s^+}, \end{aligned} \tag{2.12}$$

Furthermore, these BCs are also true for vertical-magnetic dipole (VMD_z) and the HMD_x transmitters. Magnetic dipole transmitters are important in cross-well EM tomography, where 2D inversion is generally preferred, particularly for vertical wells Hoversten Jr et al. (2001). Magnetic transmitters are also employed in airborne EM methods, where data is recorded along profiles. Therefore, for 2D analysis of airborne EM data, the BCs obtained for the magnetic source can be applied. To illustrate these characteristics of the EM field, we consider a complex 2D model. The model includes an isotropic salt body of resistivity 50 Ωm and anisotropic reservoir (ρ_v- 200 Ωm; ρ_h- 100 Ωm) embedded in a background having linearly increasing resistivity from 1km (ρ_v- 2 Ωm; ρ_h- 1 Ωm) to 4km (ρ_v- 10 Ωm; ρ_h- 5 Ωm), as shown in Figure (2.1). The simulation of the transmitter placed at (0, 0, 970) m is performed by 3D CSEM modeling code developed by Dehiya (2021), and the field is calculated on 100 × 100 m grid points at the seafloor (z=1 km). The magnitude shall be symmetric about the line $y = 0$ m for both even and odd functions, while the phase shall be symmetric for the even case and will be reversed in the case of odd functions. The plots of magnitude overlayed by the phase for all three electric field components for HED_x and HED_y transmitters are shown in Figure (2.2), where the magnitude for all the cases is symmetric about $y = 0$ line. For HED_x, the phase is symmetric for E_x and E_z components while it is reversed for E_y component, whereas, for HED_y, the phase is reversed for E_x and E_z components and it is symmetric for E_y component. These observations are in concurrence with the conditions derived in equation (2.11) and equation (2.12),

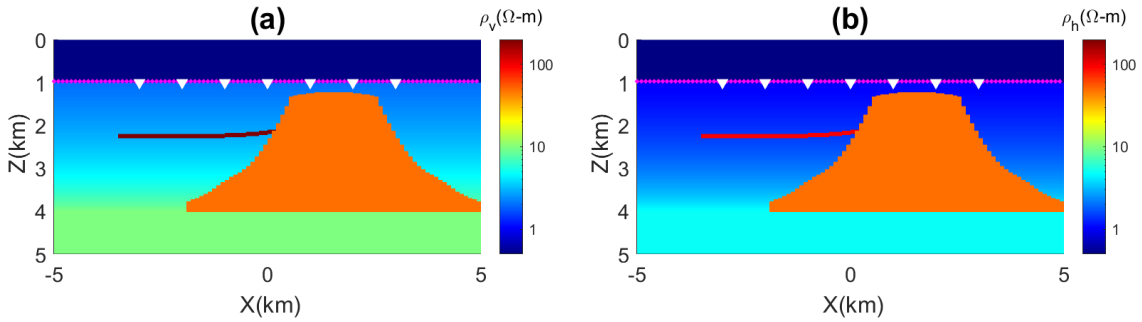

Fig. 2.1 Synthetic 2D-VTI resistivity model; (a) vertical resistivity; (b) horizontal resistivity.

respectively. Furthermore, using the differentiation definition, the BCs for symmetric and antisymmetric functions can be written as,

$$\frac{\partial f(y)}{\partial y} = 0, \tag{2.13}$$

and

$$\frac{\partial f(y)}{\partial y} - \frac{1}{\Delta y} f(y + \Delta y) = 0, \tag{2.14}$$

respectively. Equation (2.13) defines a homogeneous Neumann BC (Neumann boundary condition), whereas equation (2.14) is somewhat similar to a homogeneous Robin BC (Robin boundary condition). Therefore, homogeneous Neumann BC is applied for symmetric field components, and for antisymmetric field components, the BC given in equation (2.14) is used.

We can draw many useful conclusions from the above discussion and the relations given in equations (2.11)–(2.12). First, the transmitters can be classified into two groups viz., (i) HED_x, VED_z, HMD_y and (ii) HED_y, HMD_x, VMD_Z, where all members of a group have same symmetric/antisymmetric characteristics of different components of EM field. Furthermore, for any source constructed by a linear combination of transmitters that includes members of both groups, the joint response will be neither symmetric nor antisymmetric. Consequently, for a wavenumber-based algorithm, the inverse Fourier transform would require either response at both positive and negative wavenumbers or wavenumber-domain simulation should be done separately for both groups. For example, in the case of an arbitrarily oriented electric dipole, the computation for the HED_y contribution and its projection in the xz plane needs to be done separately. Second, equations (2.11) to (2.12) help in understanding whether sine or cosine transform is adequate for Fourier transform while transforming various components into space domain in a wavenumber-based algorithm. Another valuable piece of information is that in case one

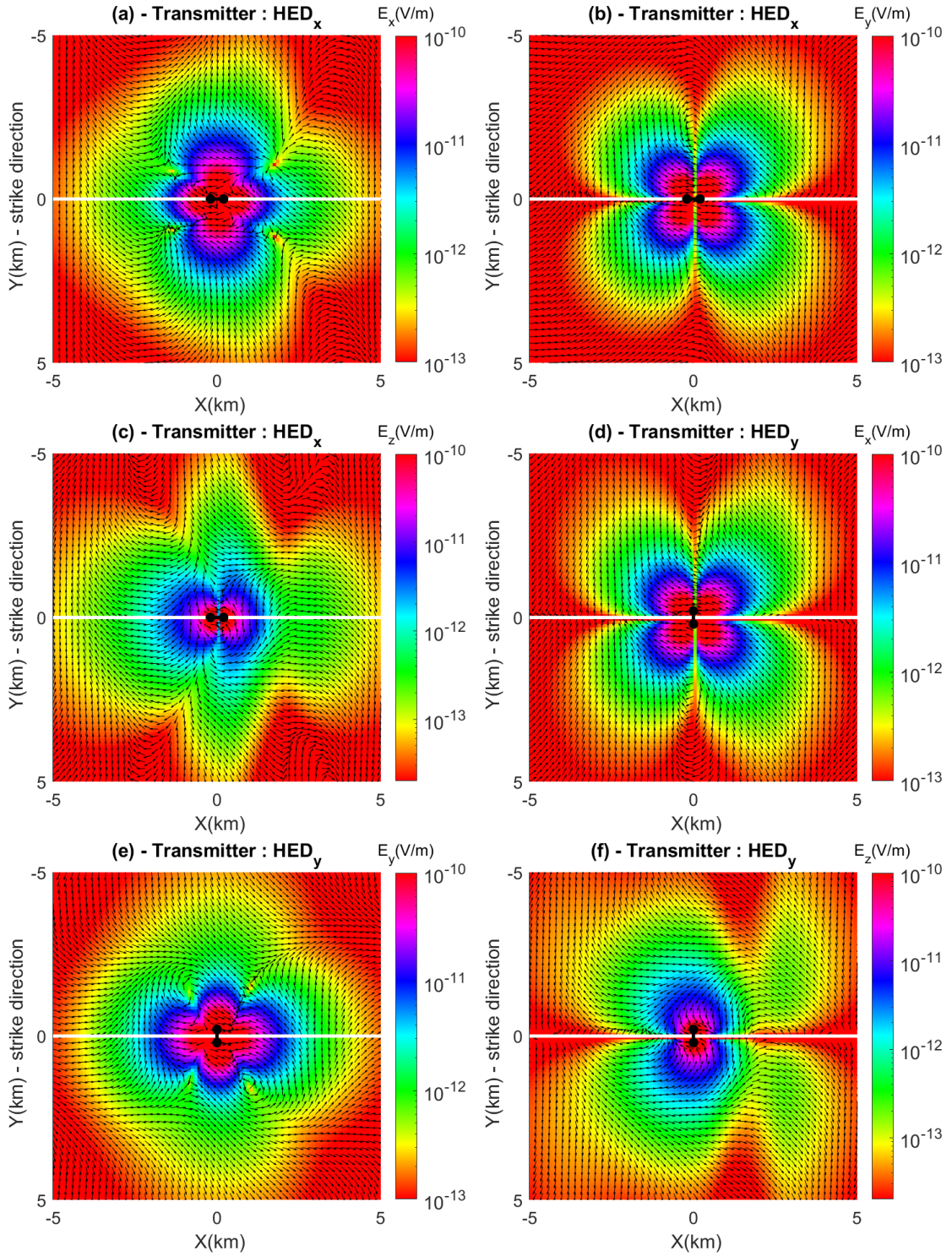

Fig. 2.2 EM field magnitude overlayed by phase for HED_x (a-c) and HED_y (d-f) for the transmitter located at 0, 0, 970 m and receivers are placed at 1000 m depth on a 100 × 100 m grid.

of the principal axes of anisotropy is not in the y-coordinate direction, the field will not be symmetric/antisymmetric; therefore, the wavenumber-domain solutions need to be computed at both negative and positive wavenumbers. Furthermore, the condition of the plane of symmetry (i.e., $y = y_s$) suggests that the source-receiver offset in the strike direction should be taken from the source position rather than from the coordinate axes, otherwise, the symmetric/antisymmetric condition will not be attained and again both negative and positive wavenumbers will be required for inverse Fourier transform. All these requirements are taken care of in a wavenumber-based EM modeling algorithm and are known; nonetheless, it is instructive to highlight these with the above analysis.

Inverse modeling is posed as an optimization problem that aims to minimize the misfit between observed data, $\mathbf{d}^{obs}$, and predicted data, $\mathbf{F}(\mathbf{m})$. The objective functional that we seek to optimize in this study is defined as,

$$\phi = ||\mathbf{W}_d(\mathbf{d}^{obs} - \mathbf{F}(\mathbf{m}))||_2 + \lambda(||\mathbf{Rm}||_2 + \beta||\mathbf{Lm}||_2) \tag{2.15}$$

where $\mathbf{W}_d$, denotes data covariance matrix; λ is regularization parameter; $\mathbf{R}$ denotes second order derivative (Laplacian) operator; β is a positive scalar; $\mathbf{L}$ is an operator that seeks to minimize the difference between horizontal and vertical conductivities. The last term is applicable only in the case of anisotropic inversion. Using the Gauss-Newton method, we can write an expression for estimation of correction in model parameter, $\delta\mathbf{m}_i$, at i^{th} iteration as,

$$\mathbf{H}_{i-1}\delta\mathbf{m}_i = -\mathbf{g}_{i-1}, \tag{2.16}$$

where

$$\mathbf{H}_{i-1} = \mathbf{J}_{i-1}^T\mathbf{W}_d^T\mathbf{W}_d\mathbf{J}_{i-1} + \lambda_{i-1}(\mathbf{R}^T\mathbf{R} + \beta\mathbf{L}^T\mathbf{L}), \tag{2.17}$$

and

$$\mathbf{g}_{i-1} = -\mathbf{J}_{i-1}^T\mathbf{W}_d^T\mathbf{W}_d(\mathbf{d}^{obs} - \mathbf{F}(\mathbf{m}_{i-1})) + \lambda_{i-1}(\mathbf{R}^T\mathbf{R}\mathbf{m}_{i-1} + \beta\mathbf{L}^T\mathbf{L}\mathbf{m}_{i-1}), \tag{2.18}$$

where $\mathbf{H}_{i-1}$ and $\mathbf{g}_{i-1}$ represent Hessian and gradient of objective functional computed for the model parameter, $\mathbf{m}_{i-1}$ after $(i-1)^{th}$ iteration and $\mathbf{J}_{i-1}$, is the Jacobian matrix calculated for model parameter, $\mathbf{m}_{i-1}$. An adjoint approach Mcgillivray and Oldenburg (1990) is used for Jacobian matrix computation. Finally, the updated model parameter after i^{th} iteration is calculated as, $\mathbf{m}_i = \mathbf{m}_{i-1} + \delta\mathbf{m}_i$. Equation (2.16) can be rearranged for direct computation of the updated model parameter as,

$$\mathbf{H}_{i-1}\mathbf{m}_i = -\mathbf{g}_{i-1} + \mathbf{H}_{i-1}\mathbf{m}_{i-1}. \tag{2.19}$$

A normalized Root Mean Square ($nRMS$), defined as,

$$nRMS_i = \sqrt{\frac{1}{n}\sum_{i=1}^{n}\frac{(d_i^{obs} - \mathbf{F}(\mathbf{m})_i)^2}{|\mathbf{d}_i^{obs}|^2}}, \tag{2.20}$$

is computed at each iteration, where n is the number of data points.

2.4 Algorithm

In this study, we propose to solve the 2D CSEM inverse modeling problem using a space domain forward (and adjoint) simulation scheme. The forward modeling is achieved by solving equation (2.3) using a staggered-grid finite-difference technique. The model discretization is similar to a 3D case, except that in the y-direction (strike direction), only one side of the xz plane that passes through the source position is taken as part of the modeling domain. The electric field components, $\mathbf{E}_x$, $\mathbf{E}_y$ and $\mathbf{E}_z$ are defined at the mid of cell sides in x-, y- and z-directions, respectively. Meanwhile, the magnetic fields are defined at the center of cell faces. Figure 2.3 depicts the discretization scheme at a representative cell. At the $y = y_s$ plane, the BCs are source dependent as given in equation (2.11) and (2.12). The homogeneous Dirichlet BCs are applied on all other sides of the model. Let's denote the linear system of equations obtained after discretization as

$$\mathbf{Ae} = \mathbf{b}, \tag{2.21}$$

where **A** denote system matrix; **e** describes a vector comprising nodal electric fields and **b** contains source information. A primary/secondary approach is employed to handle the source singularity. Since the BCs mentioned above also apply to the total and primary fields, these are also satisfied by the secondary field. It is important to note that the system matrix depends on BCs and will not be the same for different source types having distinct BCs at $y = y_s$ plane. Consequently, a source with an orientation that requires to be expressed by a linear combination of different source types needs separate computations. However, in a typical marine CSEM survey, the receivers are rotated to the towline direction. Furthermore, the reciprocity principle is used to flip the role of receivers as transmitters for efficient computations. Since BCs are the same for a vertical and horizontal electric dipole oriented perpendicular to the strike direction, the system matrix for any arbitrarily oriented electric dipole in a plane perpendicular to the strike direction will be the same. An element (p^{th} row and q^{th} column) of Jacobian is defined as

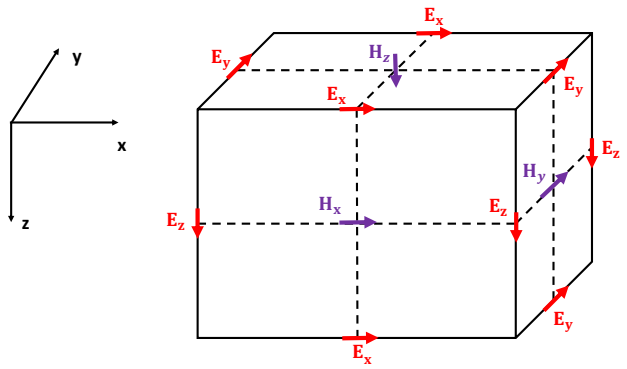

Fig. 2.3 Schematic diagram depicting the staggered grid utilized for discretization where electric field components E_x, E_y and E_z are assigned at midpoint of edges and magnetic field components H_x, H_y and H_z are defined at center of cell faces.

$$J_{p,q} = \frac{\partial \mathbf{F}(\mathbf{m})_p}{\partial m_q}, \tag{2.22}$$

where subscript $_p$ and $_q$ represent the p^{th} simulated data point and q^{th} model parameter. The $J_{p,q}$ element can be calculated by differentiating equation (2.21) and transforming the differentiation of the electric term to the observed field at the receiver position as

$$J_{p,q} = \mathbf{T}\frac{\partial \mathbf{e}}{\partial m_q} = -\mathbf{T}\mathbf{A}^{-1}\frac{\partial \mathbf{A}}{\partial m_q}\mathbf{e}, \tag{2.23}$$

where **T** is a matrix that interpolates and transforms the derivative of an electric field to the observed data type at receiver locations. The matrix derived from the differentiation of the system matrix is very sparse, and the number of non-zero elements also depends on the number of y grids as conductivity is invariant in the y-direction. In the case of VTI, the differentiation of **A** is calculated separately for horizontal and vertical conductivities. Now, by assembling all the elements, the Jacobian matrix can be expressed as

$$\mathbf{J} = \mathbf{T}\mathbf{A}^{-1}\mathbf{G}, \tag{2.24}$$

where

$$\mathbf{G} = \left[\left(-\frac{\partial \mathbf{A}}{\partial m_1}\mathbf{e}\right)\left(-\frac{\partial \mathbf{A}}{\partial m_2}\mathbf{e}\right)\ldots\left(-\frac{\partial \mathbf{A}}{\partial m_n}\right)\mathbf{e}\right]. \tag{2.25}$$

Since the matrix **G** depends on the nodal field, it needs to be computed separately for each source position and type. Now by taking the transpose of equation (2.24), we get

$$\mathbf{J}^T = \mathbf{G}^T\mathbf{A}^{-T}\mathbf{T}^T = \mathbf{G}^T\mathbf{R}, \tag{2.26}$$

where $\mathbf{R}$ is matrix containing the adjoint field. In our algorithm, first, forward and adjoint fields are computed, and subsequently, the equation (2.19) is solved using a conjugate gradient iterative solver to obtain approximate updated model parameters. Further, the real and imaginary parts are treated as independent data points to recast the problem into a real algebra, leading to mapping from a real space (having the dimension of data points) to a real space (possessing the dimension of the number of model parameters). The procedure mentioned in Dehiya et al. (2017) is followed in this study for the model update calculations. A cooling approach is used for the regularization parameter as $\lambda_i = \lambda_{i-1}/1.5$. If the value of objective functional increases in any iteration, the correction term is damped as, $\mathbf{m}_i = \gamma\mathbf{m}_i + (1-\gamma)\mathbf{m}_{i-1}$, where γ is estimated using a line search approach. PARDISO direct solver Schenk and Gärtner (2004) is employed for solving the system matrix for both forward and adjoint responses. The proposed algorithm is referred to as Space Domain 2D EM (SD2DEM), hereafter.

2.5 Numerical Results

The primary objective of the numerical experiments is to demonstrate the accuracy and robustness of the developed algorithm and examine the optimum number of grids required to discretize the space in the y-direction. Two tests, the first using synthetic data and the second considering field data, are presented for numerical experiments. Three scenarios employing 6, 8, and 10 grids for the discretization in the y-direction are analyzed for both data sets. All the experiments presented in this study are executed on Precision 3640 workstation with an intel core i7-based CPU with 64 GB RAM and eight physical cores. All the programs are run using parallel computing employing eight threads. The developed algorithm is parallelized using an openMP library. For the synthetic test, data consist of three frequencies, 0.1, 0.25, and 1.0 Hz, and were simulated using Dehiya (2021) code for a VTI resistivity model shown in Figure (2.1). The data were simulated for seven receivers separated by 1km and placed on the seafloor covering the central 6 km. The transmitter is towed 30 m above the seafloor, and the data were simulated using a 100 m transmitter spacing covering a 10 km distance.

For the SD2DEM algorithm, simulation is performed using 100 m and 25 m grid spacing in x- and z-direction. Seven grids are padded on all sides of x and z-directions, respectively. For the discretization in the y-direction, we have taken the first grid spacing the same as in the x-direction, which is 100 m. Subsequently, the grid spacing increases by

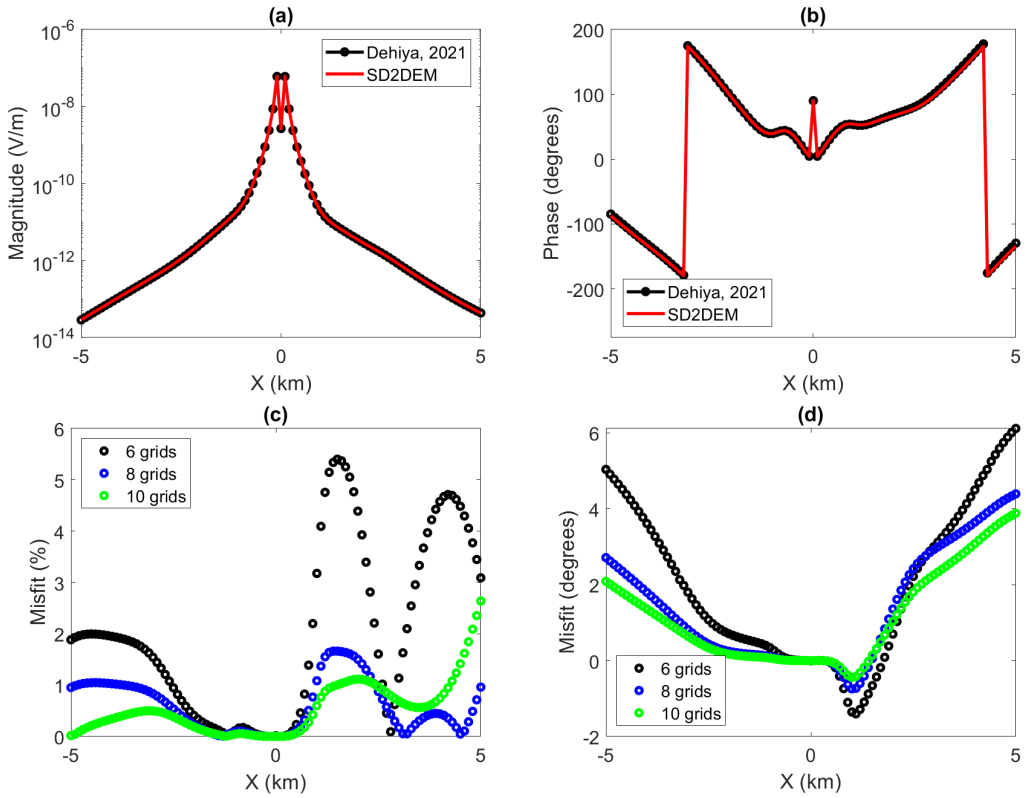

Fig. 2.4 Forward-modeling code benchmarking; (a) Magnitude plots for a receiver at x =-0.0 km simulated using Dehiya (2021) and SD2DEM algorithm using eight grids in strike direction; (b) Phase plots for a receiver at x =-0.0 km simulated using Dehiya (2021) and SD2DEM algorithm using eight grids in strike direction; (c) relative percentage error in magnitude; (d) phase difference plots.

a factor such that the domain boundary reaches around 15 km from the source location. The domain dimension in the y-direction depends on the largest skin depth likely for the data to be analyzed. Therefore, a representative resistivity of the host medium and lowest frequency can be used to compute its value. Generally, the domain size in the y-direction has the same dimension as the grid padding region in the x-direction. Therefore, strategies used in choosing the grid padding can be applied to find the optimum discretization in the y-direction. It is instructive to re-emphasize that the number of model parameters for inversion depends only on the discretization in the x and z directions, as the conductivity does not vary in the y-direction.

For benchmarking, the amplitude and phase comparison plots for 1.0 Hz signal concerning a receiver located at x=0.0 km for the eigth y-grids case along with the responses computed using Dehiya (2021) are shown in Figure (2.4a) and Figure (2.4b), respectively. The relative percentage error in magnitude for all three y-grids scenarios is calculated and

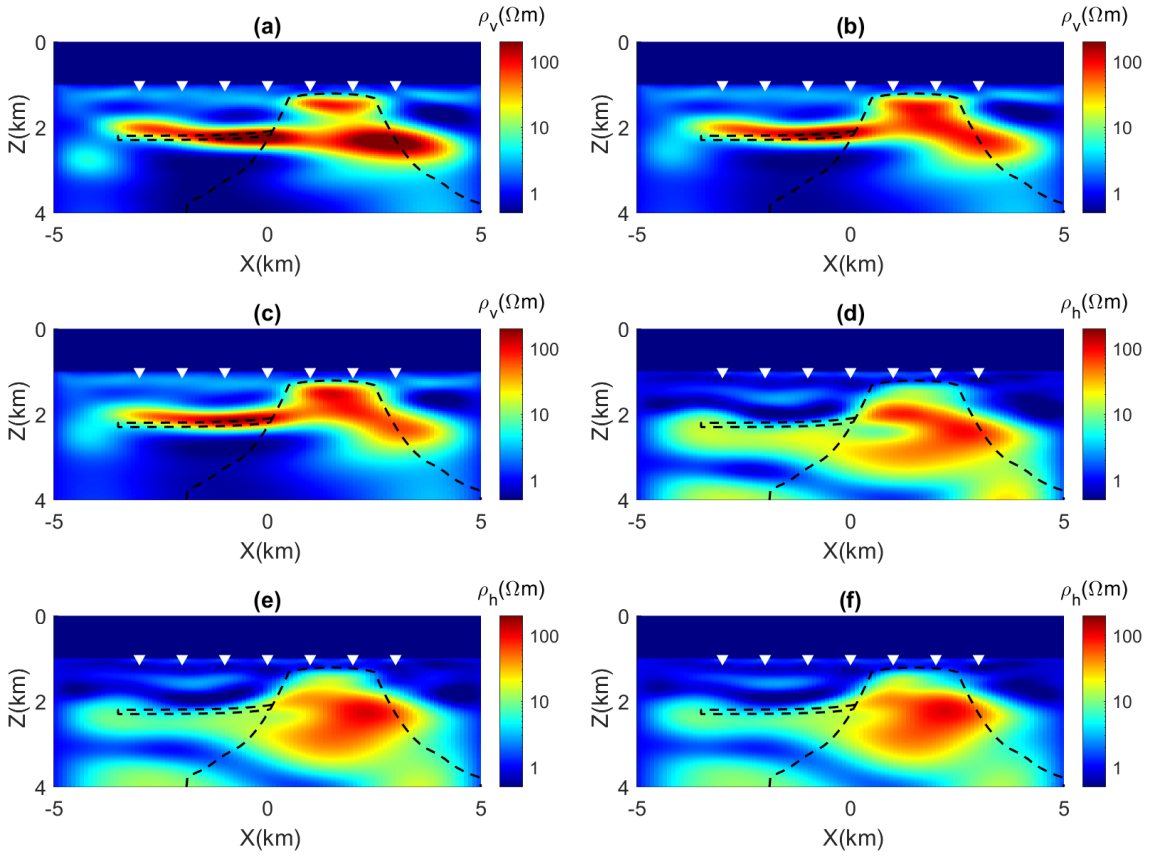

Fig. 2.5 Inverted resistivity models obtained using 2D anisotropic inversion of synthetic data for varying numbers of grids in strike direction; here, inverted-solid triangles represent the receiver's positions and dashed-black lines denote the salt dome and reservoir positions; (a) ρ_v model of the 6-grid case ; (b) ρ_v model of the 8-grid case; (c) ρ_v model of the 10-grid case; (d) ρ_h model of the 6-grid case ; (e) ρ_h model of the 8-grid case; (f) ρ_h model of 10-grid case.

illustrated in Figure (2.4c). The maximum relative percentage error is 3% for 8, and 10 y-grids, whereas it increases to around 5% for the six y-grids case. The phase difference is within $\pm 4^o$ for for 8, and 10 y-grids and $\pm 6^o$ for the six y-grids case as shown in Figure (2.4d). Therefore, SD2DEM delivers a numerical acceptable response, particularly for eight or more grids in the y-direction.

For the inversion experiment, the synthetic data is corrupted by 3% Gaussian noise. The initial model is taken as a half space of 1.5 Ωm resistivity for both horizontal and vertical models. The inverted models for all inversion run after the nRMS reaches 3 % are shown in Figure (2.5). The recovered resistivity models are mostly identical, except for a little difference in the model with six y-grids inversion. To analyze the data misfit, the histogram of the amplitude ratio of predicted to observed data for initial and final inverted

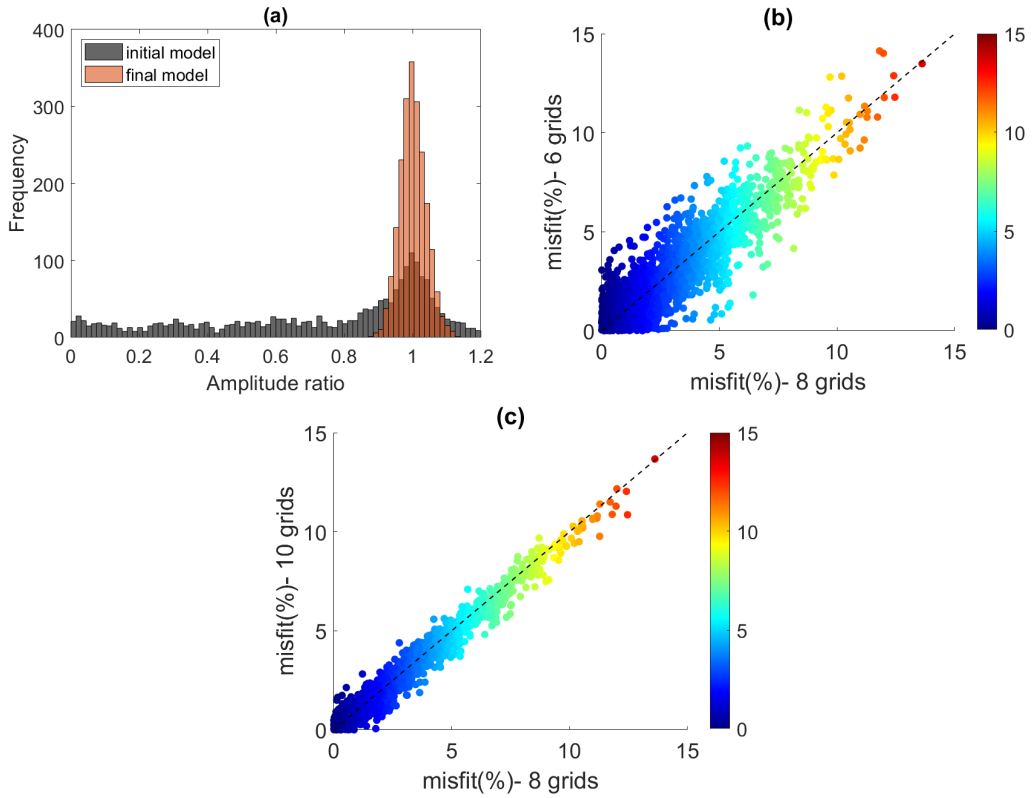

Fig. 2.6 Data misfit plots for synthetic data inversion experiments; (a) amplitude ratio's histogram of predicted data to the initial and final inverted model using 8 grids in strike direction; (b) cross plot of data misfit (%) for 8 grids vs. 6 grids; (c) cross plot of data misfit (%) for 8 grids vs. 10 grids.

models for eight y-grids is shown in Figure (2.6a). The histogram for the final-inverted model shows no bias in data fit as it is nicely distributed around one, where a ratio equal to one represents perfect data fit. The cross plot of data misfit for eight y-grids vs. the six and ten y-grids are shown in Figures (2.6b) and (2.6c), respectively. The scatter of data misfit for eight vs. ten is more narrowly aligned analog at 45^o line, illustrating a highly identical data fit for eight and ten y-grids cases compared to the six y-grids inversions run even though six y-grids case shows no bias either. These observations are explained by relatively higher misfit for the six y-grids modeling (see Figure 2.4). These results demonstrate that around eight unequispaced grids are good enough for discretization in the y-direction, however, smaller number of grid also deliver reasonable model and misfit.

The real-field data include more complex noise characteristics and realistic subsurface resistivity distribution. Therefore, it is instructive to test the algorithm on field data to test its versatility. The Troll field data recorded along northern most towline oriented in a East-West direction (see Figure 2 in Gabrielsen et al. (2009)) is presented in this study.

The reservoir in the Troll field consists of cyclic shallow-marine sandstones and is located in eastward-tilted fault blocks at a depth of around 1.5 km below the seafloor Halbouty (1992). The Troll CSEM data used in this study consists of an inline electric field recorded at five receivers and 237 transmitter locations containing 0.25 Hz, 0.75 Hz, and 1.25 Hz frequencies. The SD2DEM algorithm requires the transmitter to be at $y = 0$ m and receivers to be at $y \geq 0$ m. Hence, the y-coordinates of a transmitter and receivers are subtracted by the transmitter's y-coordinate. For a 2D model, the actual position of a transmitter and receivers in the y-direction does not matter, and only the relative distance of the transmitter and receivers in the strike direction affects the modeling response. Therefore, the repositioning of transmitters and receivers will have no impact on forward and adjoint calculations. This transformation may yield some of the receiver's y-coordinates as negatively valued, which is not permitted in the SD2DEM algorithm. However, we can use boundary conditions given in equation (2.11) and equation (2.12) to address this issue. Since the E_x and E_z components are symmetric and E_y is antisymmetric about plane $y = y_s$. Consequently, by taking the absolute value of the receiver's y-coordinates and reversing the sign of angles that define the deviation of the receiver from plane $y = y_s$, the receiver's y-coordinates can be made positively valued. This straightforward repositioning and reorientation of the transmitter's y-coordinates are done during the data preparation step before inversion. For inversion, the subsurface model is discretized by 200 m and 25 m grid spacing in x- and z-directions, respectively. Three scenarios for y-grids as applied in synthetic data are experimented with. The coefficient β is set equal to zero. All the inversion runs converge to a comparable nRMS ($7.40\% \pm 0.01$) after 12 inversion iterations. The vertical and horizontal resistivity models for all three inversion runs are shown in Figure (2.7). The recovered resistive anomaly matched well with the gas reservoir, which has its top at around 1.35 km Gabrielsen et al. (2009). The histogram and the cross plots, as described in the synthetic experiment, are also generated for Troll data inversion and shown in Figure (2.8). The results of real-field data inversion agree well with the conclusion drawn from the synthetic data. Therefore, both the inversion tests illustrate that one may need around eight grids in the y-direction for this algorithm to deliver optimum results.

2.5.1 Benchmarking of SD2DEM

To benchmark SD2DEM code, a comparison with a wavenumber-domain inversion algorithm, MARE2DEM Key (2016) using Master version, is presented here. The SD2DEM and MARE2DEM have several differences; therefore, the impact of space-domain simulations may not be accounted for exactly. For clarity, first, the main differences between these algorithms are discussed. The MARE2DEM used a wavenumber domain modeling code

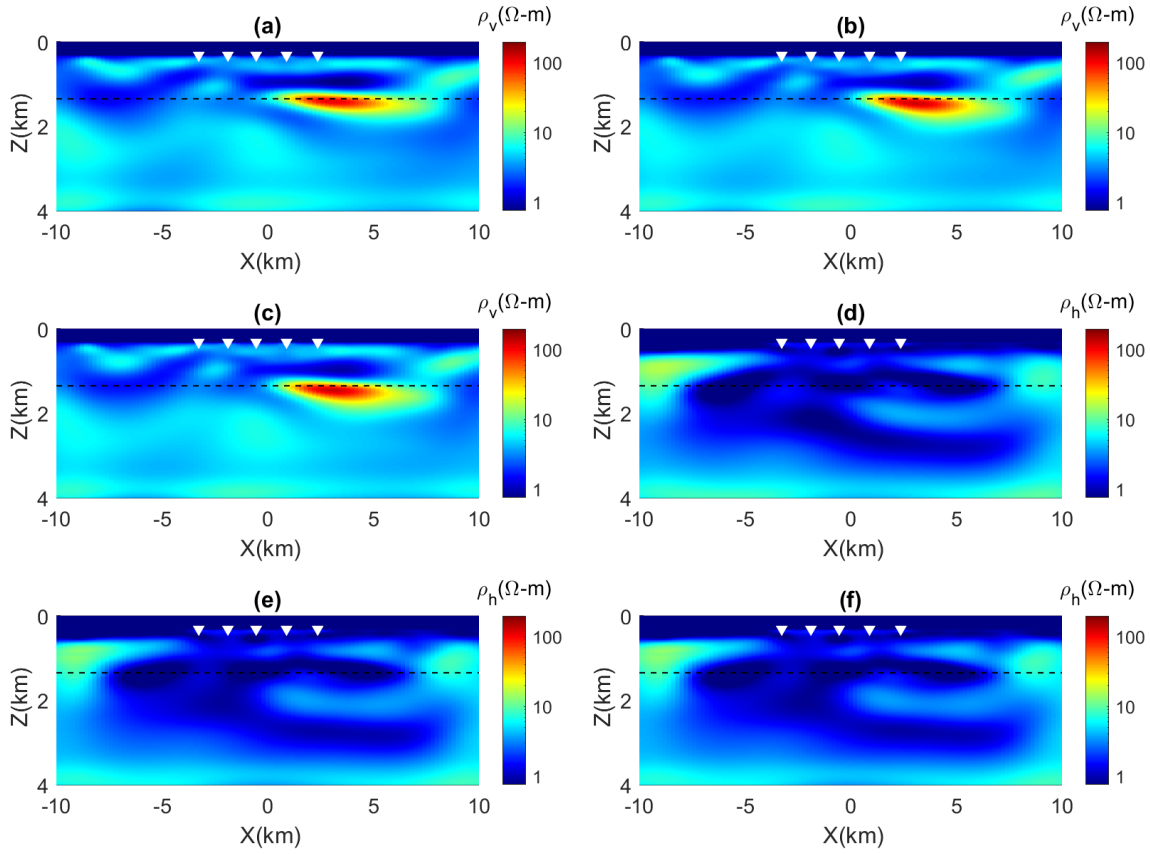

Fig. 2.7 Inverted resistivity models obtained using 2D anisotropic inversion of Troll field CSEM data for varying numbers of grids in strike direction; here, inverted-solid triangles represent the receiver's positions and dashed-black line sketched at 1.35 km illustrates the top of the gas reservoir; (a) ρ_v model of 6-grid case ; (b) ρ_v model of 8-grid case; (c) ρ_v model of 10-grid case; (d) ρ_h model of 6-grid case ; (e) ρ_h model of 8-grid case; (f) ρ_h model of 10-grid case.

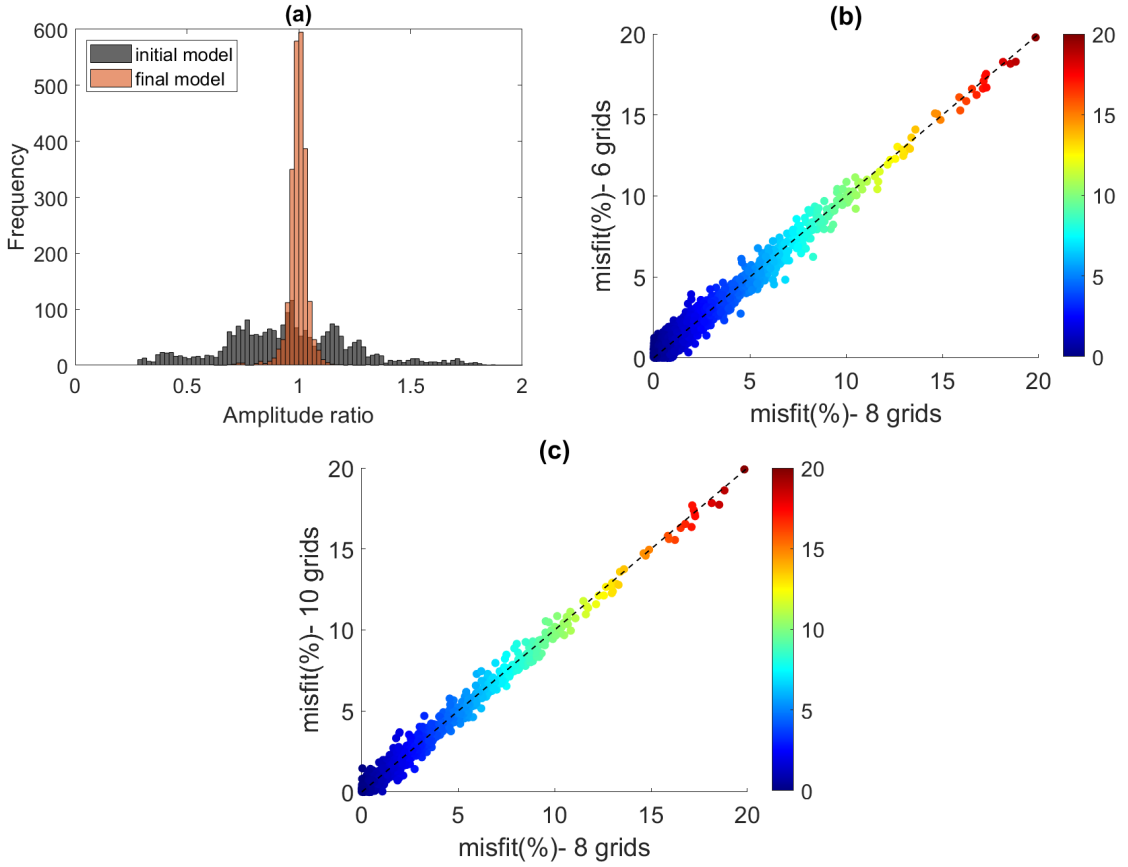

Fig. 2.8 Data misfit plots for Troll field CSEM data inversion experiments; (a) amplitude ratio's histogram of predicted data to the initial and final inverted model using 8 grids in strike direction; (b) cross plot of data misfit (%) for 8 grids vs. 6 grids; (c) cross plot of data misfit (%) for 8 grids vs. 10 grids.

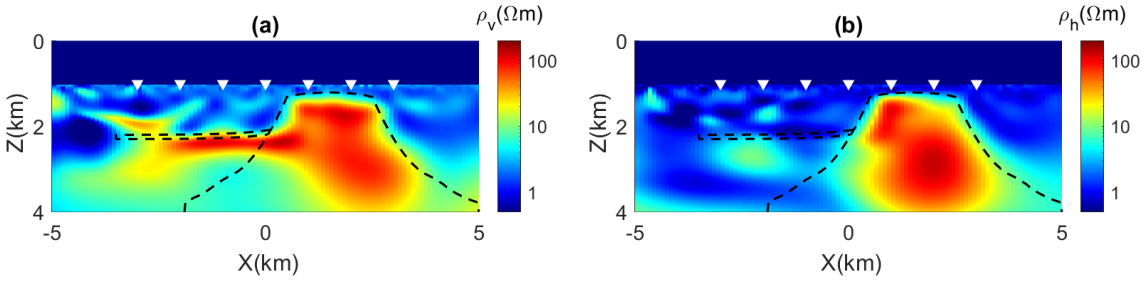

Fig. 2.9 Inverted resistivity models obtained using 2D MARE2DEM inversion code of Synthetic EM data; (a) vertical resistivity; (b) horizontal resistivity.

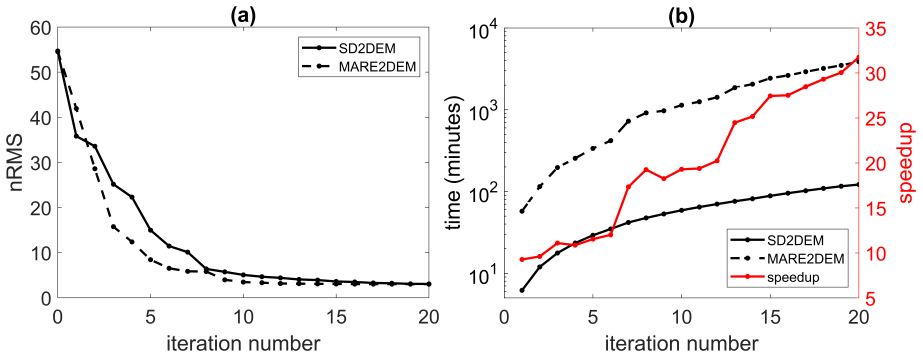

Fig. 2.10 nRMS (in %) plot and time comparison between SD2DEM and MARE2DEM of synthetic EM data; (a) nRMS plot; (b) time efficiency comparison plot.

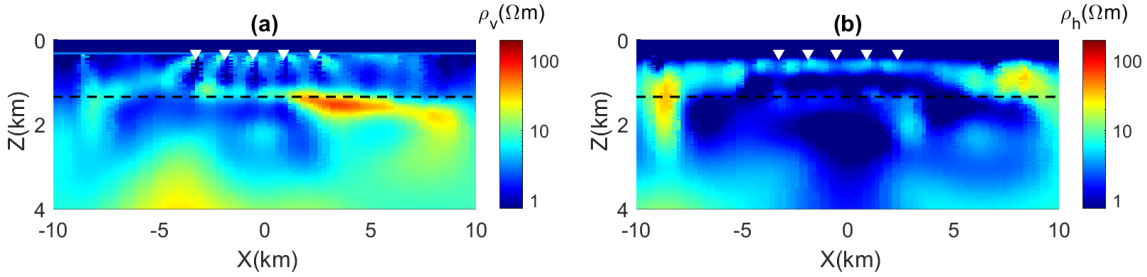

Fig. 2.11 Inverted resistivity models obtained using 2D MARE2DEM inversion code of Troll EM data; (a) vertical resistivity; (b) horizontal resistivity.

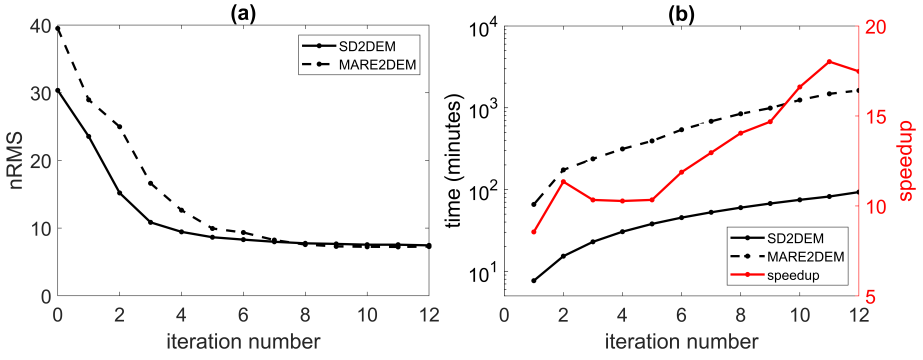

Fig. 2.12 nRMS(in %) plot and time comparison between SD2DEM and MARE2DEM of Troll EM data; (a) nRMS plot; (b) time efficiency comparison plot.

Key and Ovall (2011) based on the finite element method with adaptive grid refinement for forward/adjoint simulations. It employs Occam's inversion scheme for inverse modeling. However, it only search for optimum regularization parameters if the misfit is not reduced considerably. Thus, it may operate like a Gauss-Newton optimization at many iterations. It can consider data in several formats, but the option in the available code works on fitting the log base 10 of magnitude and phase in degrees as data. Wheelock et al. (2015) has shown the benefits of such representation of data in EM inversion. The MARE2DEM computes the full Jacobian matrix and solves it using a direct solver. In contrast, the SD2DEM is a finite difference-based space domain algorithm. It utilizes the Gauss-Newton optimization method, where one hundred conjugate gradient iterations are used for numerical tests presented in this study. Therefore, the Jacobian is not assembled completely, and the Hessian is solved only approximately. In SD2DEM, the regularization parameter is computed using a cooling approach, and no search method is employed to find an optimum regularization parameter. Both algorithms have similar regularization strategies, but there may be some differences in actual implementation. For benchmaring both the synthetic and Troll field data is inverted using MARE2DEM. We made the utmost effort to minimize the difference using user inputs for the inversion experiments presented in this study. Therefore, the inversion domain in x and z direction for MARE2DEM is taken as same as SD2DEM. The synthetic data concerning the salt dome model is inverted using MARE2DEM using magnitude (in log base 10) and phase. The model is discretized using rectangular cells of 100 m and 25 m in the x- and z-direction, respectively, as in the case of SD2DEM experiments. Therefore, the number of unknown model parameters for MARE2DEM is same as the SD2DEM test. Outside the inversion domain, the model is discretized using an unstructured grid generated automatically using the MARE2DEM utilities. The inversion is performed for the VTI case without prejudicing a similarity between vertical and horizontal resistivities. The smoothing factors for both vertical and horizontal directions are equal to one, as in the case of SD2DEM experiments. The recovered resistivity models for the MARE2DEM inversion run after 20 iterations are shown in Figure (2.9). The salt body is recuperated very well by MARE2DEM inversion, delivering a better geometry of the salt body than the SD2DEM inversion. The SD2DEM algorithm finds it a little tricky to image the vertical resistivity of the deep part of the salt body. On the other hand, the reservoir is imaged relatively better in the case of the SD2DEM algorithm. One of the most likely circumstances for differences could be the consideration of log magnitude and phase as data in MARE2DEM while SD2DEM fit the real and imaginary parts of data. One inherent factor for the difference could be how these two approaches applied the data weights. The complex data fitting weighted by the absolute value of the

corresponding datum tends to favor the bigger element between the real and imaginary parts of the datum. Therefore, such an algorithm penalizes the smaller elements between real and imaginary parts of the datum, which may contain valuable information in the case of complex models such as the present one. Wheelock et al. (2015) discussed a 2D magnetotelluric experiment to compare inversion using complex impedance tensors and a log of apparent resistivity plus phase. Nonetheless, a detailed investigation of these issues for CSEM data still needs to be studied. To compare the convergence of data fitting, the nRMS for MARE2DEM inversion is recomputed as per the definition given in equation (2.20) using the response calculated at each iteration. The nRMS plot for MARE2DEM and SD2DEM inversion run using eight y-grids are shown in Figure (2.10a). Both algorithms show a comparable convergence and converge to the nRMS value as three after 20 inversion iterations. Therefore, the proposed algorithms perform well in terms of data fitting compared to the wavenumber domain inversion algorithm. Figure (2.10b) shows the computation times after each iteration for both algorithms and the speedup factor defined as the ratio of MARE2DEM time to SD2DEM time. Since the MARE2DEM involves searching for the optimum regularization factor at some iterations, the computation cost for MARE2DEM may vary from iteration to iteration. The SD2DEM (with eight y grids case) shows roughly a thirty-time reduction in computation time for this experiment. Therefore, the proposed algorithm outperforms a wavenumber domain algorithm in terms of computation efficiency. The peak memory usage for SD2DEM is 12.6 GB, where two-thirds of memory use is due to the direct solver application in forward/adjoint computation. The maximum memory utilization for MARE2DEM is 30.6 GB, which peaks during the formation of the Jacobian matrix. However, it is instructive to state again that the efficiency may not be fully attributed to space domain computation alone.

Troll data using the MARE2DEM algorithm was also inverted, employing rectangular cells with the same dimension as in the case of SD2DEM Troll experiments to keep the number of unknown model parameters the same for both algorithms. The recovered resistivity models after 12 iterations of VTI inversion without prejudicing a similarity between vertical and horizontal resistivities are shown in Figure (2.11). The reservoir is imaged at the correct depth window in the vertical resistivity model. However, the obtained inverted model shows more artifacts compared to SD2DEM inversion results. The nRMS plot for MARE2DEM (recomputed as per equation (2.20)) and SD2DEM inversion run using eight y-grids are shown in Figure (2.12a). Both algorithms show a comparable convergence and converge to the nRMS value of 7.4% after 12 inversion iterations. Figure (2.12b) shows the computation times for both algorithms and the speedup factor. The SD2DEM (with eight y grids case) shows around a sixteen-time drop in computation

time for Troll field data. The highest memory utilized for SD2DEM and MARE2DEM is 20.0 GB and 33.6 GB, respectively, for the Troll field experiment. Therefore, in terms of computation efficiency, the proposed algorithm is more than one order faster and uses roughly 1.6–2.4 times less memory compared to MARE2DEM with an equivalent nRMS convergence. The computation and memory analysis of SD2DEM indicated that both computation time and memory requirements increase almost linearly with number of y-grids. Quantitatively, the computation time and memory requirement increase by a factor of roughly 1.36 and 1.28 times per y grid, respectively. The MARE2DEM performs better in terms of model recovery for the salt dome model. However, the SD2DEM delivers a smoother model for Troll field data than MARE2DEM. Besides, in SD2DEM, there is no limitation on the receiver's deviation in strike direction, or the requirement of projecting the receives onto the transect, as may be the case of wavenumber-domain algorithms. For example, in MARE2DEM, if the along-strike source-receiver offset is large, the choice of wavenumber is advised to be benchmarked using a 1D modeling response. In a nutshell, the algorithm development and execution of the proposed algorithm are very straightforward and deliver efficient computation and reasonable convergence. Due to the efficiency of the proposed space domain algorithm, it can potentially be developed for unstructured grids as well. Furthermore, a space domain modeling algorithm may be employed in other inversion schemes, such as Bayesian inversion, as efficient computation is essential for such optimization techniques.

2.6 Conclusion

A novel space-domain 2D CSEM inverse modeling algorithm is developed in this study. A new set of boundary conditions is derived for the plane perpendicular to the strike direction that passes through the transmitter position. These boundary conditions are derived using the electromagnetic field components' symmetric/antisymmetric characteristics about the plane mentioned above. A space-domain forward modeling algorithm is developed employing these boundary conditions. A comparison of the simulated response with a published algorithm's responses reveals that around eight grids are sufficient for the discretization of space in the strike direction for numerical accuracy required in electromagnetic data analysis. Furthermore, a Gauss-Newton-based inversion code is developed, utilizing the proposed modeling algorithm for forward and adjoint computations. The inversion experiments using synthetic and real field data also indicate that around eight grids are sufficient for discretization in the strike direction. The numerical experiments suggest that the proposed algorithm is at least one order faster in computation and re-

quires 1.6–2.4 times less memory than a wavenumber domain algorithm, MARE2DEM. However, it must be stated that the proposed and MARE2DEM algorithms employ very distinct forward and inverse modeling approaches. Therefore, it is not possible to attribute the computational advantages solely to the space domain strategy. Nevertheless, the proposed algorithm is very straightforward to implement as it eliminates the need for inverse Fourier transform in two-dimensional electromagnetic modeling and inversion.

Chapter 3

2D structurally constraint CSEM inversion algorithm

3.1 Abstract

This chapter presents the development and evaluation of a 2D structurally constrained controlled-source electromagnetic inversion algorithm employing the cross-gradient method. Our investigation reveals that structural constraints significantly improve the imaging of complex geological features such as salt domes. However, inaccurate constraints can impact the resistivity distribution obtained by constrained inverse modelling. We also examine the benefit of an initial model based on prior information, including the impact of inaccurate prior. Moreover, minimising the difference between horizontal and vertical resistivity enhances the imaging of deep salt bodies; however, it generates artefacts if the subsurface is anisotropic. The analysis presented in this study emphasises the importance of carefully devising inversion experiments to ensure the usefulness and reliability of subsurface models obtained by the inversion of controlled-source electromagnetics.

3.2 Introduction

Geophysical inverse modelling is a critical tool in subsurface exploration, allowing scientists to infer the physical properties of the Earth's interior from surface measurements. However, this process is inherently non-unique due to the ill-posed nature of inversion; consequently, multiple subsurface models can explain the observed data equally well. This non-uniqueness arises from several factors, including inadequate data coverage, weak sensitivity to some of the model parameters, model discretization, and the method's

resolution, which depend on the underlying physics of the geophysical methods, as each method depends on different physical processes. Consequently, the model derived from inverse modelling depends on the initial model and the regularization technique, due to the non-uniqueness of the inversion process. Additionally, the quantity and quality of the data available and the geometry of the survey conducted also play significant roles in this non-uniqueness. Given these challenges, combining information from multiple geophysical methods has emerged as a powerful approach to mitigate the non-uniqueness, at least partially, in inverse modelling. By integrating data from different techniques, it is possible to leverage the complementary sensitivities of each method to different subsurface properties, thereby providing more robust and constrained models. For example, seismic data struggles to accurately define hydrocarbon saturation, as the change in seismic velocity is minimal after 10-15 % saturation. Therefore, it is challenging to distinguish between commercial and non-commercial reserves. Thus, basing assessments of reservoir potential solely on seismic information may lead to erroneous conclusions. However, on the other hand, the resistivity of rock changes with hydrocarbon saturation. Hence, one potential strategy to improve the accuracy of reservoir models is to conduct controlled source electromagnetic (CSEM) surveys in conjunction with seismic surveys (MacGregor et al., 2001; Sinha, 1999). However, there is no analytical formulation that relates the seismic velocities and the electrical resistivity which causes the joint inversion of CSEM and seismic data challenging.

There are three primary approaches to combining geophysical data, where no analytical relationship exists among the physical property senses by each method. One such approach is direct parameter coupling, which involves creating a cross-property relationship derived from borehole data or petrophysical relationships. This method has been applied successfully in various studies. Panzner et al. (2016) combined the seismic and electromagnetic (EM) data to improve sub-basalt imaging in the Faroe-Shetland Basin by making an empirical relationship between resistivity and the velocity from well-log data. Heincke et al. (2017) combine magnetotelluric, gravity, and seismic data using the petrophysical relationship as a constraint. Inverse modelling is likely to perform very well in such imaging analyses since a relationship between parameters is available. However, the outcome of such a joint inversion heavily depends on the cross-property relationship used during the inversion. Therefore, one needs to have a borehole in the study area that penetrates the depths to be imaged. Complex geological regions where physical properties change rapidly away from the bore may need better well data coverage in the study area. However, in reality, such relationships only approximately match throughout the study area. Furthermore, the well-log data has a different sensitivity scale to small-scale

features than the surface data, making the cross-property relationship only approximately valid. Another approach is structurally coupling joint inversion, which integrates different types of geophysical data based on their structural similarities. This method does not require borehole measurements but comes with complexities in combining datasets with varying resolutions and sensitivities (Gallardo et al., 2012; Gallardo and Meju, 2004; Meju et al., 2003). Colombo and De Stefano (2007) presented a simultaneous joint inversion algorithm to combine seismic, gravity and electromagnetic data. The third approach is the constraint inversions, it utilizes prior subsurface information to perform a single physics-based data inversion. Prior knowledge of the subsurface can be used in numerous ways during inversion. For example, it can be used to create an initial guess model which is in proximity to the global minima as the gradient-based inversion converges to the nearest minima. The prior information can be explained by designing the regularization operator for inverse modelling to steer the model as per prior information. One valuable use is enforcing structural similarity on the inverted model using prior information employing the cross-gradient-based regularization technique. Saunders et al. (2005) developed a structurally constrained CSEM inversion algorithm based on the seismic structural data. Auken et al. (2005) works on a piecewise one dimensional laterally constrained inversion algorithm of resistivity data based on layered earth model. An image-guided inversion algorithm of electrical resistivity data developed by Zhou et al. (2014) where structural information is obtained directly from a guiding image.

In this study, we present the development of a structurally constrained CSEM inversion algorithm and exhaustive analysis to test the pros and cons of such an inversion application. The main focus is to find the best practices to be followed while working with such inversion algorithms for CSEM data inversion. For the algorithm development part, the SD2DEM code presented in the previous study is augmented with the functionality of applying structural constraints on 2D CSEM inversion. The rest of the chapter is as follows. First, the theory of structural coupling using a cross-gradient approach is presented. The second part is the numerical experiments, which is the main focus of this study, and the chapter ends with a conclusion.

3.3 Methodology

To develop a structurally constrained inversion algorithm, the objective function is modified by augmenting an additional regularization term to incorporate the prior information into our SD2DEM inversion algorithm. A cross-gradient approach is used to apply the structural similarity. Therefore, the functional given in equation (2.15) can be modified as

$$\phi_{joint} = ||\mathbf{W}_d(\mathbf{d}^{obs} - \mathbf{F}(\mathbf{m}))||_2 + \lambda(||\mathbf{Rm}||_2 + \beta||\mathbf{Lm}||_2 + \gamma||\mathbf{Km}||_2) \tag{3.1}$$

where $\mathbf{d}^{obs}$ denotes the observed data, $\mathbf{F}(\mathbf{m})$ denotes the predicted data , $\mathbf{W}_d$, denotes data covariance matrix; λ is regularization parameter; $\mathbf{R}$ denotes second order derivative (Laplacian) operator; $\mathbf{L}$ is an operator that seek to minimize the difference between horizontal and vertical conductivity; β and γ are the positive scalars and $\mathbf{K}$ is an operator that define the cross gradient function which can be expressed as

$$||\mathbf{Km}||_2 = ||\nabla\mathbf{m} \times \nabla\mathbf{m}_{ref}||_2 \tag{3.2}$$

where $\mathbf{m}_{ref}$ is a model derived from the prior information obtained from other geophysical methods. By including the 2-norm of cross-product of gradients of the prior model and unknown parameter vector, the unknown parameters can be constrained to have a similar structure as the prior model. The benefit of such a functional is that it does not enforce conductivity contrast at all the interface of the prior model. It occurs because the cross-product can be zero if one of the gradients is zero or both gradients are identical directionally. Therefore, the optimization would not enforce resistivity interfaces at all contrasting horizons of the prior model. An expression for estimation of correction in the model parameter, $\delta\mathbf{m}_i$, at i^{th} iteration by using the Gauss-Newton method for the above-stated functional can be written as

$$\mathbf{H}_{i-1}\delta\mathbf{m}_i = -\mathbf{g}_{i-1}, \tag{3.3}$$

where

$$\mathbf{H}_{i-1} = \mathbf{J}_{i-1}^T\mathbf{W}_d^T\mathbf{W}_d\mathbf{J}_{i-1} + \lambda_{i-1}(\mathbf{R}^T\mathbf{R} + \beta\mathbf{L}^T\mathbf{L} + \gamma\mathbf{K}^T\mathbf{K}), \tag{3.4}$$

and

$$\mathbf{g}_{i-1} = -\mathbf{J}_{i-1}^T\mathbf{W}_d^T\mathbf{W}_d(\mathbf{d}^{obs} - \mathbf{F}(\mathbf{m}_{i-1})) + \lambda_{i-1}(\mathbf{R}^T\mathbf{R} + \beta\mathbf{L}^T\mathbf{L} + \gamma\mathbf{K}^T\mathbf{K})\mathbf{m}_{i-1}, \tag{3.5}$$

where $\mathbf{H}_{i-1}$ and $\mathbf{g}_{i-1}$ represent Hessian and gradient of objective functional computed for the model parameter, $\mathbf{m}_{i-1}$ after $(i-1)^{th}$ iteration and $\mathbf{J}_{i-1}$, is the Jacobian matrix calculated for model parameter, $\mathbf{m}_{i-1}$. An adjoint approach (Mcgillivray and Oldenburg, 1990) is used for Jacobian matrix computation. Finally, the updated model parameter after i^{th} iteration is calculated as, $\mathbf{m}_i = \mathbf{m}_{i-1} + \delta\mathbf{m}_i$. Equation (3.3) can be rearranged for direct computation of the updated model parameter as,

$$\mathbf{H}_{i-1}\mathbf{m}_i = -\mathbf{g}_{i-1} + \mathbf{H}_{i-1}\mathbf{m}_{i-1}. \tag{3.6}$$

The rest of the strategies are the same as discussed in the previous chapter.

3.4 Numerical Results

The numerical experiments are aimed at investigating the effectiveness of the developed algorithm. To test the limit of an algorithm, a problem that is difficult for that algorithm should be experimented with. Therefore, we opted for a synthetic model, which poses an imaging challenge for CSEM methods. CSEM methods are designed to sense thin, resistive bodies with large horizontal dimensions like hydrocarbon reservoirs (Constable, 2010). Salt dome imaging presents a challenge for the CSEM method that's why the magnetotelluric (MT) method is often employed along with CSEM data to image the salt dome. Consequently, the resistivity model used in the previous chapter, as shown in Figure 2.1, is used for the experiments for the present analysis. For evaluating the advantage of the proposed algorithm, its results need to be compared with an inverted model obtained without any structural constraint; therefore, for better comparison, the inverted model obtained in the previous study is shown in Figure 3.1. This model serves as a reference model for the analysis present in this study. It is to be noted that the inversion domain is 10 km by 4 km is defined for inversion, and the grid size is 100 m and 25 m in x- and z-direction, respectively, which is the same as the one employed in synthetic data inversion in the previous chapter. All the user inputs, such as regularization parameter strategy and misfit computation, are the same as in the previous chapter's inversion experiment for the salt dome study. Prior structural information about the subsurface can be included in inversion in many ways. One of the ways to do this is to use it to apply structural constraint via a cross-gradient strategy. The second approach is to generate an initial model using it. Since, in this case, only the geometry of the body is known, the resistivity is assumed to be unknown. Assuming the structural information is derived from the seismic method, we would have some information about the anomaly. For example, in the present case, if it is believed based on the seismic image that the anomaly is a salt body, we can assign a relatively more resistivity to it compared to the host, which is sedimentary rock saturated by marine water, which has a resistivity around 1 Ω-m. Therefore, an initial model for the inversion can be derived by specifying the geometry based on the prior structure and assigning a higher resistivity than the host media. The third strategy could be to deploy an initial guess model based on the prior information and enforce structural constraints using the cross-gradient functional. Furthermore, it is imperative to believe that the structural information will have uncertainties and will not be perfectly accurate. Therefore, it is instructive to experiment using somewhat inaccurate prior information. We test all these scenarios in this numerical experiment section to obtain insight into the effectiveness of the proposed algorithm. Unfortunately, any numerical experiment-based study has a limitation in that the analysis is biased by the experiment design, such as the

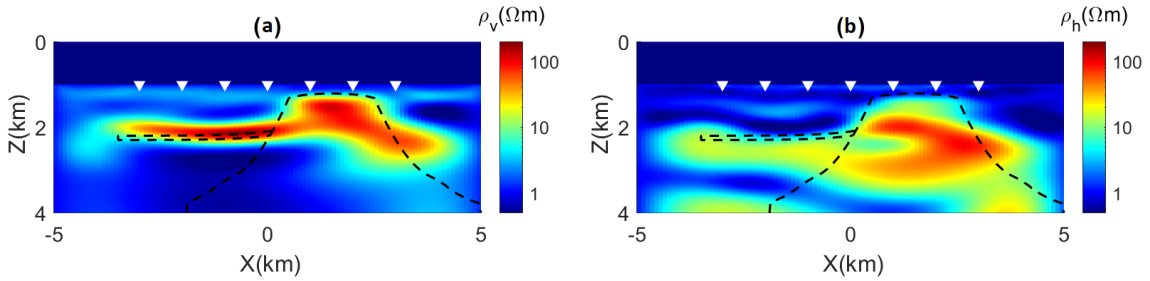

Fig. 3.1 Inverted resistivity models obtained by inversion without any structural constraints; here, inverted-solid triangles represent the receiver's positions and dashed-black lines denote the salt dome and reservoir positions; (a) ρ_v; (b) ρ_h.

choice of synthetic model and survey parameters which is also the shortcoming of the present analysis. However, we try to make the current analysis detailed so that some broad observations can be obtained.

3.4.1 Structural constraint on the salt dome

For the first experiment, we incorporated accurate structural information of the salt dome as constrainet into the CSEM inversion algorithm. This assumption is not realistic as the shape of deeply buried bodies is not known accurately. However, this experience serves the purpose of the best-case scenario; therefore, it provides a benchmark for other tests. For inversion, the initial model is taken as a half-space of 1.5 Ωm resistivity for both horizontal and vertical models. The scaling factor for cross-gradient, γ, is taken as 50. We have tested its values as 1, 10, 50, and 100. γ=50 is found to be suitable for our inversion, and the same is used for all the experiments in this chapter. After the nRMS reaches 3 %, the inverted models are considered the final model as the synthetic data is contaminated by 3% Gaussian noise. The vertical and horizontal resistivity models estimated by this inversion run are shown in Figures (3.2a) and (3.2b), respectively. The comparison of these inverted models with unconstrained inversion (Figure 3.1) clearly shows the advantage of structurally constrained inversion. The structurally constrained inversion successfully compels the salt body into its boundaries. However, the boundaries are not as sharp as those of the synthetic model. The smoothness constraints that are applied to stabilise the inversion process cause the smooth interface of anomalies. Therefore, the regularization term includes functionals with competing goals. We have also observed relatively slower convergence in the case of constrained inversion than unconstrained inversion. We postulate that it is due to conflicting regularization terms, but we are unable to prove it. The next objective is to test a realistic situation where the shape of the salt body is only

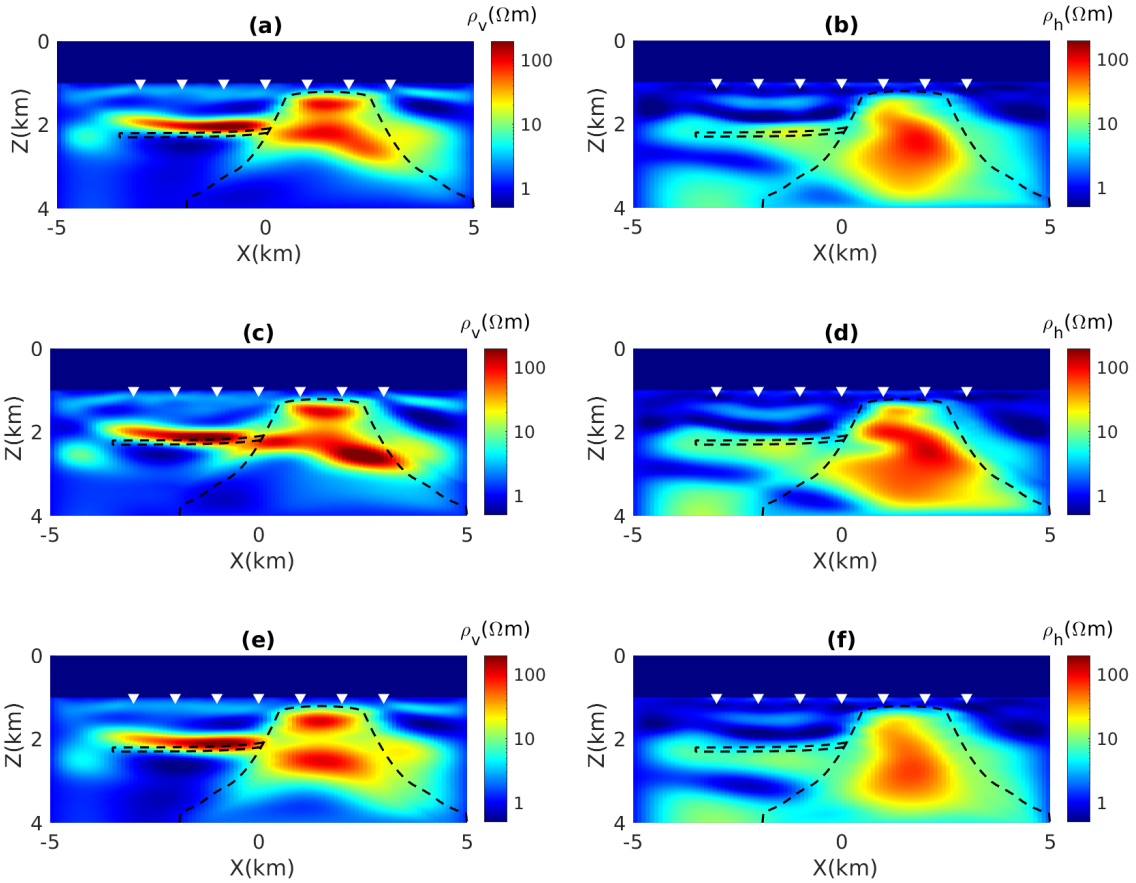

Fig. 3.2 Inverted resistivity models obtained by applying structural salt dome constraints; here, inverted-solid triangles represent the receiver's positions and dashed-black lines denote the salt dome and reservoir positions; (a) ρ_v (accurate); (b) ρ_h (accurate); (c) ρ_v (inaccurate: broadened+500m, shifted up 50m); (d) ρ_h (inaccurate: broadened+500m, shifted up 50m); (e) ρ_v (inaccurate: shrunkned+500m, shifted down 50m); (f) ρ_h(inaccurate: shrunkned+500m,shifted down 50m).

known approximately. Therefore, an error is included in the structure of the prior model. Additionally, it is assumed that the inaccuracy will be less in the estimate of the position of the top of salt than in the side flanks. We consider two scenarios for inaccurate prior structural models. First, the top of the salt is 50 meters above its actual position, and the flank expands outward by 500 meters maximum at the base. Therefore, the error linearly increases from 50 m at the top to 500 at the base of the salt. For the second case, the top is shifted down by 50 m, and flanks are shrunk inward by 500 m at the base, with structural error going from 50 m at the top to 500 m at the base. The inverted models for the nRMS 3% for both the tests are shown in Figures (3.2c) to (3.2f). The comparison of inverted models of inaccurate structural information with accurate prior illustrates that structural information errors impact the salt body's estimated resistivity. However, the changes are incremental, illustrating the stability of the scheme for error propagation in the estimated model. It is instructive to add that all the inversion results show minimal influence on the imaging of the reservoir.

3.4.2 Structural constraint and initial model derived from prior model for the salt dome

For the second set of experiments, a prior model is used to design an initial model and apply the structural constraint using the cross-gradient technique on the salt body only. For the initial model, the resistivity of the salt body is assigned as 10 Ω-m. This assumption of allocating a higher resistivity is reasonable for the salt bodies as they generally have higher resistivity than host rock in marine environments. Similar to previous experiments, three types of prior information are tested, namely, accurate prior and the two erroneous priores, same as described in the previous subsection. The inverted models for all inversion run after the nRMS reaches 3% are shown in Figure (3.3). All the inversion runs have performed reasonably well, achieving identical data fit, and the inverted models are comparable. Compared to previous experiments, the salt body is mapped up to greater depths for both horizontal and vertical resistivity models. Furthermore, the resistivity in the deeper part is increased towards the actual value, which is 50 Ω-m from the 10 Ω-m prescribed for the initial model. It indicates that the data also senses the deeper part of the salt body. It contradicts the previous experiments, where results indicate that the data only senses the top 3 km salt body in the vertical resistivity model. Thus, we argue that since our algorithm converges to the nearest minima, the change in the initial model leads to a convergence of the inversion to different minima, causing varying vertical resistivity images for these experiments. It raises an important question: Should we use an initial

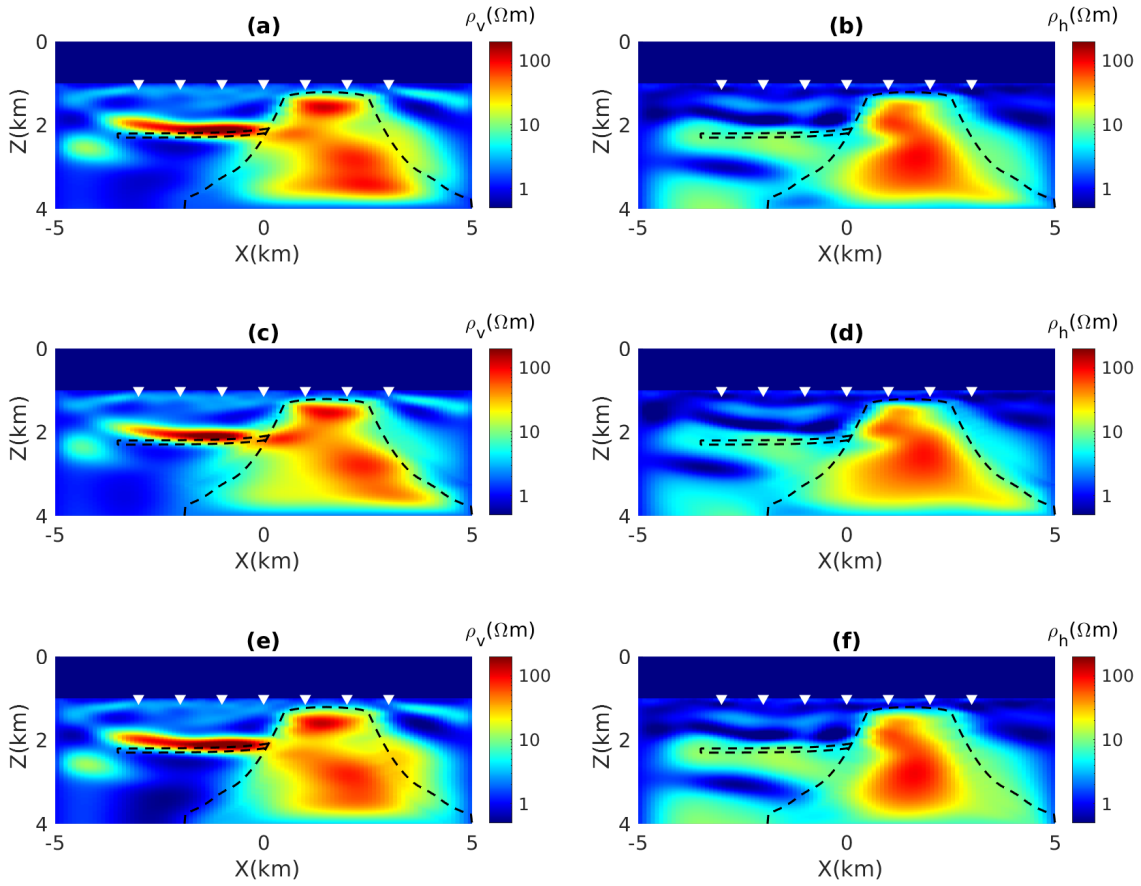

Fig. 3.3 Inverted resistivity models obtained by providing predefined initial models and also applying structural salt dome constraints; (a) ρ_v (accurate); (b) ρ_h (accurate); (c) ρ_v (inaccurate: broadened+500m, shifted up 50m); (d) ρ_h (inaccurate: broadened+500m, shifted up 50m); (e) ρ_v (inaccurate: shrunkned+500m, shifted down 50m); (f) ρ_h(inaccurate: shrunkned+500m,shifted down 50m).

model derived from prior information in case we have considerable uncertainties in the prior information? For the present case, it is expected that the bottom of salt may contain significant uncertainties as imaging the bottom of salt is challenging.

An experiment with a modified synthetic model is performed to examine the limitation of CSEM imaging using constrained inversion with significant errors in the position of the bottom of the salt body. The synthetic model is created by truncating the base of the salt body at 3 km depth, and the CSEM data with the same configuration as the earlier case is simulated. The data was contaminated by 3% Gaussian noise, the same as in the previous case. The data is inverted with the prior, where the salt body is extended up to 4 km with accurate top and side flanks up to 3 km. Therefore, the error in the prior model is

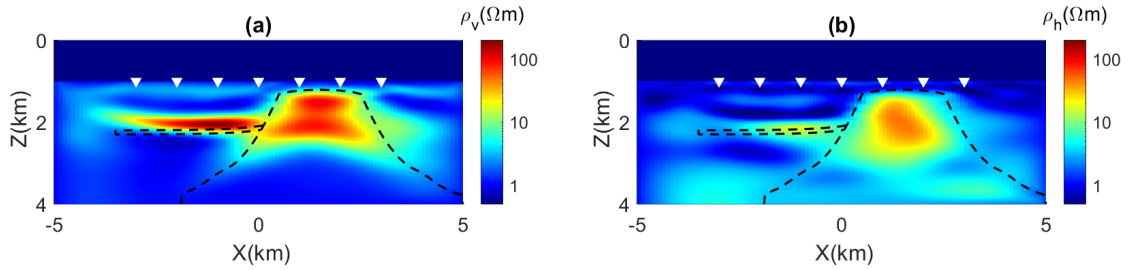

Fig. 3.4 Inverted resistivity model using a half-space initial model with the application of only structural constraints of the salt dome; (a) ρ_v; (b) ρ_h. Note that for the forward simulation, a model representing approximately half of the actual salt dome was used.

only below 3 km depth. First, the inversion is done employing only structural constraint with this prior and using a half-space initial model with a resistivity of 1.5 Ω-m. Figure (3.4) illustrates the obtained inverted model. The results show that the inverted resistivity values were confined within the boundaries of the salt dome, with the top part being well-imaged, and the salt body did not extend up to 4 km as defined in the prior model. In the second experiment, an initial guess model containing a salt body, 10 Ω-m up to 4 km depth in a 1.5 Ω-m host is used along with the structural constraint. The inverted model is depicted in Figure (3.5). The results illustrate that the inversion is not able to update the resistivity under the salt base, and it remains around 10 Ω-m, which is the initial guess model value. It indicates that the simulated CSEM data does not sense the subsurface below the salt body. However, it was observed in the second set of experiments that CSEM data could sense the subsurface below 3 km. Therefore, collectively, all three inversions suggest that CSEM data has a weak sensitivity of the model below 3 km where the salt body is present. Consequently, a good initial guess leads to a more reasonable estimate of the subsurface at those depths. These two experiments lead to important conclusions. First, the results suggest that using a predefined initial model can lead to misinterpretation in case some part of the model is weakly sense by the data. Specifically, the persistence of the initial resistivity value in the inverted model highlights a potential bias introduced by the predefined model, which may not accurately reflect the deeper parts of the salt dome. Second, applying only structural constraints appears to be a more reliable approach as it does not introduce such prejudices. Such a model may lack some information but does not have fictitious anomalies. In summary, while predefined initial models can aid in imaging specific parts of the subsurface, they lead to the risk of misinterpretation if prior information is grossly inaccurate. Therefore, if confidence in the predefined model is lacking, particularly in the weakly sensitive part of the model, it is advisable to avoid its use

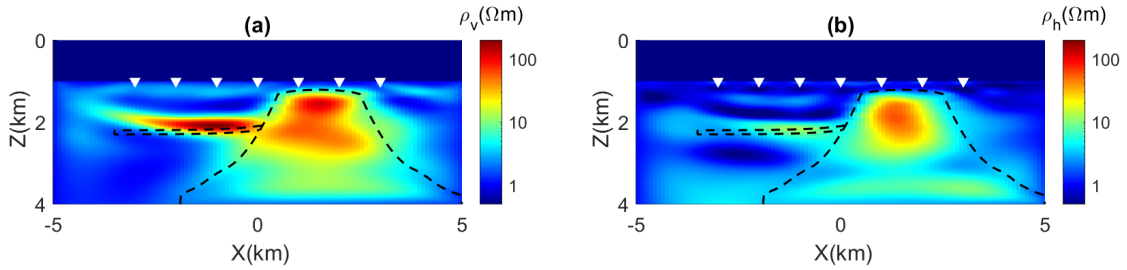

Fig. 3.5 Inverted resistivity model using an accurate salt dome initial model with 10 ohm-m resistivity and no structural constraint; (a) ρ_v; (b) ρ_h. Note that for the forward simulation, a model representing approximately half of the actual salt dome was used.

in the initial model design. Instead, relying solely on structural constraints can provide a more balanced and less biased imaging outcome.

3.4.3 Structural constraint and initial model derived from prior model for the salt dome and reservoir

A structural constraint is applied to both the salt body and the reservoir for this group of experiments. The initial guess model consists of a salt dome and reservoir with 10 Ω-m resistivity. The objective of this investigation is to assess whether the inclusion of predefined information and the application of additional reservoir constraints can enhance the accuracy of the inverted results, particularly for reservoirs. The experiment is performed for three cases that are accurate prior to the salt dome shape and two cases of inaccurate salt dome geometry as described earlier. The position of the reservoir is taken as its actual position for all three cases. The inverted models for all inversion runs after the nRMS reaches 3 % are shown in Figure (3.6). Surprisingly, the reservoir was not confined to the boundaries given in the prior model, which was its actual position and was even included in the initial model. We argue that it is caused by the smoothing regularization function that prevents the sharp boundaries. Since the grid size in the z-direction is 25 m while the reservoir thickness is 100 m, smoothening openers compelled it to be thicker than its actual size. Therefore, the reservoir is mapped just above its actual position to satisfy the smoothening and cross-gradient operator. However, the cross-gradient operator forces the bottom of the imaged reservoir to be concise with the top of the prior model, making it flatter than the previous case. The results of all the above experiments suggest that a 1-norm-based regularization scheme can be tested to replace the smoothing operator-based regularization. Since the 1-norm promotes sparsity, it may allow a sharp

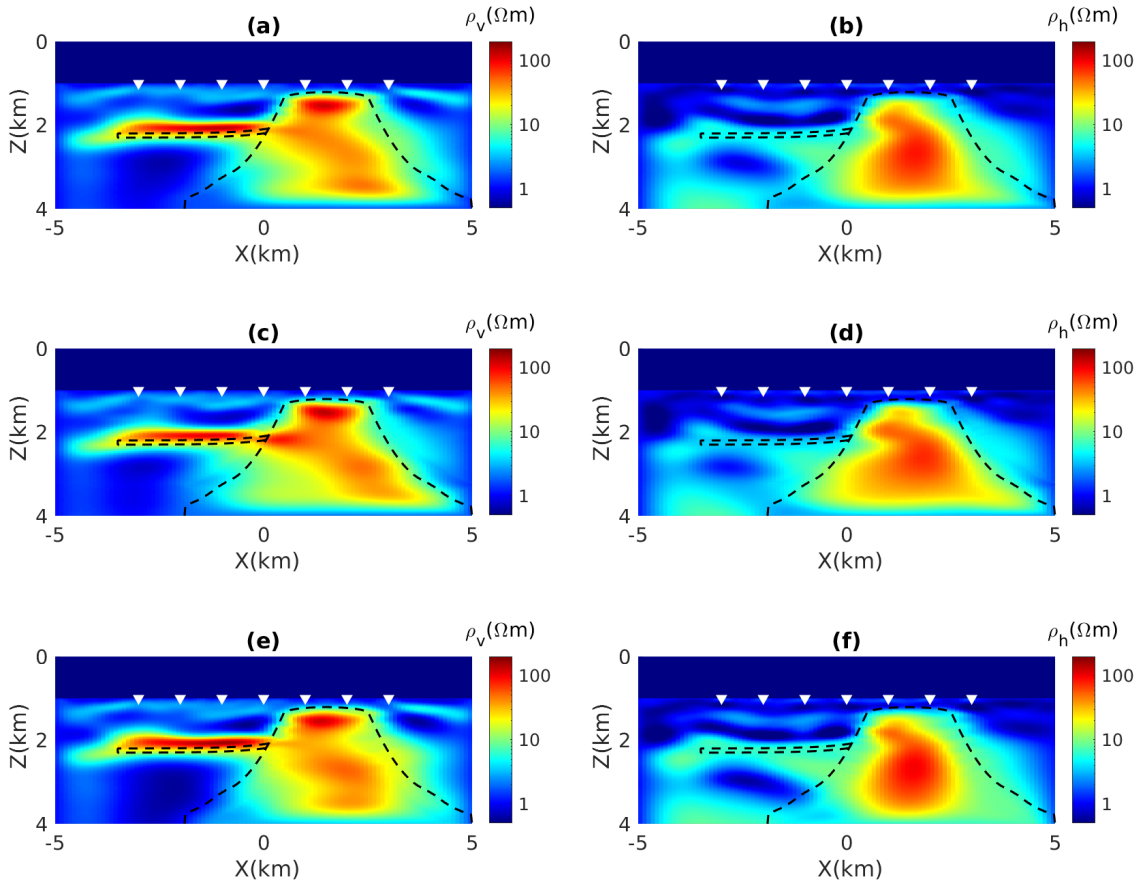

Fig. 3.6 Inverted resistivity models obtained by providing predefined initial models and also applying structural salt dome and reservoir constraints; (a) ρ_v (accurate); (b) ρ_h (accurate); (c) ρ_v (inaccurate: broadened+500m, shifted up 50m); (d) ρ_h (inaccurate: broadened+500m, shifted up 50m); (e) ρ_v (inaccurate: shrunkned+500m, shifted down 50m); (f) ρ_h(inaccurate: shrunkned+500m,shifted down 50m).

interface of anomaly, which will conform with the cross-gradient constraint. However, this development is out of the scope of the present analysis and will be explored in future studies.

3.4.4 Similarity prejudice between the vertical and horizontal resistivity models

The comparison of inverted vertical and horizontal resistivity models indicates that the shallower part of the salt dome is mapped relatively well in the vertical resistivity model, and the deeper part is better imaged in the horizontal resistivity model. Therefore, it is instructive to study whether enforcing a similarity prejudice between them can improve

both the vertical and horizontal resistivity models. It is expected that anomalies' interface of both vertical and horizontal resistivity coincide. This will also improve the horizontal resistivity image of the reservoir, which is faintly mapped in the horizontal resistivity model. One of the ways is to minimise the difference between the horizontal and vertical resistivity model, which is a case of a nonzero value of parameter β. We tested this technique with different β values, such as 0.1 and 1. For the inversion, we used an initial model comprising a half-space with a resistivity of 1.5 Ω-m for both horizontal and vertical components. The inversion results for β =0.1 are presented in Figure (3.7). The inversion did not converge below 3.88 % nRMS; because, for an anisotropic model, the difference can not be zero. Furthermore, the obtained model indicates that attempting to align vertical and horizontal resistivity introduces artifacts in the inverted model. These artifacts arise because the regularization term associated with the β factor tries to make the subsurface closer to an isotropic character. A viable strategy to mitigate these artifacts is to accurately characterise the anisotropy of the medium, which requires the anisotropy to be known prior, which is difficult to obtain. Nevertheless, we see the evident advantage of this strategy in terms of salt body imaging. Therefore, the imaging of the salt dome can be improved significantly by enforcing similarity between vertical and horizontal resistivity. It needs to be added that the salt is an isotropic body (see Figure 2.1) in the present case. However, if the salt dome is taken anisotropic, it would not change the conclusion that by incorporating detailed anisotropic information into the model, one can achieve a more realistic representation of the subsurface properties.

To prove the above stated assertion, we experimented using the isotropic model. The model comprises the same feature as in Figure (2.1) but with isotropic properties in both vertical and horizontal resistivity models. Utilising this model, we performed anisotropic inversion to evaluate the impact on imaging results. The inverted models without any similarity bias (β=0) after the nRMS reaches 3 % are shown in Figure (3.8), which is analogous to the anisotropic subsurface in terms of depth of imaging, data sensitivity, etc. Subsequently, we sought to achieve a similarity between horizontal and vertical resistivity employing β=0.1, and the resulting inverted models are presented in Figure (3.9). The inversion outcome is devoid of any significant artefacts compared to the anisotropic synthetic data scenario. The benefit of biasing the vertical and horizontal models to be similar clearly demonstrates the advantage of salt dome imaging. This finding underscores the CSEM method's inability to sense both vertical and horizontal resistivity equally well through the subsurface that is being imaged. It also highlights the importance of prior information about anisotropy, which can play a valuable role in CSEM imaging for geological complex subsurfaces.

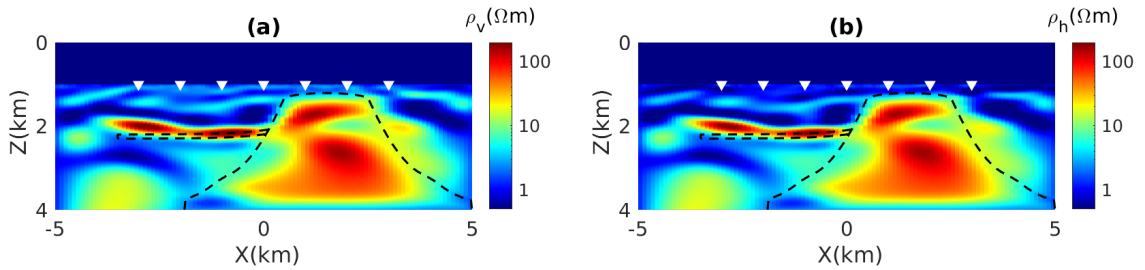

Fig. 3.7 Inverted resistivity models obtained by imposing similarity between vertical and horizontal resistivity in an anisotropic inversion; (a) vertical resistivity (ρ_v); (b) horizontal resistivity(ρ_h).

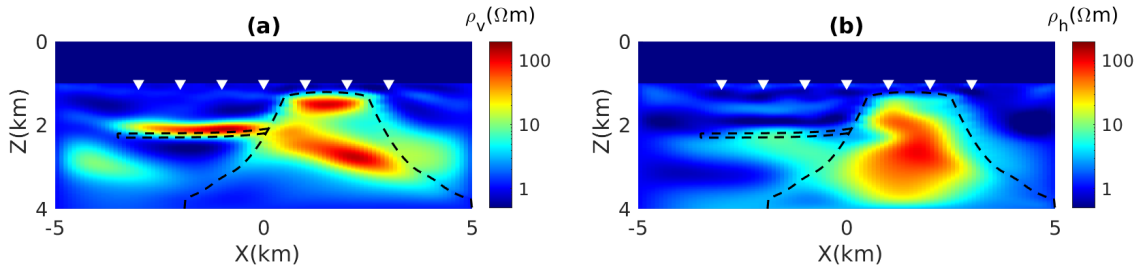

Fig. 3.8 Inverted resistivity models of a isotropic model obtained by an anisotropic inversion; (a) vertical resistivity (ρ_v); (b) horizontal resistivity(ρ_h).

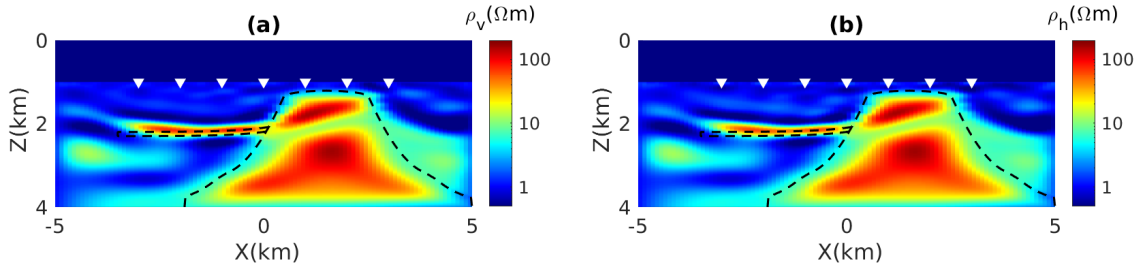

Fig. 3.9 Inverted resistivity models obtained by imposing similarity between vertical and horizontal resistivity in an isotropic model; (a) vertical resistivity (ρ_v); (b) horizontal resistivity(ρ_h).

3.5 Conclusion

We developed a 2D structurally constrained CSEM inversion algorithm using the cross-gradient method. The inversion analysis obtained by numerical experiments provides valuable information for applying such constraints on the inverted models. Structural constraints improve the imaging of complex geological features such as salt domes. However, the smoothing constraint conflict with the structural constraint prevents the sharp anomaly interface being produced in an inverted model. Using an initial model based on the prior information can improve the inversion outcome. However, it is crucial to exercise caution when utilising predefined initial models if confidence in prior information is lacking. Additionally, the strategy of minimising the difference between horizontal and vertical resistivity could improve the imaging of geologically complex subsurface. However, prior information may be required about the anisotropy of artefacts-free inversion. Overall, these results underscore the importance of careful model selection and constraint application to optimise the accuracy and reliability of subsurface imaging.

Chapter 4

2D Anisotropic Acoustic wave modeling using support operator method

4.1 Abstract

We developed an algorithm to simulate two-dimensional frequency-domain acoustic-wave response in a transversely isotropic medium with a tilted symmetry axis. The algorithm employs a support-operator finite-difference method for modeling. This method constructs a nine-point stencil finite-difference scheme for second-order elliptic equations for generalized anisotropic physical properties. The medium's properties are described as P-wave velocity on the symmetric axis, density, Thomsen's anisotropic parameters (epsilon and delta), and the tilt angle. The benchmarking analysis of modeled amplitude is illustrated using an isotropic whole-space model. Several synthetic experiments are conducted to evaluate the accuracy of the scheme for anisotropic models. The results suggest that the developed algorithm simulates the P-wave solution and the fictitious S-wave mode, as reported in the literature. Simulation for a heterogenous model with a spatially varying tilt angle of the medium symmetry axis is performed to ascertain the algorithm's robustness. The outcomes of the numerical experiments demonstrate that the developed algorithm can accurately simulate the frequency-domain response of acoustic waves in the tilted anisotropic media.

4.2 Introduction

In exploration seismology, anisotropy refers to the directional dependency of seismic wave propagation in subsurface material. Understanding anisotropy is vital in the seismic

methods for accurate velocity model building Li et al. (2008), amplitude interpretation, and reservoir characterization Besheli et al. (2005). Anisotropy can occur in various forms, but the two most common types encountered in exploration seismology are transverse isotropy and orthorhombic anisotropy. Transverse Isotropy (TI) is a frequently observed anisotropic nature of subsurface formations. The primary physical factors contributing to this TI symmetry, also known as hexagonal symmetry, are the inherent anisotropic properties of sedimentary formations, particularly shales, and the presence of regular fine and coarse layering. When sediments are horizontally layered, they exhibit TI characteristics with a vertical symmetry axis, commonly referred to as vertical transverse isotropy (VTI) Ikelle and Amundsen (2018). However, the tilted symmetry axis can arise due to the slope and folding of strata; in such cases, the anisotropy can be represented by a tilted transverse isotropic (TTI) media.

To model the propagation of seismic waves in anisotropic media, researchers commonly employ numerical methods such as finite difference Igel et al. (1995) and pseudospectral methods Carcione et al. (1988). Accurate modeling of seismic wave propagation in an anisotropic subsurface requires working with an elastic wave equation. However, it requires tremendous computational resources, and often, an acoustic wave approximation is adopted in the field of reflection seismology, particularly in the marine environment. For simulation of P-waves propagation using an acoustic wave approximation in vertical transversely isotropic (VTI) and orthorhombic anisotropic media, an approach proposed by Alkhalifah (1998, 2003) can be employed. His technique simplifies computational requirements by setting the vertical S-wave velocity to zero in the dispersion relation. Alkhalifah (1998) demonstrated that this strategy yields a kinematically accurate approximation of P-wave propagation.

The modeling of wave propagation can be implemented either in the time domain Gao et al. (2018); Mehra et al. (2012) or frequency domain Hustedt et al. (2004); Plessix (2007); Williamson and Pratt (1995). In general, time domain modeling is favored for 3D modeling; however, for 2D modeling, the frequency domain method provides an efficient option. Frequency-domain modeling is better suited for frequency-dependent behavior and long-distance wave propagation and allows greater control over sources in acoustic wave modeling Plessix (2007). In the past few years, researchers have made significant advancements in the development of anisotropic acoustic wave algorithms for VTI and TTI media. Zhou et al. (2006) introduced an algorithm for VTI media, while Operto et al. (2009) focused on frequency-domain modeling of visco-acoustic wave propagation through a TTI media.

In this study, we present the development of 2D acoustic wave modeling in an anisotropic medium using a support operator method. Support-operator method was first used by Ely et al. (2008) for seismic modeling. First, the discussion on governing equations for acoustic wave modeling in an anisotropic medium is presented, and next, mathematical concepts of the support operator method are discussed. Subsequently, the accuracy and versatility of the developed algorithm are illustrated using several numerical experiments.

4.3 The tilted transverse isotropic acoustic wave modeling

For tilted transverse isotropic (TTI) media, a modified 2D acoustic wave equation was proposed by Zhou et al. (2006); and Operto et al. (2009) revised it for variable density medium. Accordingly, for a spatially varying angle of the tilted-symmetric axis and density, a 2D acoustic wave equation in the time domain can be expressed as,

$$\begin{aligned} &\frac{1}{\kappa}\frac{\partial^2 p}{\partial t^2} - (1+2\delta)Hp - H_0 p = (1+2\delta)Hq \\ &\frac{1}{\kappa}\frac{\partial^2 q}{\partial t^2} - 2(\epsilon-\delta)Hq = 2(\epsilon-\delta)Hp, \end{aligned} \tag{4.1}$$

here H and H_0 are defined as,

$$\begin{aligned} H &= \frac{\partial}{\partial x}\cos^2\theta_0 b\frac{\partial}{\partial x} + \frac{\partial}{\partial z}\sin^2\theta_0 b\frac{\partial}{\partial z} - \left(\frac{\partial}{\partial x}\frac{\sin 2\theta_0}{2}b\frac{\partial}{\partial z} + \frac{\partial}{\partial z}\frac{\sin 2\theta_0}{2}b\frac{\partial}{\partial x}\right) \\ H_0 &= \frac{\partial}{\partial x}\sin^2\theta_0 b\frac{\partial}{\partial x} + \frac{\partial}{\partial z}\cos^2\theta_0 b\frac{\partial}{\partial z} + \left(\frac{\partial}{\partial x}\frac{\sin 2\theta_0}{2}b\frac{\partial}{\partial z} + \frac{\partial}{\partial z}\frac{\sin 2\theta_0}{2}b\frac{\partial}{\partial x}\right), \end{aligned} \tag{4.2}$$

where κ is the bulk modulus; b is the inverse of mass density, termed buoyancy; the δ and ϵ are dimensionless parameters defining the anisotropy Thomsen (1986), and θ_0 is the angle of tilled symmetry axis to the vertical direction; p is the pressure wavefield, and q is the auxiliary pressure wavefield introduced by Zhou et al. (2006) to recast the fourth-order equation proposed by Alkhalifah (1998) into a coupled second-order equations which are much easier to solve. Furthermore, the $\epsilon - \delta$ must be greater than or equal to zero so that equation (4.1) can be a well posed initial value problem. H and $H0$ are differential operator and the cross derivative term in these both differential operator are responsible for angular rotation of the symmetry axis in TTI medium. Isotropic acoustic wave equation is a special case of equations (4.1) and (4.2) under the conditions, $\epsilon = \delta = 0$, whereas $\epsilon \neq \delta$

means that ellipticity does not vanish. The solution of the above equations provides the response in the time domain. Equation (4.1) can be transformed into frequency domain using the Fourier transform and in the frequency domain can be written as,

$$\begin{aligned} \frac{\omega^2}{\kappa} p - (1+2\delta) Hp - H_0 p &= (1+2\delta) Hq \\ \frac{\omega^2}{\kappa} q - 2(\epsilon-\delta) Hq &= 2(\epsilon-\delta) Hp, \end{aligned} \tag{4.3}$$

where ω is the angular frequency. The same notations are used for the time and frequency domain responses for brevity. Equation (4.2) can be represented in a concise form using a set of elliptic partial differently equations as,

$$\begin{aligned} H &= \nabla \cdot \Theta \nabla \\ H_0 &= \nabla \cdot \Theta_0 \nabla, \end{aligned} \tag{4.4}$$

where Θ and Θ_0 are given as,

$$\Theta = \begin{pmatrix} \cos^2\theta_0 b & -\frac{\sin 2\theta_0}{2} b \\ -\frac{\sin 2\theta_0}{2} b & \sin^2\theta_0 b \end{pmatrix} \quad \& \quad \Theta_0 = \begin{pmatrix} \sin^2\theta_0 b & \frac{\sin 2\theta_0}{2} b \\ \frac{\sin 2\theta_0}{2} b & \cos^2\theta_0 b \end{pmatrix}. \tag{4.5}$$

Using equations (4.3) and (4.4), we can recast the problem of acoustic wave modeling for a TTI media as a matrix equation given as,

$$\begin{pmatrix} \frac{\omega^2}{\kappa} - (1+2\delta) H - H_0 & -(1+2\delta) H \\ -2(\epsilon-\delta) H & \frac{\omega^2}{\kappa} - 2(\epsilon-\delta) H \end{pmatrix} \begin{pmatrix} p \\ q \end{pmatrix} = \begin{pmatrix} 0 \\ 0 \end{pmatrix} \tag{4.6}$$

The above equation is written for source free media and in case of a source, the right hand side vector will contain the source information. In this study, we propose to solve the equation (4.6) using the support operator method originally introduced by Shashkov (2018).

4.3.1 Discretization

The matrix equation (4.6) can be assembled by four block matrices where each block matrix depends on the discrete approximation of the continuum operators given in equation (4.4). We discretize these continuum operators using the support operator method Samarskii et al. (1981). The details of the support operator method can be found in Shashkov (2018); however, for completeness, a basic concept of the method is presented

in this study. The support operator method instructs first devising the prime operator, and subsequently, the derived operator is designed by enforcing the relationship between prime and derived operators. The basic concept of the support operator method for designing a conservative differences scheme can be explained using the following five steps Shashkov (2018). First, write the governing equation using first-order differential operators such as gradient, divergence, and curl. Therefore, we have rewritten the present problem employing the gradient and divergence operators (see equations 4.4 to 4.6). The second step is to use an identity through which the operators involved in the governing equation are connected. The identity employed in the present scheme is given as,

$$\int_v \phi \nabla \cdot \vec{\mathbf{F}} dv + \int_v (\vec{\mathbf{F}}, \nabla \phi) dv = \oint_s \phi(\vec{\mathbf{F}}, \vec{\mathbf{n}}) ds, \tag{4.7}$$

where ϕ and $\vec{\mathbf{F}}$ are scalar and vector functions, respectively; $\vec{\mathbf{n}}$ denotes outer unit-normal vector; v represents an arbitrary volume enclosed by the surface, s. The third step is to discretize the scalar, vector, and tensor functions. We implement a nodal discretization of scalar functions and cell-centered discretization of vector and tensor functions. The next step is to construct a prime operator, and in the case of nodal discretization of scalar functions, the natural choice is the gradient operator as the prime operator. Therefore, the divergence operator is assigned the role of a derived operator. The last step is to construct the derived operator enforcing the identity given in equation (4.7). Shashkov (2018) showed that imposition of identity given in the above equation leads to the relation between gradient and divergence operators as,

$$DIV = -GRAD^*, \tag{4.8}$$

where * represents adjoint operator; $GRAD$ and DIV, denote the gradient and divergence operators, respectively. Thus, the discrete analog of the general elliptic operator is self-adjoint and positive. These properties of the discrete problem make it possible to use effective iterative methods for solving the system of finite difference equations. Since the operators constructed through this procedure mimic the properties of the original continuum operator of the identity, the support operator method is also known as the mimetic finite different method (MFDM). A nine-point stencil discretization, as shown in figure (4.1), is considered to describe the salient features of the support operator method. The grid follows a left-handed coordinate system with the z-axis pointed downward (i.e., depth).

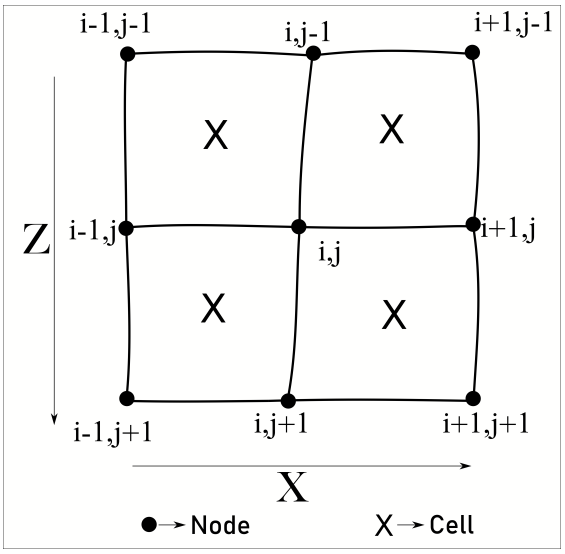

Fig. 4.1 Schematic representation of the nine-point stencil scheme employed for model discretization.

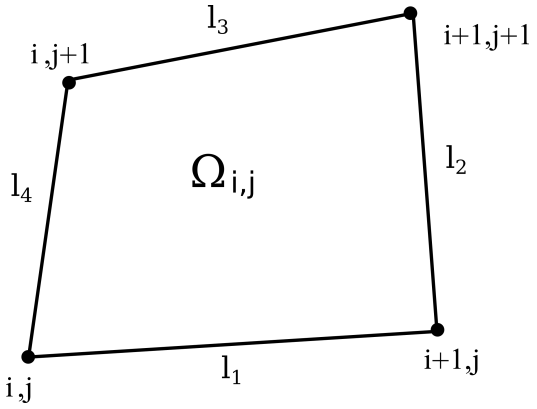

Fig. 4.2 Schematic diagram for a cell i, j having area Ω and four sides as, l_1, l_2, l_3 and l_4.

4.3.2 Construction of $\nabla \cdot \Theta \nabla$ operator

The components of the gradient operator can be derived utilizing Green's formula as,

$$\frac{\partial P}{\partial x} = \lim_{A \to 0} \frac{\oint_C P \, dz}{A} \tag{4.9}$$

and

$$\frac{\partial P}{\partial z} = -\lim_{A \to 0} \frac{\oint_C P \, dx}{A}, \tag{4.10}$$

where A is an arbitrary area surrounded by a boundary denoted by C. For discrete cases, the area, A, of the i, j cell is represented by Ω_{ij} as illustrated in figure (4.2) . l_1, l_2, l_3 and l_4 are

the four sides of quadrilateral as shown in figure (4.2). For an approximation of the right-hand side of equation (4.9) and (4.10), the contour integral is divided into four integrals each over the corresponding side of the quadrangle of area Ω_{ij}. Because each side of the quadrangle is a segment of the line, the integral over each side is one-dimensional, and to approximate it, the trapezium rule is used. After applying the trapezium rule, the discrete analogous of equations (4.9) and (4.10) can be written as,

$$(D_x P)_{ij} = \frac{(P_{i+1,j+1} - P_{i,j})(z_{i,j+1} - z_{i+1,j}) - (P_{i,j+1} - P_{i+1,j})(z_{i+1,j+1} - z_{i,j})}{2\Omega_{ij}}, \tag{4.11}$$

and

$$(D_z P)_{ij} = \frac{(P_{i+1,j+1} - P_{i,j})(x_{i,j+1} - x_{i+1,j}) - (P_{i,j+1} - P_{i+1,j})(x_{i+1,j+1} - x_{i,j})}{2\Omega_{ij}}, \tag{4.12}$$

respectively, where, $x_{i,j}$ and $z_{i,j}$ denote the coordinate of i, j node. Using the equations (4.11) and (4.12), an expression of prime operator, gradient, for discrete case can be written as,

$$GRAD(P) = \begin{bmatrix} D_x P \\ D_z P \end{bmatrix}. \tag{4.13}$$

The gradient operator maps the scalar field to a vector field. The next step is to operate the tensor on the vector field, which results in another vector field (say **W**) as,

$$\mathbf{W} = \begin{bmatrix} W^x \\ W^z \end{bmatrix} = \Theta\ GRAD(P) = \begin{bmatrix} \Theta_{xx} & \Theta_{xz} \\ \Theta_{xz} & \Theta_{zz} \end{bmatrix} \begin{bmatrix} D_x P \\ D_z P \end{bmatrix}. \tag{4.14}$$

where Θ is a tensor, referred as buoyancy tensor, hereafter in this study. Now, the next task is to construct the derived operator (divergence) using the gradient operator given in equation (4.13) by enforcing the property given in equation (4.8). Consequently, the expression for divergence operator can be written as,

$$
\begin{aligned}
(DIV\vec{\mathbf{W}}) = \frac{0.5}{VN_{ij}}(-((z_{i-1,j}-z_{i,j-1})W^x_{i-1,j-1}-(z_{i,j+1}-z_{i+1,j})W^x_{ij}+ \\
(z_{i+1,j}-z_{i,j-1})W^x_{i,j-1}-(z_{i,j+1}-z_{i-1,j})W^x_{i-1,j})+ \\
((x_{i-1,j}-x_{i,j-1})W^z_{i-1,j-1}-(x_{i,j+1}-x_{i+1,j})W^z_{ij}+ \\
(x_{i+1,j}-xi,j-1)W^z_{i,j-1}-(x_{i,j+1}-x_{i-1,j})W^z_{i-1,j})),
\end{aligned}
\tag{4.15}
$$

where VN_{ij} is the average area for four cells sharing node $i,\ j$ as their corner. By assembling the terms for a nine-point stencil depicted in figure (2.1), an equation for a central node, $i,\ j$, can be written as Shashkov (2018),

$$
\begin{aligned}
(\nabla\cdot\Theta\nabla P)_{ij} = C_{i,j}P_{i,j}+C_{i+1,j}P_{i+1,j}+C_{i-1,j}P_{i-1,j}+C_{i,j-1}P_{i,j-1}+C_{i,j+1}P_{i,j+1} \\
+C_{i-1,j-1}P_{i-1,j-1}+C_{i-1,j+1}P_{i-1,j+1}+C_{i-1,j+1}P_{i-1,j+1}+C_{i+1,j+1}P_{i+1,j+1},
\end{aligned}
\tag{4.16}
$$

where $C_{i,j}, C_{i+1,j}, C_{i-1,j}, C_{i,j-1}, C_{i,j+1}, C_{i-1,j-1}, C_{i-1,j+1}, C_{i+1,j-1}, C_{i+1,j+1}$ are the coefficients and the expression for these coefficients are given in the Appendix B.1.

The linear equations for all the nodes are assembled to form a discrete representation of elliptic equations to construct operators, H and H_0. Subsequently, a linear system of equations is obtained by assembling these block matrices to form the matrix equation (4.4) and solved for a monochromatic source under the appropriate boundary conditions. The homogeneous boundary conditions are applied to simulate the wavefield in an unbounded domain. It requires the field to vanish at the domain boundary, which is achieved by applying the PML technique. The support operator method works with discontinuous physical parameters. Gyrya and Lipnikov (2012) discuss a detailed analysis of the stability of the mimetic finite difference method, which applies to the present study. We have employed a direct solver for computing the inverse of the system matrix. The proposed algorithm has been implemented in the Python programming language. Next, we present numerical experiments to test the accuracy of the developed code.

4.4 Numerical Results

This section presents the results from numerical simulations for isotropic, vertical transverse isotropic (VTI), and tilted transverse isotropic (TTI) whole-space models and a heterogenous model having a spatially varying tilt angle of the medium symmetry axis.

The simulation results are compared with analytical results wherever available. For whole-space models, the modeling domain extends at 3250 m × 3250 m and the transmitter is placed at the center of the model.

4.4.1 Isotropic Case

The primary goal of the isotropic modeling experiment is to analyze the accuracy of amplitudes computed using the developed algorithm, as the analytical results Aki and Richards (2002) are available for the isotropic case. A whole space of 4000 m/s P-wave velocity is considered for the isotropic case. The real and imaginary parts of the simulated response using the developed algorithm at 10 Hz frequency are shown in figure (4.3). For the benchmarking, a relative misfit defined as $|\frac{|G^a_{(i,j)}|-|G^{SO}_{(i,j)}|}{|G^a_{(i,j)}|}|$ is calculated; where, G^a and G^{SO} denote the analytical and numerical responses, respectively, at (i, j) node and $||$ represents the absolute value. The misfit plot for the 10 Hz simulation is shown in figure (4.4), where the maximum misfit value is around 0.06. The misfit is relatively small in the diagonal directions compared to the axis directions. Gyrya and Lipnikov (2012) showed that the numerical dispersion in the support operator method is relatively less in the diagonal direction, therefore, the we observe better fit in diagonal direction. Additionally, the real and imaginary parts of the simulated and analytical response along a horizontal profile passing through the source position are illustrated in figure (4.5). The plots include the absorbing boundary region to exhibit the effectiveness of boundary conditions application on the simulated response. These comparison analyses illustrate the accuracy of amplitude computed using the proposed algorithm.

Furthermore, time domain responses are calculated using inverse Fourier transform for a 10 Hz dominant frequency Ricker wavelet Ricker (1940) as the source. The Ricker wavelet that is utilized as a source and its amplitude spectrum is illustrated in figure (4.6). The wavefronts at three-time samples viz. $t = 0.1s$, $t = 0.2s$, and $t = 0.3s$, are displayed in figure (4.7). As expected, the frequency and time domain wavefield exhibit a perfectly circular shape. The circular behavior arises due to the isotropic nature of the medium, as the velocity is the same in all directions. These results indicate that the developed algorithm can simulate accurate acoustic wave propagation in isotropic media. Next, we consider a VTI half-space model.

4.4.2 Vertical Transverse Isotropic case

For the VTI experiment, we considered two cases: weak anisotropy and strong anisotropy. The parameters for both models are listed in Table (4.1). For the first case, the horizontal-

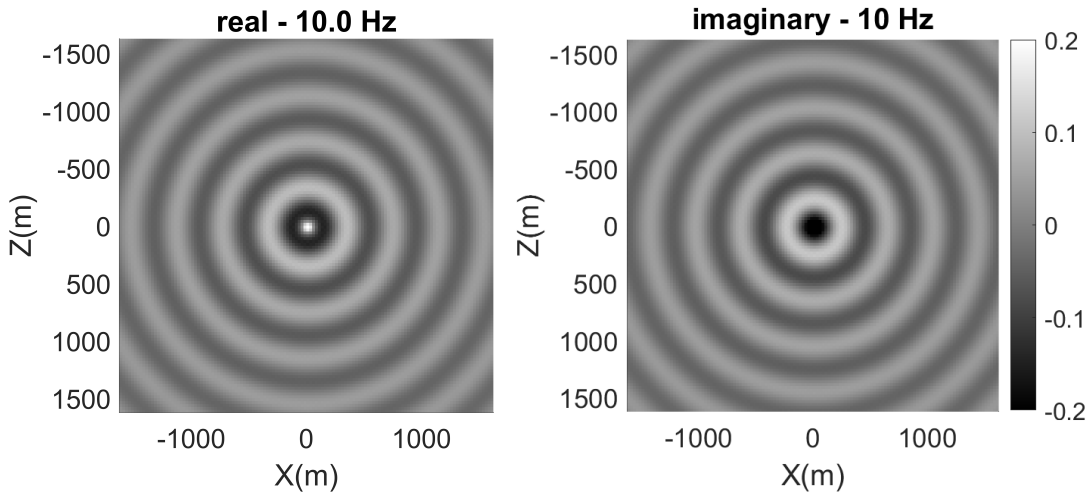

Fig. 4.3 Real and imaginary parts of pressure wavefield in the frequency domain simulated using the support opertaor method for a homogeneous isotropic medium employing a monochromatic source emitting 10 Hz frequency. The same color scale is used for both images; hence, it is only displayed in one of the images for brevity.

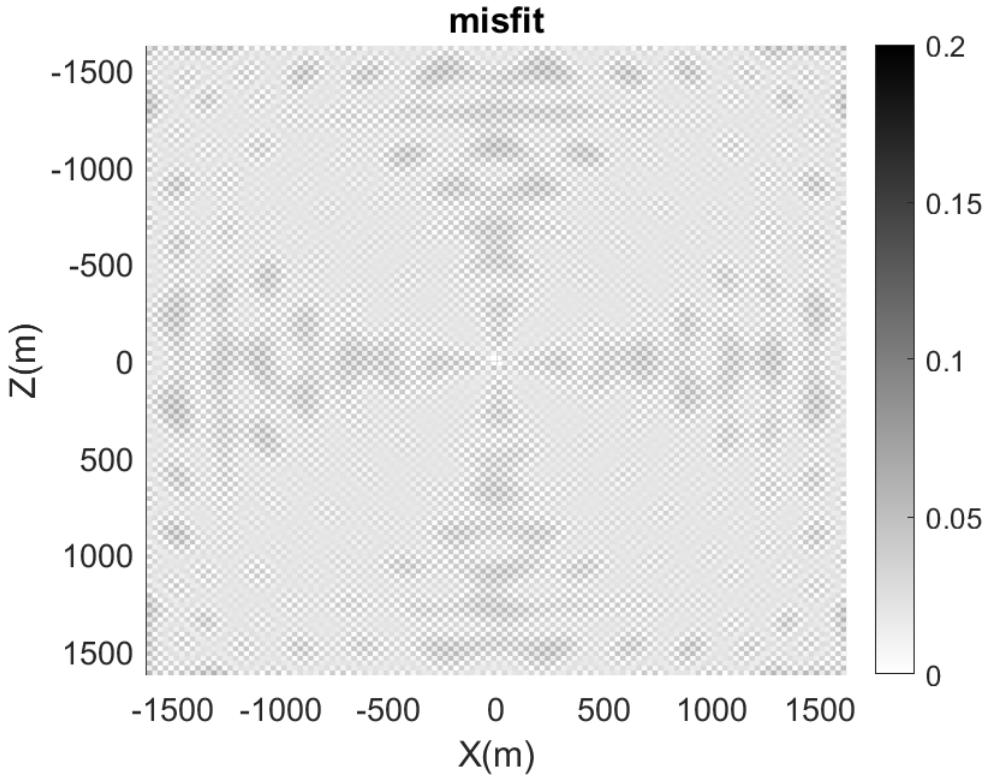

Fig. 4.4 Relative misfit of amplitude between the analytical and numerical simulation performed using the support-operator method at 10 Hz.

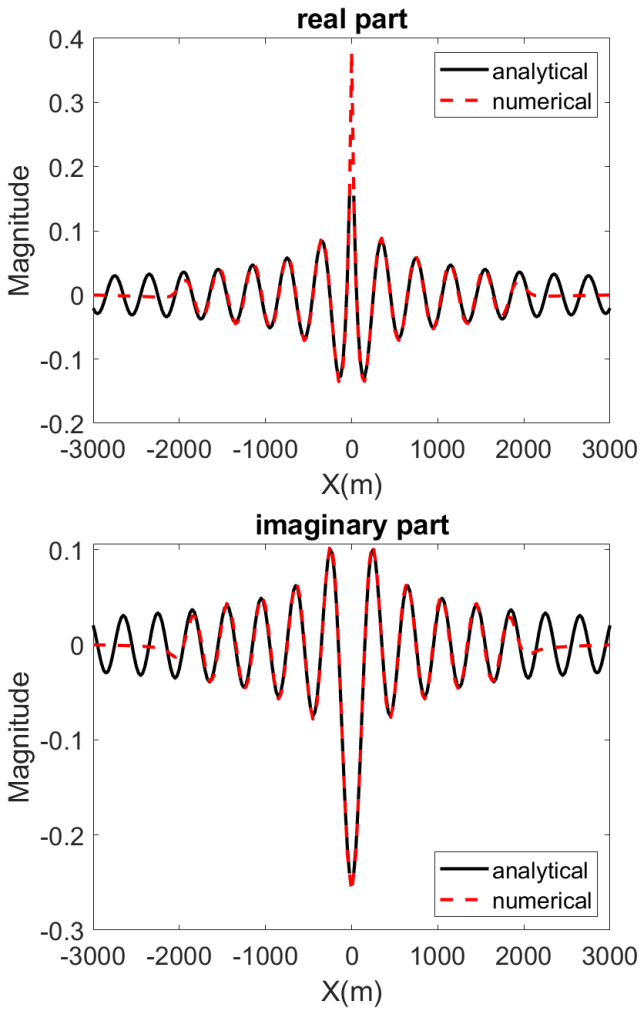

Fig. 4.5 Real and imaginary parts of responses calculated using the proposed numerical method, including the PML region and the analytical responses at a horizontal line passing through the source position for a 10 Hz frequency source.

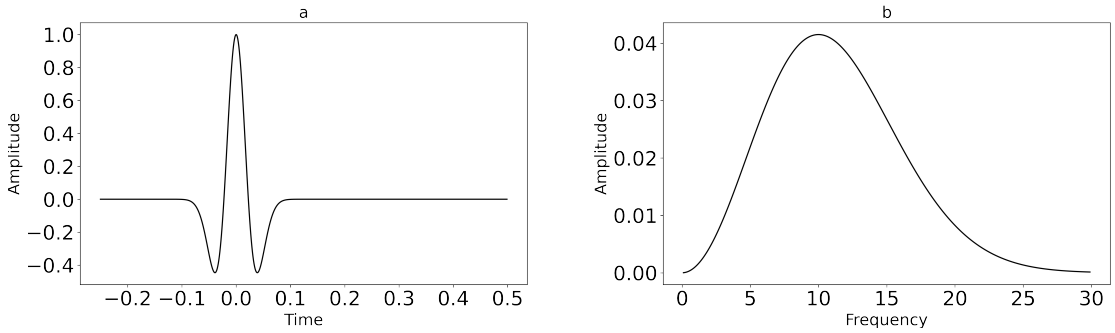

Fig. 4.6 Ricker Wavelet of 10 Hz dominant frequency; (a) time domain and (b) amplitude spectrum in the frequency domain

to-vertical velocity ratio is 1.1, as the horizontal velocity is $1+\epsilon$ times the vertical velocity Thomsen (2014) because we measure the angle, θ_0, from the vertical direction. Figure (4.8) shows the frequency-domain response of the pressure wavefield's real component at 10 and 18 Hz. Further, the time domain response utilizing a Ricker wavelet of 10 Hz dominant frequency is calculated employing inverse Fourier transform. Figure (4.9) shows the wavefronts at three specific time instances ($t = 0.1s, 0.2s, 0.3s$). Since the horizontal velocity is faster than the vertical velocity in this VTI model, the simulated response exhibits an elliptical nature with the major axis in the horizontal direction. The time domain results also comprise another wavefield propagating slower than the main P-wavefront. It is a fictitious S-wave that arises in the case of anisotropic acoustic wave modeling and is referred to as S-wave artifacts in literature Alkhalifah (1998). Several schemes have been proposed Abedi and Stovas (2020); Li and Stovas (2021); Stovas et al. (2021); Xu et al. (2020) to suppress these artifacts in the acoustic wave modeling of anisotropic models. The S-wave artifact is diamond-shaped for this model because the anisotropic parameter ϵ is greater than δ, and this behavior follows the results reported in other studies Zhou et al. (2006). To assess the VTI simulation's accuracy, the time domain responses are benchmarked using the analytical wavefront calculated using the Payton (1983) formulation, developed explicitly for Class IV TI (transversely isotropic) media. The red and blue curves overlayed on the time-domain response in figure (4.9) represent the analytical P and S wavefronts, respectively. We can observe an excellent kinematic agreement between the acoustic snapshot and the analytic P-wavefront, indicating that the acoustic approximation of wave propagation in VTI model provides an accurate simulation. Thus, the developed algorithm exhibits the capabilities of modeling accurate results for the acoustic approximation of wave propagation in VTI media, at least for a weak anisotropy case. Next, we analyze the algorithm's robustness for a strong anisotropy VTI model.

Medium	Velocity (V_p in ms^{-1})	Density (ρ in kgm^{-3})	Epsilon (ϵ)	Delta (δ)	Phi (ϕ in °)
Sediments	4000	2500	0.1	0.02	0
zinc medium	2955.06	7100	0.830645	2.7098	0
TTI	4000	2500	0.1	0.02	45

Table 4.1 Table presents the values of physical parameters utilized for different numerical tests for anisotropic experiments. The P-wave velocity along the vertical direction through the medium is represented by V_p. The dimensionless parameters, epsilon (ϵ) and delta (δ), introduce anisotropy to the media. The angle between the vertical axis and the axis of anisotropy is denoted as phi (ϕ).

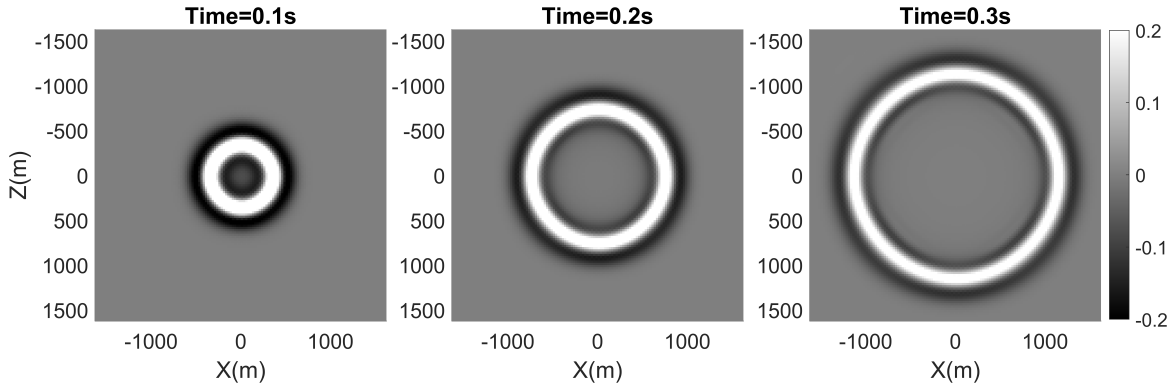

Fig. 4.7 Pressure wavefield in the time domain for a homogeneous isotropic medium employing a 10 Hz dominant frequency Ricker wavelet as a source; the corresponding time is mentioned at the top of each image.

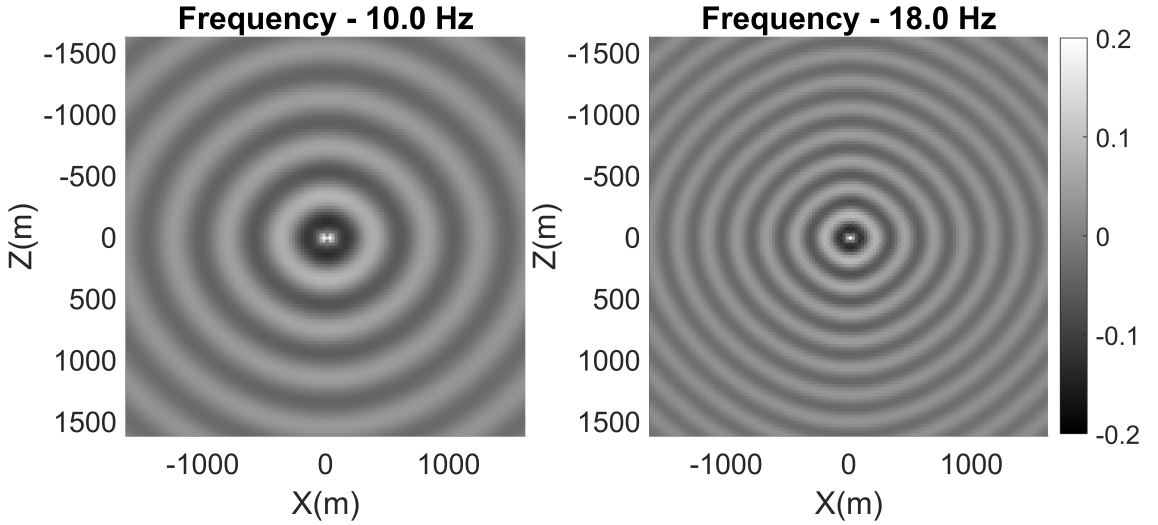

Fig. 4.8 Real part of pressure wavefield in the frequency domain for a homogeneous VTI medium for 10 and 18 Hz frequencies.

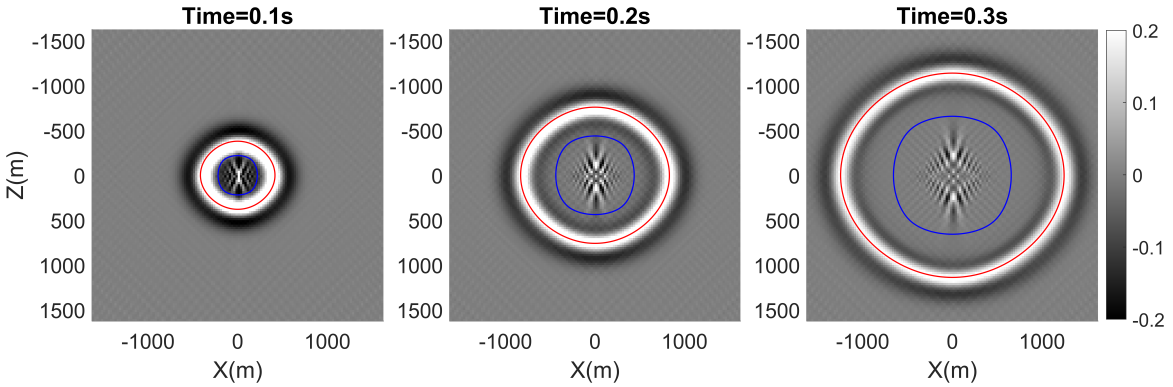

Fig. 4.9 Pressure wavefield in the time domain for a homogeneous VTI medium at three-time instances using a 10 Hz dominant frequency Ricker wavelet as a source, where the red and blue curves show the P and S wavefronts calculated using the analytical formula.

The zinc crystal is often used to test the modeling algorithm for strong anisotropy media. The Thomsen parameters ϵ and δ for zinc crystal are 0.83 and 2.7, respectively, leading to a horizontal-to-vertical velocity ratio of 1.83., which is a strong anisotropic. Generally, this particular combination of parameters is expected to result in an unstable simulation of S-waves when using the VTI acoustic equation Operto et al. (2009). However, in our frequency domain solution, we did not observe the generation of S-waves even though the value of ϵ is smaller than δ, and the simulation of P-waves remained stable. Operto et al. (2009) provided a possible explanation for this unexpected behavior due to the presence of absorbing boundary conditions in the frequency domain problem. Implementing these absorbing boundary conditions cancels out the instability associated with the S-wave mode. Therefore, it also confirms our algorithm's optimal performance of boundary conditions. To assess the accuracy of modeled response, the analytical VTI wavefronts are computed and overlayed on the numerically calculated wavefront for the zinc crystal (Figure 4.10). The comparison shows an effective agreement in terms of kinematics behavior between wavefronts for P-wave propagation. This matching reinforces the reliability and precision of the numerical approach in modeling wave propagation even in VTI media with disparate values of ϵ and δ. Furthermore, these results are noteworthy as they demonstrate the stability of the frequency-domain simulations in the presence of anisotropy, even in cases where the parameter ϵ is considerably smaller than δ. These experiments indicate that the chosen method and its associated boundary conditions are robust and capable of accurately capturing the behavior of P-wave propagation in anisotropic media, even for strong anisotropic VTI media.

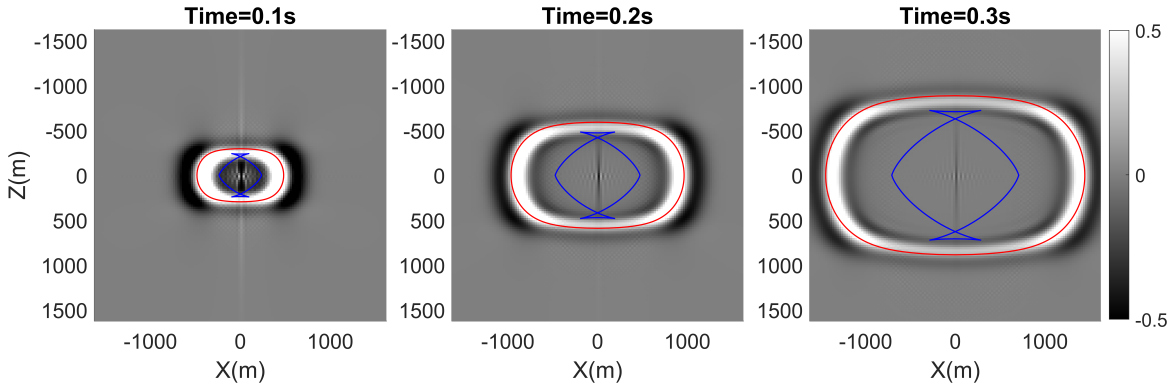

Fig. 4.10 Pressure wavefield in the time domain for a homogeneous Zinc VTI medium at three-time instances using a 10 Hz dominant frequency Ricker wavelet as a source, where the red and blue curves show the P and S wavefronts calculated using the analytical formula.

4.4.3 Tilted Transverse Isotropic case

In the last experiment for the whole-space examples, a TTI anisotropic model is considered, and the parameters for this model are given in Table (4.1) (see bottom-most row). Figures (4.11) and (4.12) illustrate the frequency and time domain pressure wavefield, respectively. The wavefields in both cases exhibit an elliptical shape, similar to the VTI results; however, the elliptical wavefront's major axis is tilted as the anisotropy axis is rotated at 45^o. This tilt in the simulated response matches the angle in the anisotropic. As expected, the S-wave artifacts caused by the anisotropy are also rotated by the same angle. The tilted axis of anisotropy introduces directional dependencies, leading to the tilted wavefronts observed in both the frequency and time domains. Therefore, we can use the analytical wavefront formulation developed for the VTI model and rotate it with the angle of anisotropy to benchmark TTI modeling. Consequently, the analytical wavefronts for both P- and S-wave are calculated and overlayed on the time domain response after rotating it with an anisotropy angle. Similar to the VTI case, the TTI modeling results also match the analytical result for P-wave propagation. The above-discussed experiments for isotropic, VTI, and TTI whole-space models demonstrate that the support operator method employed in our simulations delivers accurate simulation, providing a valuable tool for modeling anisotropic acoustic wave propagation. Next, a simulation in the case of a heterogeneous model is presented.

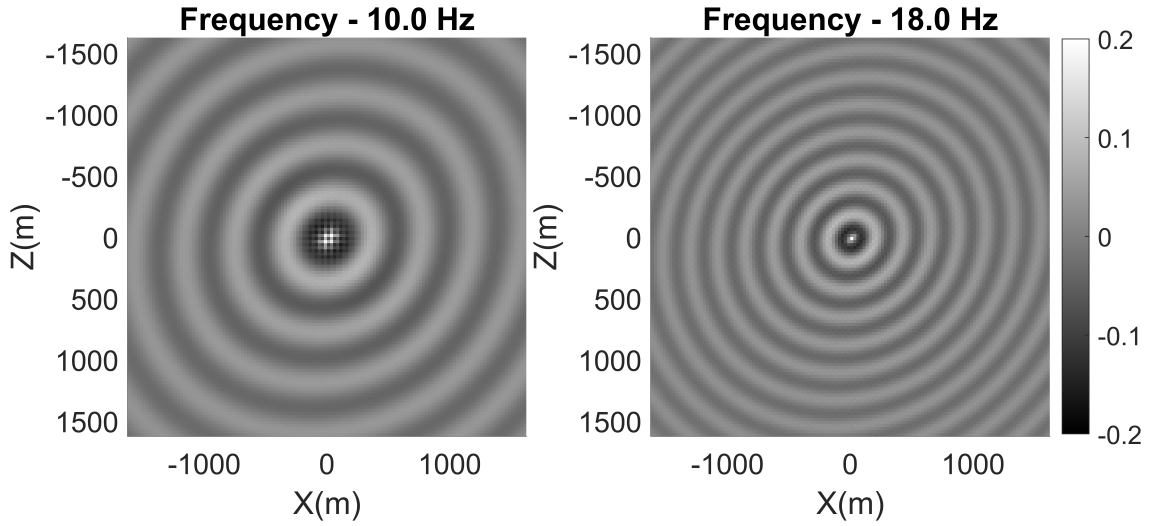

Fig. 4.11 Real part of pressure wavefield in the frequency domain for a homogeneous TTI medium for 10 and 18 Hz frequencies.

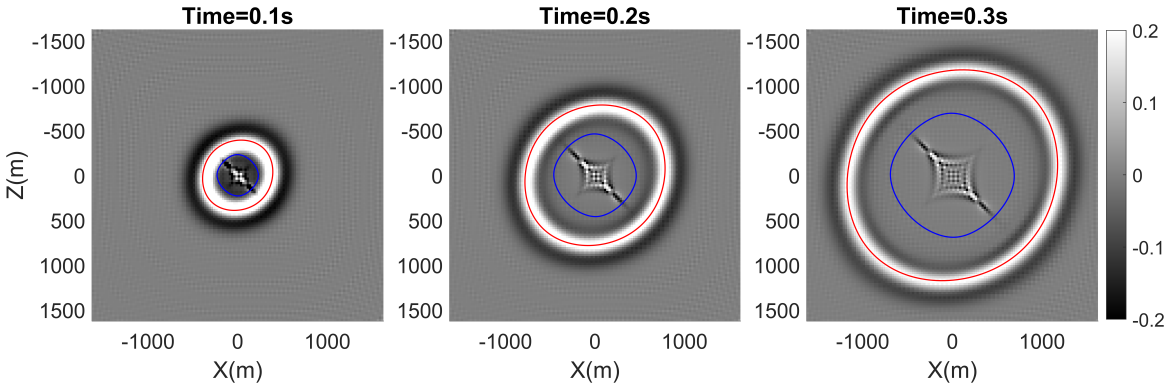

Fig. 4.12 Pressure wavefield in the time domain for a homogeneous TTI medium at three-time instances using a 10 Hz dominant frequency Ricker wavelet as a source, where the red and blue curves show the P and S wavefronts calculated using the analytical formula.

4.4.3.1 Heterogeneous medium

A model with five strata of distinct velocities is used for wave propagation simulations in a heterogeneous subsurface. The model has several folded layers forming anticlinal structures with a perfectly vertical axial plane meeting the x-axis at -500 m. The litho unit interfaces, densities, and velocities are shown in figure (4.13). The bulk modulus is calculated by multiplying the density of each unit and the square of velocity. Furthermore, two TTI cases with spatially varying tilt angles of the medium's symmetry axis are also considered for experiments. In the first case, the direction of the symmetry axis is taken as the tangential to the interface, while in the second case, the symmetry axis is assumed as normal to the interface. Subsequently, the tilt angle of the symmetry axis is estimated as the angle between the symmetry axis and the vertical direction. The calculated tilt angles and densities are used to obtain the elements of the buoyancy tensor (see equation (4.5)). Images of all three estimated tensor elements for the first TTI case are shown in figure (4.14). In the TTI simulations, the δ and ϵ are taken as 0.02 and 0.1, except in the first layer, since the first litho unit is assumed to be isotropic, so that the travel time and amplitude of the first reflection can be compared between the isotropic and anisotropic medium. The simulations are performed for a source placed at 0.0 and 50 m in the x and z-direction for all three (one isotropic and two TTI) models using a modeling domain of 10000 m and 3500 m in the horizontal and vertical directions, respectively. The grid spacing is taken as 25 m in both horizontal and vertical directions. Figure (4.15) presents the real components of simulated pressure wavefields at 10 Hz frequency for all three cases. Furthermore, the frequency domain responses are transformed into the time domain using the Fourier transform, considering a Ricker wavelet of 10 Hz dominant frequency. The snapshots of wavefield propagation at three-time instances at 0.2, 0.4, and 0.6 seconds are illustrated in figure (4.16). The reflected waves display their association with the interface drawn as cyan colored dashed lines over the images. Additionally, weak diffracted energy is also observable, traveling behind the reflected wavefront. These are generated due to the staircase approximation of dipping interfaces due to structured grid discretization used in the method, as visible in figure (4.14). Since the wave velocity along the symmetry axis will be the same as the isotropic velocities of respective strata, whereas the velocity perpendicular to the symmetry axis will be $1+\epsilon$ times the velocity along the symmetry axis, therefore, the velocity will be higher in the direction perpendicular to the interface as in the first case of TTI. In contrast, in the second case, it will be faster in the direction parallel to the interface. A careful comparison of three simulated wavefronts at a particular time does reveal such behavior. For example, the velocity in the z-direction of the subsurface just below the source position will be the same for the isotropic model

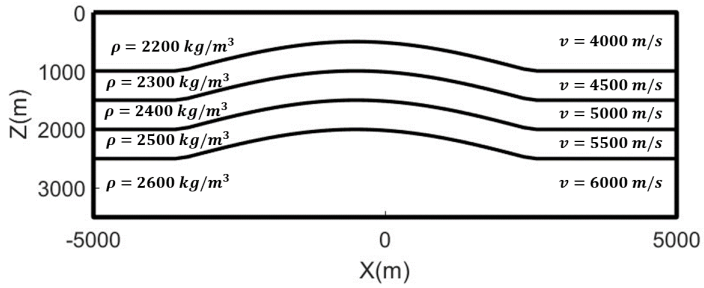

Fig. 4.13 Schematic diagram depicting interfaces of different strata of a 2D heterogeneous along with their densities and velocities.

and the second case of TTI; however, it will be faster for the first case of TTI. The same is observed by comparing the wavefronts in the z-direction at x=0 m, particularly visible at 0.6 s snapshots. In contrast, in the second TTI case, the wavefront expands faster in the horizontal direction than in other cases, as anticipated.

The shot-point gatherers for receivers located at 75 m inside the subsurface are depicted in figure (4.17). Since the first layer is isotropic in all three simulations, the travel time of the first reflection should be the same, and these do match each other in simulated gathers. Furthermore, the acoustic impedance contrast at the first interface for the isotropic and the second TTI model is approximately the same at the zero offset; however, it is higher for the first TTI case. The same is revealed by comparing the first reflected events of all three simulations as the first reflection amplitude at near zero offsets are similar for figures (4.17a) and (4.17c) while it is stronger in case of the figure (4.17b). Furthermore, the travel time of all the reflections for isotropic and the second case of TTI matched well at smaller offsets, while the travel time is smaller for the first case of TTI owing to faster velocity in the direction perpendicular to the interfaces, except in the first layer. The diffracted energy is also observable in shot point gathers. Thus, the simulated data exhibit the properties of seismic wave propagation and behavior as expected for such models, but there are no analytical results for these models to compare. Nonetheless, the numerical results collectively demonstrate the proposed algorithm's ability to model the response of an acoustic approximation in arbitrarily oriented anisotropic media. Therefore, the proposed algorithm can be used in seismic data analysis for anisotropic subsurface.

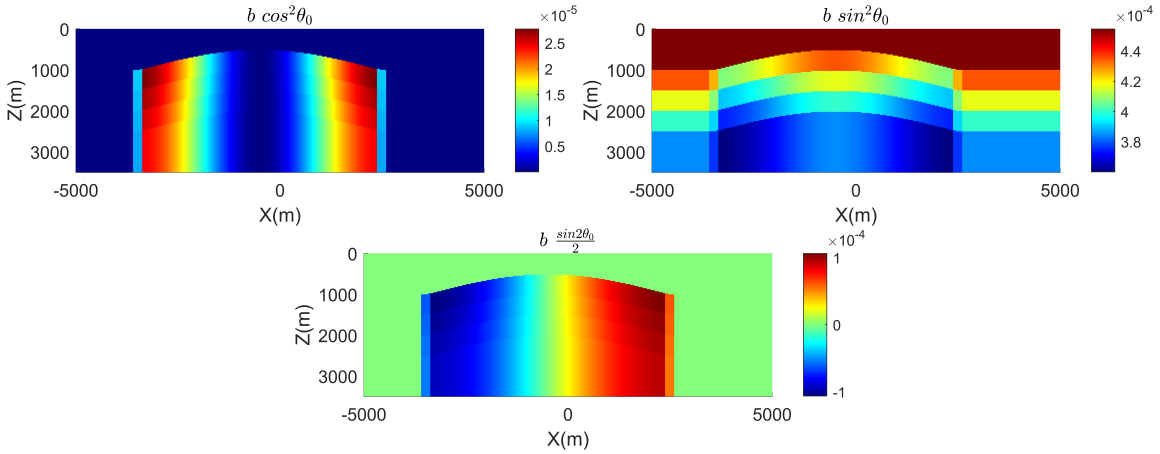

Fig. 4.14 Images of buoyancy tensor's elements obtained using the spatially varying tilt angle of the medium symmetry axis, where the angle is measured between the tangent to the interface with the vertical direction. The title of each image indicates the respective expression of the buoyancy tensor element.

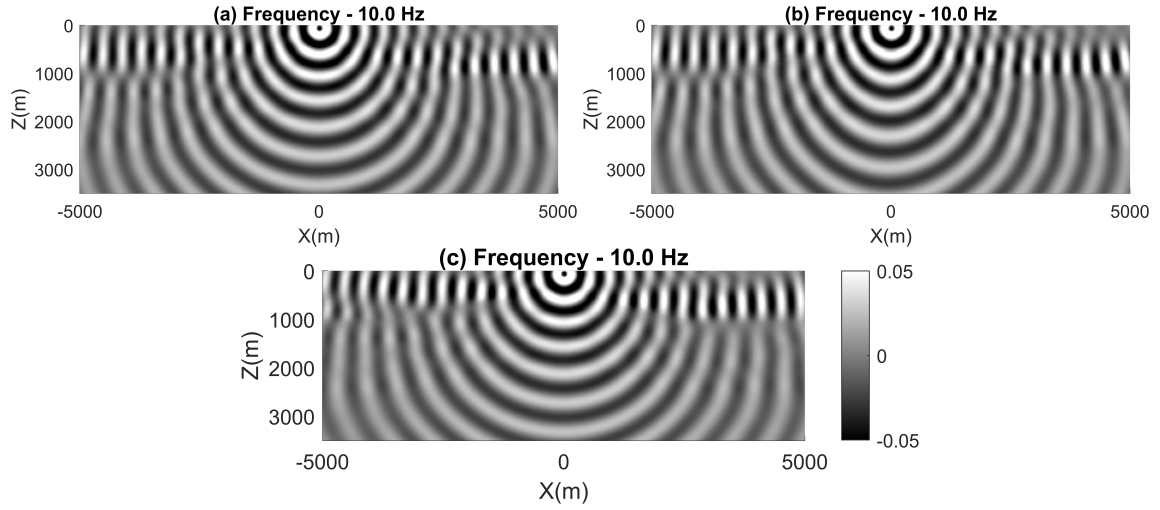

Fig. 4.15 Real part of pressure wavefield in the frequency domain for heterogeneous subsurfaces due to 10 Hz frequency monochromatic source; (a) for the isotropic model; (b) for the TTI model where the direction of the symmetry axis is taken as tangential to the interface; (c) for the TTI model where the direction of the symmetry axis is considered as perpendicular to the interface.

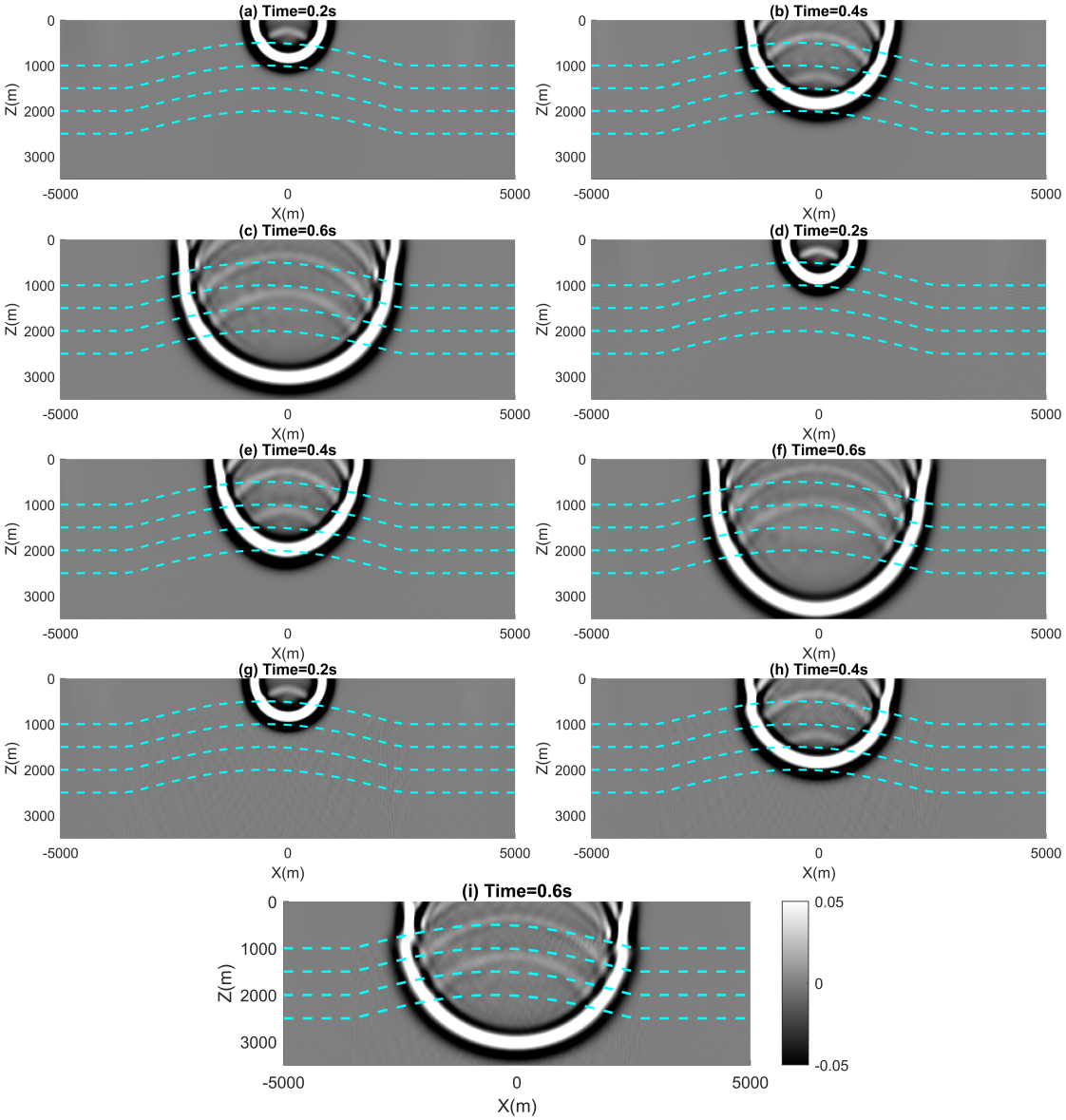

Fig. 4.16 Pressure wavefield in the time domain for heterogeneous subsurfaces using a 10 Hz dominant frequency Ricker wavelet as a source; (a) to (c) pressure wavefield for the isotropic model; (d) to (f) pressure wavefield for the TTI model where the direction of the symmetry axis is taken as tangential to the interface; (g) to (i) pressure wavefield for the TTI model where the direction of the symmetry axis is considered as perpendicular to the interface. The dashed cyan color curves denote the interfaces of different litho units.

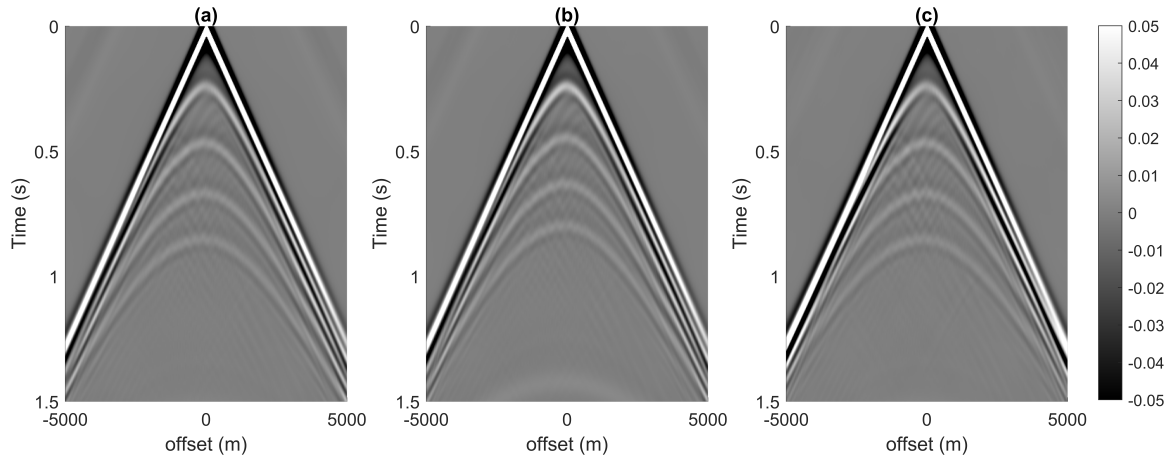

Fig. 4.17 Simulated shot-point gathers for heterogeneous subsurfaces using a 10 Hz dominant frequency Ricker wavelet as a source; (a) for the isotropic model; (b) for the TTI model where the direction of the symmetry axis is taken as tangential to the interface; (c) for the TTI model where the direction of the symmetry axis is considered as perpendicular to the interface.

4.5 Conclusion

We have developed an algorithm for 2D acoustic wave simulation in anisotropic media based on a support-operator finite-difference technique. The algorithm leads to a nine-point stencil discretization of the model. The accuracy of the modeled amplitude is benchmarked using an isotropic whole-space model. For the vertical transverse isotropic case, the simulated P-wave wavefront agrees well with the analytical simulation for both weak and strong anisotropic experiments. The tilted transverse isotropic media modeling also matched well with the analytical wavefront. The S-wave artifacts are observed in an anisotropic model with a similar character reported in the literature. The developed algorithm also experimented with a heterogeneous isotropic model and a tilted transverse isotropic model having a spatially varying tilt angle of the medium symmetry axis to examine its modeling capability. The benchmarking study presented using numerical experiments demonstrates the reliability and accuracy of the proposed method for acoustic wave simulation for anisotropic models.

Chapter 5

Conclusion and future possibilities

The research presented in this thesis has laid a robust foundation for the development of advanced geophysical inversion techniques, particularly focusing on the integration of seismic and controlled-source electromagnetic (CSEM) data. First, a space-domain forward modelling algorithm for two-dimensional (2D) CSEM data is devised. The efficiency of forward modelling is ensured using new boundary conditions specified at the plane perpendicular to the strike direction that intersects the transmitter position. These conditions leverage the symmetric and antisymmetric properties of the electromagnetic field components concerning the specified plane. A comparison of the simulated responses with the published algorithm results exhibits that approximately eight grids are adequate for spatial discretisation in the strike direction, ensuring the numerical accuracy needed for electromagnetic data simulation. A novel 2D CSEM inverse modelling algorithm is developed employing a space domain approach for both forward and adjoint field computation. Subsequently, these fields are used for the computation of the Jacobian matrix, which is utilised for gradient and Hessian calculation. A Gauss-Newton scheme is developed for iteratively updating the model parameters where the Hessian matrix is solved approximately using the conjugate gradient method. Inversion tests using synthetic and real field data also confirm that around eight grids are sufficient for discretisation in the strike direction, making the proposed algorithm highly efficient. A comparative study with a wavenumber domain 2D CSEM code (MARE2DEM) shows that the developed inversion algorithm is more than one order faster than MARE2DEM and also requires less memory.

A constrained inversion algorithm for 2D CSEM data is also developed by augmenting a cross-gradient-based regularisation functional in the above-mentioned algorithm. This algorithm integrates CSEM data with prior information obtained by other geophysical methods, leveraging structural details as a constraint to enhance the interpretative accuracy of the inversion process. The analysis carried out using the constrained inversion

algorithm provides useful knowledge about the benefits and limitations of the developed algorithm. It shows that structurally constrained inversion enhances the imaging of geological complex subsurfaces like salt domes. However, the inversion does not produce the sharp boundaries of anomalies due to smoothing constraints that seek a smooth model. An initial model based on prior knowledge can used to converge to global minima. However, the numerical experiment reveals that it is essential to exercise caution when creating such an initial model if faith in prior information is low. Further, the strategy of optimising the 2-norm of the difference between horizontal and vertical resistivity could enhance the imaging of geologically complex subsurface. However, prior knowledge about the anisotropy is required for such an application to obtain an artifacts-free inverted model.

We also developed a 2D acoustic wave simulation algorithm for anisotropic media using a support-operator finite-difference method, resulting in a nine-point stencil discretisation. The simulated P-wave wavefronts for vertical and tilted transverse isotropic cases matched well with analytical simulations. S-wave artifacts observed in the anisotropic model were consistent with those reported in the literature. Numerical experiments demonstrated the algorithm's reliability and accuracy in modelling heterogeneous isotropic and spatially varying tilted transversely isotropic media. The ability to accurately model anisotropic wave propagation is critical for improving the fidelity of seismic data interpretation, particularly in complex geological settings.

The work presented in this thesis represents a substantial advancement in the field of geophysical inversion, providing new tools and methodologies for more accurate and integrated subsurface imaging. These accomplishments not only contribute to the academic understanding of geophysical processes but also have practical implications for exploration geophysics, potentially leading to more effective resource exploration and development strategies. In future, the next phase of this research will focus on developing a 2D anisotropic seismic inversion algorithm. Since we have already developed an inversion framework for CSEM inversion and seismic modelling, the creation of a seismic inversion algorithm simply requires the integration of the inversion module with the seismic modelling code. We plan to work with the anisotropic properties of the subsurface for seismic data inversion as well. By accurately accounting for anisotropy in the inversion process, it is expected that the resulting subsurface models will exhibit improved resolution and reliability.

A key extension of future work will involve the simultaneous integration of seismic and CSEM results. This will be achieved by developing a simultaneous joint inversion algorithm designed to leverage the complementary strengths of both data types. The

integration process will build upon the constrained inversion techniques developed in the earlier phases of this research but will extend them to allow for the simultaneous inversion of both seismic and CSEM data. The development of this simultaneous joint inversion algorithm will involve several technical challenges. One of the primary challenges will be the effective handling of the different scales and resolutions of seismic and CSEM data. Additionally, the algorithm needs to be efficient in delivering the results in reasonable time frame.

The anticipated outcome of future work is a comprehensive and integrated inversion framework that can provide high-resolution, multi-parameter subsurface models using multiphysics data. Such a framework will not only enhance the understanding of subsurface geological structures but also improve the accuracy of resource exploration and characterization efforts. The simultaneous joint inversion of seismic and CSEM data represents a significant step forward in geophysical inversion methodologies, promising to deliver more detailed and reliable subsurface images. In summary, the research journey outlined in this thesis has achieved significant milestones in the development of advanced inversion techniques. The planned future work aims to build on these achievements, pushing the boundaries of what is possible in integrated geophysical inversion. By continuing to innovate and refine these methodologies, the ultimate goal is to provide more accurate and comprehensive tools for subsurface exploration and analysis.

References

Abedi, M. M. and Stovas, A. (2020). A new acoustic assumption for orthorhombic media. *Geophysical Journal International*, 223(2):1118–1129.

Abubakar, A., Habashy, T., Druskin, V., Knizhnerman, L., and Alumbaugh, D. (2008). 2.5 d forward and inverse modeling for interpreting low-frequency electromagnetic measurements. *Geophysics*, 73(4):F165–F177.

Aki, K. and Richards, P. G. (2002). *Quantitative seismology*.

Alford, R., Kelly, K., and Boore, D. M. (1974). Accuracy of finite-difference modeling of the acoustic wave equation. *Geophysics*, 39(6):834–842.

Alkhalifah, T. (1998). Acoustic approximations for processing in transversely isotropic media. *Geophysics*, 63(2):623–631.

Alkhalifah, T. (2000). An acoustic wave equation for anisotropic media. *Geophysics*, 65(4):1239–1250.

Alkhalifah, T. (2003). An acoustic wave equation for orthorhombic anisotropy. *Geophysics*, 68(4):1169–1172.

Alterman, Z. and Karal Jr, F. (1968). Propagation of elastic waves in layered media by finite difference methods. *Bulletin of the Seismological Society of America*, 58(1):367–398.

Amundsen, L., Løseth, L., Mittet, R., Ellingsrud, S., and Ursin, B. (2006). Decomposition of electromagnetic fields into upgoing and downgoing components. *Geophysics*, 71(5):G211–G223.

Anderson, C. and Mattson, J. (2010). An integrated approach to marine electromagnetic surveying using a towed streamer and source. *First Break*, 28(5).

Anderson, W. L. (1989). A hybrid fast hankel transform algorithm for electromagnetic modeling. *Geophysics*, 54(2):263–266.

Auken, E., Christiansen, A. V., Jacobsen, B. H., Foged, N., and Sørensen, K. I. (2005). Piecewise 1d laterally constrained inversion of resistivity data. *Geophysical Prospecting*, 53(4):497–506.

Avdeev, D. and Avdeeva, A. (2009). 3d magnetotelluric inversion using a limited-memory quasi-newton optimization. *Geophysics*, 74(3):F45–F57.

Avdeev, D. B., Kuvshinov, A. V., Pankratov, O. V., and Newman, G. A. (2002). Three-dimensional induction logging problems, part i: An integral equation solution and model comparisons. *Geophysics*, 67(2):413–426.

Berenger, J.-P. (1994). A perfectly matched layer for the absorption of electromagnetic waves. *Journal of computational physics*, 114(2):185–200.

Bergmann, T., Robertsson, J. O., and Holliger, K. (1996). Numerical properties of staggered finite-difference solutions of maxwell's equations for ground-penetrating radar modeling. *Geophysical Research Letters*, 23(1):45–48.

Besheli, S. A., Urosevic, M., and Li, R. (2005). The effect of seismic anisotropy on reservoir characterization. In *SEG International Exposition and Annual Meeting*, pages SEG–2005. SEG.

Bhuyian, A. H., Landrø, M., and Johansen, S. E. (2012). 3d csem modeling and time-lapse sensitivity analysis for subsurface co 2 storage. *Geophysics*, 77(5):E343–E355.

Boore, D. M. (1970). Love waves in nonuniform wave guides: Finite difference calculations. *Journal of Geophysical Research*, 75(8):1512–1527.

Brossier, R., Virieux, J., and Operto, S. (2008). Parsimonious finite-volume frequency-domain method for 2-dp–sv-wave modelling. *Geophysical Journal International*, 175(2):541–559.

Cai, H., Hu, X., Li, J., Endo, M., and Xiong, B. (2017). Parallelized 3d csem modeling using edge-based finite element with total field formulation and unstructured mesh. *Computers & Geosciences*, 99:125–134.

Cai, H., Liu, M., Zhou, J., Li, J., and Hu, X. (2022). Effective 3d-transient electromagnetic inversion using finite-element method with a parallel direct solver. *Geophysics*, 87(6):E377–E392.

Carcione, J. M., Kosloff, D., and Kosloff, R. (1988). Wave-propagation simulation in an elastic anisotropic (transversely isotropic) solid. *The Quarterly Journal of Mechanics and Applied Mathematics*, 41(3):319–346.

Castillo-Reyes, O., de la Puente, J., and Cela, J. M. (2018). Petgem: A parallel code for 3d csem forward modeling using edge finite elements. *Computers & Geosciences*, 119:123–136.

Chave, A. D. (1983). Numerical integration of related hankel transforms by quadrature and continued fraction expansion. *Geophysics*, 48(12):1671–1686.

Chen, J. and Hoversten, G. M. (2012). Joint inversion of marine seismic ava and csem data using statistical rock-physics models and markov random fields. *Geophysics*, 77(1):R65–R80.

Chesley, C., Naif, S., Key, K., and Bassett, D. (2021). Fluid-rich subducting topography generates anomalous forearc porosity. *Nature*, 595(7866):255–260.

Colombo, D. and De Stefano, M. (2007). Geophysical modeling via simultaneous joint inversion of seismic, gravity, and electromagnetic data: Application to prestack depth imaging. *The Leading Edge*, 26(3):326–331.

Colombo, D., Mantovani, M., Hallinan, S., and Virgilio, M. (2008). Sub-basalt depth imaging using simultaneous joint inversion of seismic and electromagnetic (mt) data: a crb field study. In *SEG Technical Program Expanded Abstracts 2008*, pages 2674–2678. Society of Exploration Geophysicists.

Constable, S. (2010). Ten years of marine csem for hydrocarbon exploration. *Geophysics*, 75(5):75A67–75A81.

Constable, S., Kannberg, P. K., and Weitemeyer, K. (2016). Vulcan: A deep-towed csem receiver. *Geochemistry, Geophysics, Geosystems*, 17(3):1042–1064.

Constable, S. C., Parker, R. L., and Constable, C. G. (1987). Occam's inversion: A practical algorithm for generating smooth models from electromagnetic sounding data. *Geophysics*, 52(3):289–300.

Cox, C. S. (1981). On the electrical conductivity of the oceanic lithosphere. *Physics of the Earth and Planetary Interiors*, 25(3):196–201.

Crase, E. (1990). High-order (space and time) finite-difference modeling of the elastic wave equation. In *SEG Technical Program Expanded Abstracts 1990*, pages 987–991. Society of Exploration Geophysicists.

da Silva, N. V., Morgan, J. V., MacGregor, L., and Warner, M. (2012). A finite element multifrontal method for 3d csem modeling in the frequency domain. *Geophysics*, 77(2):E101–E115.

De Basabe, J. D. and Sen, M. K. (2007). Grid dispersion and stability criteria of some common finite-element methods for acoustic and elastic wave equations. *Geophysics*, 72(6):T81–T95.

De Basabe, J. D. and Sen, M. K. (2010). Stability of the high-order finite elements for acoustic or elastic wave propagation with high-order time stepping. *Geophysical Journal International*, 181(1):577–590.

deGroot Hedlin, C. and Constable, S. (1990). Occam's inversion to generate smooth, two-dimensional models from magnetotelluric data. *Geophysics*, 55(12):1613–1624.

Dehiya, R. (2021). 3d forward modeling of controlled-source electromagnetic data based on the radiation boundary method. *Geophysics*, 86(2):E143–E155.

Dehiya, R. (2024). Error propagation and model update analysis in three-dimensional csem inversion. *Geophysical Journal International*, 238(3):1807–1824.

Dehiya, R., Singh, A., Gupta, P. K., and Israil, M. (2017). Optimization of computations for adjoint field and jacobian needed in 3d csem inversion. *Journal of Applied Geophysics*, 136:444–454.

Dormy, E. and Tarantola, A. (1995). Numerical simulation of elastic wave propagation using a finite volume method. *Journal of Geophysical Research: Solid Earth*, 100(B2):2123–2133.

Dumbser, M. and Käser, M. (2006). An arbitrary high-order discontinuous galerkin method for elastic waves on unstructured meshes—ii. the three-dimensional isotropic case. *Geophysical Journal International*, 167(1):319–336.

Ely, G. P., Day, S. M., and Minster, J.-B. (2008). A support-operator method for viscoelastic wave modelling in 3-d heterogeneous media. *Geophysical Journal International*, 172(1):331–344.

Engebretsen, K. W., Zhang, B., Fiandaca, G., Madsen, L. M., Auken, E., and Christiansen, A. V. (2022). Accelerated 2.5-d inversion of airborne transient electromagnetic data using reduced 3-d meshing. *Geophysical Journal International*, 230(1):643–653.

Etgen, J. T. and O'Brien, M. J. (2007). Computational methods for large-scale 3d acoustic finite-difference modeling: A tutorial. *Geophysics*, 72(5):SM223–SM230.

Evans, R. L. (2007). Using csem techniques to map the shallow section of seafloor: From the coastline to the edges of the continental slope. *Geophysics*, 72(2):WA105–WA116.

Faccioli, E., Maggio, F., Quarteroni, A., and Taghan, A. (1996). Spectral-domain decomposition methods for the solution of acoustic and elastic wave equations. *Geophysics*, 61(4):1160–1174.

Fomenko, E. Y. and Mogi, T. (2002). A new computation method for a staggered grid of 3d em field conservative modeling. *Earth, planets and space*, 54:499–509.

Gabrielsen, P. T., Brevik, I., Mittet, R., and Løseth, L. O. (2009). Investigating the exploration potential for 3d csem using a calibration survey over the troll field. *First Break*, 27(6).

Galis, M., Moczo, P., and Kristek, J. (2008). A 3-d hybrid finite-difference—finite-element viscoelastic modelling of seismic wave motion. *Geophysical Journal International*, 175(1):153–184.

Gallardo, L., Fontes, S., Meju, M., Buonora, M., and De Lugao, P. (2012). Robust geophysical integration through structure-coupled joint inversion and multispectral fusion of seismic reflection, magnetotelluric, magnetic, and gravity images: Example from santos basin, offshore brazil. *Geophysics*, 77(5):B237–B251.

Gallardo, L. A. and Meju, M. A. (2003). Characterization of heterogeneous near-surface materials by joint 2d inversion of dc resistivity and seismic data. *Geophysical Research Letters*, 30(13).

Gallardo, L. A. and Meju, M. A. (2004). Joint two-dimensional dc resistivity and seismic travel time inversion with cross-gradients constraints. *Journal of Geophysical Research: Solid Earth*, 109(B3).

Gao, K., Fu, S., and Chung, E. T. (2018). A high-order multiscale finite-element method for time-domain acoustic-wave modeling. *Journal of Computational Physics*, 360:120–136.

Gribenko, A., Green, A. M., Cuma, M., and Zhdanov, M. S. (2010). Efficient 3d inversion of mt data using integral equations method and the receiver footprint approach: Application to the large-scale inversion of the earthscope mt data. In *SEG International Exposition and Annual Meeting*, pages SEG–2010. SEG.

Gribenko, A. and Zhdanov, M. (2007). Rigorous 3d inversion of marine csem data based on the integral equation method. *Geophysics*, 72(2):WA73–WA84.

Günther, T., Rücker, C., and Spitzer, K. (2006). Three-dimensional modelling and inversion of dc resistivity data incorporating topography—ii. inversion. *Geophysical Journal International*, 166(2):506–517.

Gyrya, V. and Lipnikov, K. (2012). M-adaptation method for acoustic wave equation on square meshes. *Journal of Computational Acoustics*, 20(04):1250022.

Haber, E. (2004). Quasi-newton methods for large-scale electromagnetic inverse problems. *Inverse problems*, 21(1):305.

Haber, E. and Holtzman Gazit, M. (2013). Model fusion and joint inversion. *Surveys in Geophysics*, 34:675–695.

Halbouty, M. T. (1992). *Giant oil and gas fields of the decade 1978-1988*. American Association of petroleum geologists.

Harris, P. and MacGregor, L. (2006). Determination of reservoir properties from the integration of csem, seismic, and well-log data. *First Break*, 24(11).

He, Z., Hu, Z., Luo, W., and Wang, C. (2010). Mapping reservoirs based on resistivity and induced polarization derived from continuous 3d magnetotelluric profiling: Case study from qaidam basin, china. *Geophysics*, 75(1):B25–B33.

Heincke, B., Jegen, M., and Hobbs, R. (2006). Joint inversion of mt, gravity and seismic data applied to sub-basalt imaging. In *SEG Technical Program Expanded Abstracts 2006*, pages 784–789. Society of Exploration Geophysicists.

Heincke, B., Jegen, M., Moorkamp, M., Hobbs, R. W., and Chen, J. (2017). An adaptive coupling strategy for joint inversions that use petrophysical information as constraints. *Journal of Applied Geophysics*, 136:279–297.

Higdon, R. L. (1991). Absorbing boundary conditions for elastic waves. *Geophysics*, 56(2):231–241.

Hoversten, G. M., Cassassuce, F., Gasperikova, E., Newman, G. A., Chen, J., Rubin, Y., Hou, Z., and Vasco, D. (2006). Direct reservoir parameter estimation using joint inversion of marine seismic ava and csem data. *Geophysics*, 71(3):C1–C13.

Hoversten Jr, G., Newman Jr, G., Morrison Jr, H., Gasperikova Jr, E., and Berg Jr, J.-I. (2001). Reservoir characterization using crosswell electromagnetic inversion: A feasibility study for the snorre field, north sea. *Geophysics*, 66(4):1177–1189.

Hustedt, B., Operto, S., and Virieux, J. (2004). Mixed-grid and staggered-grid finite-difference methods for frequency-domain acoustic wave modelling. *Geophysical Journal International*, 157(3):1269–1296.

Igel, H., Mora, P., and Riollet, B. (1995). Anisotropic wave propagation through finite-difference grids. *Geophysics*, 60(4):1203–1216.

Ikelle, L. T. and Amundsen, L. (2018). *Introduction to petroleum seismology*. Society of Exploration Geophysicists.

Jo, C.-H., Shin, C., and Suh, J. H. (1996). An optimal 9-point, finite-difference, frequency-space, 2-d scalar wave extrapolator. *Geophysics*, 61(2):529–537.

Käser, M. and Dumbser, M. (2006). An arbitrary high-order discontinuous galerkin method for elastic waves on unstructured meshes—i. the two-dimensional isotropic case with external source terms. *Geophysical Journal International*, 166(2):855–877.

Key, K. (2016). Mare2dem: a 2-d inversion code for controlled-source electromagnetic and magnetotelluric data. *Geophysical Journal International*, 207(1):571–588.

Key, K. and Ovall, J. (2011). A parallel goal-oriented adaptive finite element method for 2.5-d electromagnetic modelling. *Geophysical Journal International*, 186(1):137–154.

Komatitsch, D., Coutel, F., and Mora, P. (1996). Tensorial formulation of the wave equation for modelling curved interfaces. *Geophysical Journal International*, 127(1):156–168.

Komatitsch, D. and Tromp, J. (2003). A perfectly matched layer absorbing boundary condition for the second-order seismic wave equation. *Geophysical Journal International*, 154(1):146–153.

Komatitsch, D. and Vilotte, J.-P. (1998). The spectral element method: an efficient tool to simulate the seismic response of 2d and 3d geological structures. *Bulletin of the seismological society of America*, 88(2):368–392.

Kong, F., Johnstad, S., Røsten, T., and Westerdahl, H. (2008). A 2.5 d finite-element-modeling difference method for marine csem modeling in stratified anisotropic media. *Geophysics*, 73(1):F9–F19.

Kosloff, D. D. and Baysal, E. (1982). Forward modeling by a fourier method. *Geophysics*, 47(10):1402–1412.

Lampe, B., Holliger, K., and Green, A. G. (2003). A finite-difference time-domain simulation tool for ground-penetrating radar antennas. *Geophysics*, 68(3):971–987.

Li, B. and Stovas, A. (2021). Decoupled approximation and separate extrapolation of p-and sv-waves in transversely isotropic media. *Geophysics*, 86(4):C133–C142.

Li, G., Duan, S., Cai, H., Han, B., and Ye, Y. (2020). An improved interpolation scheme at receiver positions for 2.5 d frequency-domain marine controlled-source electromagnetic forward modelling. *Geophysical Prospecting*, 68(5):1657–1675.

Li, Z., Wang, B., Xu, W., Mason, C., Yoon, K., and Rodriguez, G. (2008). Impacts of seismic anisotropy and subsalt velocity updates in imaging, deepwater gulf of mexico. In *SEG International Exposition and Annual Meeting*, pages SEG–2008. SEG.

Linde, N., Binley, A., Tryggvason, A., Pedersen, L. B., and Revil, A. (2006). Improved hydrogeophysical characterization using joint inversion of cross-hole electrical resistance and ground-penetrating radar traveltime data. *Water Resources Research*, 42(12).

Liu, J., Xiao, X., Tang, J., Zhou, C., Li, Y., Zhou, F., Pang, C., Zhou, S., and Wang, H. (2024). 3d structurally constrained inversion of the controlled-source electromagnetic data using octree meshes. *IEEE Transactions on Geoscience and Remote Sensing*.

Liu, Y. and Sen, M. K. (2010). A hybrid scheme for absorbing edge reflections in numerical modeling of wave propagation. *Geophysics*, 75(2):A1–A6.

Liu, Y. and Yin, C. (2016). 3d inversion for multipulse airborne transient electromagnetic data. *Geophysics*, 81(6):E401–E408.

Long, Z., Cai, H., Hu, X., Zhou, J., and Yang, X. (2024). 3d inversion of csem data using finite element method in data space. *IEEE Transactions on Geoscience and Remote Sensing*.

Lysmer, J. and Drake, L. (1972). Evolving geometrical and material properties of fault zones in a damage rheology model. *Methods in Computational Physics II: Seismology*, pages 181–216.

Ma, X., Zhou, J., Li, J., Zhang, J., Han, C., Guo, L., Li, S., and Mao, D. (2024). Image-guided structure-constrained inversion of electrical resistivity data for improving contaminations characterization. *Computers & Geosciences*, 185:105545.

MacGregor, L., Sinha, M., and Constable, S. (2001). Electrical resistivity structure of the valu fa ridge, lau basin, from marine controlled-source electromagnetic sounding. *Geophysical Journal International*, 146(1):217–236.

Mackie, R. L., Smith, J. T., and Madden, T. R. (1994). Three-dimensional electromagnetic modeling using finite difference equations: The magnetotelluric example. *Radio Science*, 29(4):923–935.

Maday, Y. and Patera, A. T. (1989). Spectral element methods for the incompressible navier-stokes equations. *IN: State-of-the-art surveys on computational mechanics (A90-47176 21-64). New York*, pages 71–143.

Malinverno, A. (2002). Parsimonious bayesian markov chain monte carlo inversion in a nonlinear geophysical problem. *Geophysical Journal International*, 151(3):675–688.

Marfurt, K. J. (1984a). Accuracy of finite-difference and finite-element modeling of the scalar and elastic wave equations. *Geophysics*, 49(5):533–549.

Marfurt, K. J. (1984b). Seismic modeling: a frequency-domain/finite-element approach. In *SEG Technical Program Expanded Abstracts 1984*, pages 633–634. Society of Exploration Geophysicists.

Martí, A. (2014). The role of electrical anisotropy in magnetotelluric responses: from modelling and dimensionality analysis to inversion and interpretation. *Surveys in Geophysics*, 35:179–218.

Mcgillivray, P. R. and Oldenburg, D. (1990). Methods for calculating fréchet derivatives and sensitivities for the non-linear inverse problem: A comparative study 1. *Geophysical prospecting*, 38(5):499–524.

Mehra, R., Raghuvanshi, N., Savioja, L., Lin, M. C., and Manocha, D. (2012). An efficient gpu-based time domain solver for the acoustic wave equation. *Applied Acoustics*, 73(2):83–94.

Meju, M. A. and Gallardo, L. A. (2016). Structural coupling approaches in integrated geophysical imaging. *Integrated imaging of the earth: Theory and applications*, pages 49–67.

Meju, M. A., Gallardo, L. A., and Mohamed, A. K. (2003). Evidence for correlation of electrical resistivity and seismic velocity in heterogeneous near-surface materials. *Geophysical research letters*, 30(7).

Meju, M. A., Mackie, R. L., Miorelli, F., Saleh, A. S., and Miller, R. V. (2019). Structurally tailored 3d anisotropic controlled-source electromagnetic resistivity inversion with cross-gradient criterion and simultaneous model calibration. *Geophysics*, 84(6):E387–E402.

Miller, R. V., Meju, M. A., Saleh, A. S., Mackie, R. L., and Miorelli, F. (2019). Structure-guided 3d joint inversion of csem and mt data from a fold-thrust belt. In *SEG International Exposition and Annual Meeting*, page D043S098R007. SEG.

Minsley, B. J. (2011). A trans-dimensional bayesian markov chain monte carlo algorithm for model assessment using frequency-domain electromagnetic data. *Geophysical Journal International*, 187(1):252–272.

Moczo, P., Kristek, J., Galis, M., and Pazak, P. (2010). On accuracy of the finite-difference and finite-element schemes with respect to p-wave to s-wave speed ratio. *Geophysical Journal International*, 182(1):493–510.

Nádasi, E., Gribenko, A. V., and Zhdanov, M. S. (2022). Large-scale inversion of magnetotelluric data using regularized gauss–newton method in the data space. *Pure and Applied Geophysics*, 179(10):3785–3806.

Operto, S., Virieux, J., Ribodetti, A., and Anderson, J. E. (2009). Finite-difference frequency-domain modeling of viscoacoustic wave propagation in 2d tilted transversely isotropic (tti) media. *Geophysics*, 74(5):T75–T95.

Panzner, M., Morten, J. P., Weibull, W. W., and Arntsen, B. (2016). Integrated seismic and electromagnetic model building applied to improve subbasalt depth imaging in the faroe-shetland basin. *Geophysics*, 81(1):E57–E68.

Patera, A. T. (1984). A spectral element method for fluid dynamics: laminar flow in a channel expansion. *Journal of computational Physics*, 54(3):468–488.

Payton, R. (1983). *Elastic wave propagation in transversely isotropic media*, volume 4. Springer Science & Business Media.

Peter, D., Komatitsch, D., Luo, Y., Martin, R., Le Goff, N., Casarotti, E., Le Loher, P., Magnoni, F., Liu, Q., Blitz, C., et al. (2011). Forward and adjoint simulations of seismic wave propagation on fully unstructured hexahedral meshes. *Geophysical Journal International*, 186(2):721–739.

Plessix, R.-E. (2007). A helmholtz iterative solver for 3d seismic-imaging problems. *Geophysics*, 72(5):SM185–SM194.

Pratt, R. G. (1990). Frequency-domain elastic wave modeling by finite differences: A tool for crosshole seismic imaging. *Geophysics*, 55(5):626–632.

Pratt, R. G. and Worthington, M. H. (1990). Inverse theory applied to multi-source cross-hole tomography. part 1: Acoustic wave-equation method 1. *Geophysical prospecting*, 38(3):287–310.

Priolo, E., Carcione, J. M., and Seriani, G. (1994). Numerical simulation of interface waves by high-order spectral modeling techniques. *The Journal of the Acoustical Society of America*, 95(2):681–693.

Ricker, N. H. (1940). The form and nature of seismic waves and the structure of seismograms. *Geophysics*, 5(4):348–366.

Robertsson, J. O., Blanch, J. O., Nihei, K., and Tromp, J. (2012). *Numerical modeling of seismic wave propagation: Gridded two-way wave-equation methods*. Society of Exploration Geophysicists.

Robertsson, J. O., Blanch, J. O., and Symes, W. W. (1994). Viscoelastic finite-difference modeling. *Geophysics*, 59(9):1444–1456.

Rodi, W. and Mackie, R. L. (2001). Nonlinear conjugate gradients algorithm for 2-d magnetotelluric inversion. *Geophysics*, 66(1):174–187.

Saenger, E. H. and Bohlen, T. (2004). Finite-difference modeling of viscoelastic and anisotropic wave propagation using the rotated staggered grid. *Geophysics*, 69(2):583–591.

Samarskii, A., Tishkin, V., Favorskii, A., and Shashkov, M. Y. (1981). Operational finite-difference schemes. *Differential Equations*, 17(7):854–862.

Sambridge, M. and Mosegaard, K. (2002). Monte carlo methods in geophysical inverse problems. *Reviews of Geophysics*, 40(3):3–1.

Sasaki, Y. (1999). Three-dimensional frequency-domain electromagnetic modeling using the finite-difference method; sabunho ni yoru shuhasu ryoiki denji tansaho no sanjigen moderingu. *Butsuri Tansa (Geophysical Exploration)*, 52.

Sasaki, Y. (2001). Full 3-d inversion of electromagnetic data on pc. *Journal of Applied Geophysics*, 46(1):45–54.

Saunders, J., Herwanger, J., Pain, C., Worthington, M., and De Oliveira, C. (2005). Constrained resistivity inversion using seismic data. *Geophysical Journal International*, 160(3):785–796.

Schenk, O. and Gärtner, K. (2004). Solving unsymmetric sparse systems of linear equations with pardiso. *Future Generation Computer Systems*, 20(3):475–487.

Schlue, J. (1979). Finite element matrices for seismic surface waves in three-dimensional structures. *Bulletin of the Seismological Society of America*, 69(5):1425–1438.

Schwalenberg, K., Haeckel, M., Poort, J., and Jegen, M. (2010). Evaluation of gas hydrate deposits in an active seep area using marine controlled source electromagnetics: Results from opouawe bank, hikurangi margin, new zealand. *Marine Geology*, 272(1-4):79–88.

Seriani, G. and Oliveira, S. (2008). Dispersion analysis of spectral element methods for elastic wave propagation. *Wave motion*, 45(6):729–744.

Seriani, G. and Priolo, E. (1994). Spectral element method for acoustic wave simulation in heterogeneous media. *Finite elements in analysis and design*, 16(3-4):337–348.

Serón, F., Sanz, F., Kindelan, M., and Badal, J. (1990). Finite-element method for elastic wave propagation. *Communications in applied numerical methods*, 6(5):359–368.

Shashkov, M. (2018). *Conservative finite-difference methods on general grids*. CRC press.

Shi, L., Zhou, Y., Wang, J.-M., Zhuang, M., Liu, N., and Liu, Q. H. (2016). Spectral element method for elastic and acoustic waves in frequency domain. *Journal of Computational Physics*, 327:19–38.

Shin, C. and Sohn, H. (1998). A frequency-space 2-d scalar wave extrapolator using extended 25-point finite-difference operator. *Geophysics*, 63(1):289–296.

Singh, A. and Dehiya, R. (2022). An efficient em modeling scheme for large 3-d models—a magnetotelluric case study. *IEEE Transactions on Geoscience and Remote Sensing*, 61:1–11.

Sinha, M. (1999). Controlled source em sounding: survey design considerations for hydrocarbon applications. *LITHOS Science Report Apr*, 199(1):95–101.

Siripunvaraporn, W. and Egbert, G. (2000). An efficient data-subspace inversion method for 2-d magnetotelluric data. *Geophysics*, 65(3):791–803.

Siripunvaraporn, W., Egbert, G., and Lenbury, Y. (2002). Numerical accuracy of magnetotelluric modeling: a comparison of finite difference approximations. *Earth, planets and space*, 54:721–725.

Siripunvaraporn, W., Egbert, G., Lenbury, Y., and Uyeshima, M. (2005). Three-dimensional magnetotelluric inversion: data-space method. *Physics of the Earth and planetary interiors*, 150(1-3):3–14.

Smith, J. T. (1996). Conservative modeling of 3-d electromagnetic fields, part i: Properties and error analysis. *Geophysics*, 61(5):1308–1318.

Spitzer, K. (2024). Electromagnetic modeling using adaptive grids–error estimation and geometry representation. *Surveys in Geophysics*, 45(1):277–314.

Stovas, A., Roganov, Y., and Roganov, V. (2021). Pure mode p-and s-wave phase velocity equations in elastic orthorhombic media. *Geophysics*, 86(5):C143–C156.

Streich, R. (2009). 3d finite-difference frequency-domain modeling of controlled-source electromagnetic data: Direct solution and optimization for high accuracy. *Geophysics*, 74(5):F95–F105.

Tadi, M. (2004). Finite volume method for 2d elastic wave propagation. *Bulletin of the Seismological Society of America*, 94(4):1500–1509.

Tarantola, A. (2005). *Inverse problem theory and methods for model parameter estimation*. SIAM.

Tessmer, E., Kosloff, D., and Behle, A. (1992). Elastic wave propagation simulation in the presence of surface topography. *Geophysical Journal International*, 108(2):621–632.

Thomsen, L. (1986). Weak elastic anisotropy. *Geophysics*, 51(10):1954–1966.

Thomsen, L. (2014). *Understanding seismic anisotropy in exploration and exploitation*. Society of Exploration Geophysicists.

Virieux, J. (1984). Sh-wave propagation in heterogeneous media: Velocity-stress finite-difference method. *Geophysics*, 49(11):1933–1942.

Virieux, J. (1986). P-sv wave propagation in heterogeneous media: Velocity-stress finite-difference method. *Geophysics*, 51(4):889–901.

Wang, B., Liu, J., Hu, X., Liu, J., Guo, Z., and Xiao, J. (2021). Geophysical electromagnetic modeling and evaluation: a review. *Journal of Applied Geophysics*, 194:104438.

Wang, F., Morten, J. P., and Spitzer, K. (2018). Anisotropic three-dimensional inversion of csem data using finite-element techniques on unstructured grids. *Geophysical Journal International*, 213(2):1056–1072.

Ward, S. H., Hohmann, G. W., and Nabighian, M. (1988). Electromagnetic methods in applied geophysics. *Tulsa, Oklahoma, USA*, 1:131–312.

Weiss, C. J. (2007). The fallacy of the "shallow-water problem" in marine csem exploration. *Geophysics*, 72(6):A93–A97.

Weiss, C. J. and Constable, S. (2006). Mapping thin resistors and hydrocarbons with marine em methods, part ii—modeling and analysis in 3d. *Geophysics*, 71(6):G321–G332.

Weitemeyer, K., Gao, G., Constable, S., and Alumbaugh, D. (2010). The practical application of 2d inversion to marine controlled-source electromagnetic data. *Geophysics*, 75(6):F199–F211.

Wheelock, B., Constable, S., and Key, K. (2015). The advantages of logarithmically scaled data for electromagnetic inversion. *Geophysical Journal International*, 201(3):1765–1780.

Williamson, P. R. and Pratt, R. G. (1995). A critical review of acoustic wave modeling procedures in 2.5 dimensions. *Geophysics*, 60(2):591–595.

Wu, S., Huang, Q., and Zhao, L. (2023). Fast bayesian inversion of airborne electromagnetic data based on the invertible neural network. *IEEE Transactions on Geoscience and Remote Sensing*, 61:1–11.

Wu, Z., Fan, Y., Wang, J., Zhang, R., and Liu, Q. H. (2019). Application of 2.5-d finite difference method in logging-while-drilling electromagnetic measurements for complex scenarios. *IEEE Geoscience and Remote Sensing Letters*, 17(4):577–581.

Xiao, L., Fiandaca, G., Zhang, B., Auken, E., and Christiansen, A. V. (2022). Fast 2.5 d and 3d inversion of transient electromagnetic surveys using the octree-based finite-element method. *Geophysics*, 87(4):E267–E277.

Xu, S., Stovas, A., Alkhalifah, T., and Mikada, H. (2020). New acoustic approximation for transversely isotropic media with a vertical symmetry axis. *Geophysics*, 85(1):C1–C12.

Xue, G., He, Y., Chen, W., Wu, X., and Song, W. (2023). 3-d inversion based on the particle swarm optimization-quasi-newton hybrid algorithm for sotem. *IEEE Transactions on Geoscience and Remote Sensing*, 61:1–11.

Yavich, N. and Zhdanov, M. S. (2020). Finite-element em modelling on hexahedral grids with an fd solver as a pre-conditioner. *Geophysical Journal International*, 223(2):840–850.

Yee, K. (1966). Numerical solution of initial boundary value problems involving maxwell's equations in isotropic media. *IEEE Transactions on antennas and propagation*, 14(3):302–307.

Zeng, S., Chen, F., Li, D., Chen, J., and Chen, J. (2018). A novel 2.5 d finite difference scheme for simulations of resistivity logging in anisotropic media. *Journal of Applied Geophysics*, 150:144–152.

Zhou, H., Zhang, G., and Bloor, R. (2006). An anisotropic acoustic wave equation for vti media. In *68th EAGE Conference and Exhibition incorporating SPE EUROPEC 2006*, pages cp–2. European Association of Geoscientists & Engineers.

Zhou, J., Revil, A., Karaoulis, M., Hale, D., Doetsch, J., and Cuttler, S. (2014). Image-guided inversion of electrical resistivity data. *Geophysical Journal International*, 197(1):292–309.

Appendix A

Boundary conditions for HED$_x$

A.1 Boundary conditions

For HED$_x$ transmitter and using conductivity tensor given in equation (2.10), equations (2.4)–(2.9) can be written as,

$$\iota k_y E_z - \frac{\partial E_y}{\partial z} - \iota\omega\mu H_x = 0, \tag{A.1.1}$$

$$\frac{\partial E_x}{\partial z} - \frac{\partial E_z}{\partial x} - \iota\omega\mu H_y = 0, \tag{A.1.2}$$

$$\frac{\partial E_y}{\partial x} - \iota k_y E_x - \iota\omega\mu H_z = 0, \tag{A.1.3}$$

$$\iota k_y H_z - \frac{\partial H_y}{\partial z} - (\sigma_{xx} - \iota\omega\epsilon)E_x - \sigma_{xz}E_z = J_x^e \delta(x - x_s)\delta(z - z_s) \tag{A.1.4}$$

$$\frac{\partial H_x}{\partial z} - \frac{\partial H_z}{\partial x} - (\sigma_{yy} - \iota\omega\epsilon)E_y = 0, \tag{A.1.5}$$

$$\frac{\partial H_y}{\partial x} - \iota k_y H_x - \sigma_{zx}E_x - (\sigma_{zz} - \iota\omega\epsilon)E_z = 0 \tag{A.1.6}$$

Now substituting, k_y= -k_y, $E_y = -E_y$, $H_x = -H_x$ and $H_z = -H_z$ we observed that it leads to the same equation as give in equations (A.1.1)–(A.1.6). Therefore, the E_x, E_z, and H_y are even functions of k_y whereas E_y, H_x, and H_z are odd functions of k_y.

Appendix B

System matrix coefficients of MFDM scheme

B.1 Discretised form of differential operators for mimetic scheme

The expressions for coefficients of system matrix constructed using the support operator methods can be written as Shashkov (2018),

$$
\begin{aligned}
C_{i+1,j} = {} & ((z(i,j+1) - z(i+1,j)) * (\Theta_{xx}(i,j)/(2.0 * \Omega(i,j))) * \\
& (z(i,j) - z(i+1,j+1)) + (z(i+1,j) - z(i,j-1) * \\
& (\Theta_{xx}(i,j-1)/(2.0 * \Omega(i,j-1))) * (z(i+1,j-1) - z(i,j)) - \\
& (z(i,j+1) - z(i+1,j)) * (\Theta_{xz}(i,j)/(2.0 * \Omega(i,j))) * (x(i,j) - x(i+1,j+1)) - \\
& (z(i+1,j) - z(i,j-1)) * (\Theta_{xz}(i,j-1)/(2.0 * \Omega(i,j-1))) * (x(i+1,j-1) - x(i,j)) - \\
& (x(i,j+1) - x(i+1,j)) * (\Theta_{xz}(i,j)/(2.0 * \Omega(i,j))) * (z(i,j) - z(i+1,j+1)) - \\
& (x(i+1,j) - x(i,j-1)) * (\Theta_{xz}(i,j-1)/(2.0 * \Omega(i,j-1))) * (z(i+1,j-1) - z(i,j)) + \\
& (x(i,j+1) - x(i+1,j)) * (\Theta_{zz}(i,j)/(2.0 * \Omega(i,j))) * (x(i,j) - x(i+1,j+1) + \\
& (x(i+1,j) - x(i,j-1)) * (\Theta_{zz}(i,j-1)/(2.0 * \Omega(i,j-1))) * (x(i+1,j-1) - x(i,j)))/(2.0 * VN_{i,j}),
\end{aligned}
\tag{B.1.1}
$$

$$C_{i+1,j+1} = ((z(i,j+1) - z(i+1,j)) * (\Theta_{xx}(i,j)/(2.0 * \Omega(i,j))) * (z(i+1,j) - z(i,j+1)) -$$
$$(z(i,j+1) - z(i+1,j)) * (\Theta_{xz}(i,j)/(2.0 * \Omega(i,j))) * (x(i+1,j) - x(i,j+1)) -$$
$$(x(i,j+1) - x(i+1,j)) * (\Theta_{xz}(i,j)/(2.0 * \Omega(i,j))) * (z(i+1,j) - z(i,j+1)) +$$
$$(x(i,j+1) - x(i+1,j)) * (\Theta_{zz}(i,j)/(2.0 * \Omega(i,j))) * (x(i+1,j) - x(i.j+1)))/(2.0 * VN_{i,j}), \tag{B.1.2}$$

$$C_{i,j+1} = -((z(i,j+1) - z(i+1,j)) * (\Theta_{xx}(i,j)/(2.0 * \Omega(i,j))) *$$
$$(z(i,j) - z(i+1,j+1)) + (z(i-1,j) - z(i,j+1) *$$
$$(\Theta_{xx}(i-1,j)/(2.0 * \Omega(i-1,j))) * (z(i,j) - z(i-1,j-1)) +$$
$$(z(i,j+1) - z(i+1,j)) * (\Theta_{xz}(i,j)/(2.0 * \Omega(i,j))) * (x(i,j) - x(i+1,j+1)) -$$
$$(z(i-1,j) - z(i,j+1)) * (\Theta_{xz}(i-1,j)/(2.0 * \Omega(i-1,j))) * (x(i,j) - x(i-1,j+1)) +$$
$$(x(i,j+1) - x(i+1,j)) * (\Theta_{xz}(i,j)/(2.0 * \Omega(i,j))) * (z(i,j) - z(i+1,j+1)) -$$
$$(x(i-1,j) - x(i,j+1)) * (\Theta_{xz}(i-1,j)/(2.0 * \Omega(i-1,j))) * (z(i,j) - z(i-1,j+1)) -$$
$$(x(i,j+1) - x(i+1,j)) * (\Theta_{zz}(i,j)/(2.0 * \Omega(i,j))) * (x(i,j) - x(i+1,j+1)) +$$
$$(x(i-1,j) - x(i,j+1)) * (\Theta_{zz}(i-1,j)/(2.0 * \Omega(i-1,j))) * (x(i,j) - x(i-1,j+1)))/(2.0 * VN_{i,j}), \tag{B.1.3}$$

$$C_{i-1,j+1} = -((z(i-1,j) - z(i,j+1)) * (\Theta_{xx}(i-1,j)/(2.0 * \Omega(i-1,j))) * (z(i-1,j) - z(i,j+1)) +$$
$$(z(i-1,j) - z(i,j+1)) * (\Theta_{xz}(i-1,j)/(2.0 * \Omega(i-1,j))) * (x(i-1,j) - x(i,j+1)) +$$
$$(x(i-1,j) - x(i,j+1)) * (\Theta_{xz}(i-1,j)/(2.0 * \Omega(i-1,j))) * (z(i-1,j) - z(i,j+1)) -$$
$$(x(i-1,j) - x(i,j+1)) * (\Theta_{zz}(i-1,j)/(2.0 * \Omega(i-1,j))) * (x(i-1,j) - x(i.j+1)))/(2.0 * VN_{i,j}), \tag{B.1.4}$$

$$
\begin{aligned}
C_{i-1,j} = -((z(i-1,j) - z(i,j+1)) * (\Theta_{xx}(i-1,j)/(2.0 * \Omega(i-1,j))) * \\
(z(i,j) - z(i-1,j+1)) - (z(i,j-1) - z(i-1,j) * \\
(\Theta_{xx}(i-1,j-1)/(2.0 * \Omega(i-1,j-1))) * (z(i-1,j-1) - z(i,j)) + \\
(z(i-1,j) - z(i,j+1)) * (\Theta_{xz}(i-1,j)/(2.0 * \Omega(i-1,j))) * (x(i,j) - x(i-1,j+1)) + \\
(z(i,j-1) - z(i-1,j)) * (\Theta_{xz}(i-1,j-1)/(2.0 * \Omega(i-1,j-1))) * (x(i-1,j-1) - x(i,j)) + \\
(x(i-1,j) - x(i,j+1)) * (\Theta_{xz}(i-1,j-1)/(2.0 * \Omega(i-1,j-1))) * (z(i,j) - z(i-1,j+1)) + \\
(x(i,j-1) - x(i-1,j)) * (\Theta_{xz}(i-1,j-1)/(2.0 * \Omega(i-1,j-1))) * (z(i-1,j-1) - z(i,j)) - \\
(x(i-1,j) - x(i,j+1)) * (\Theta_{zz}(i-1,j)/(2.0 * \Omega(i-1,j))) * (x(i,j) - x(i-1,j+1) - \\
(x(i,j-1) - x(i-1,j)) * (\Theta_{zz}(i-1,j-1)/(2.0 * \Omega(i-1,j-1))) * (x(i-1,j-1) - x(i,j))) \\
/(2.0 * VN_{i,j}),
\end{aligned}
\tag{B.1.5}
$$

$$
\begin{aligned}
C_{i-1,j-1} = -((z(i,j-1) - z(i-1,j)) * (\Theta_{xx}(i-1,j-1) \\
/(2.0 * \Omega(i-1,j-1))) * (z(i,j-1) - z(i-1,j)) + \\
(z(i,j-1) - z(i-1,j)) * (\Theta_{xz}(i-1,j-1)/(2.0 * \Omega(i-1,j-1))) * (x(i,j-1) - x(i-1,j)) + \\
(x(i,j-1) - x(i-1,j)) * (\Theta_{xz}(i-1,j-1)/(2.0 * \Omega(i-1,j-1))) * (z(i,j-1) - z(i-1,j)) - \\
(x(i,j-1) - x(i-1,j)) * (\Theta_{zz}(i-1,j-1)/(2.0 * \Omega(i-1,j-1))) * (x(i,j-1) - x(i-1.j))) \\
/(2.0 * VN_{i,j}),
\end{aligned}
\tag{B.1.6}
$$

$$
\begin{aligned}
C_{i,j-1} = {} & ((z(i,j-1)-z(i-1,j))*(\Theta_{xx}(i-1,j-1)/(2.0*\Omega(i-1,j-1)))* \\
& (z(i-1,j-1)-z(i,j))-(z(i+1,j)-z(i,j-1)* \\
& (\Theta_{xx}(i,j-1)/(2.0*\Omega(i,j-1)))*(z(i+1,j-1)-z(i,j))- \\
& (z(i,j-1)-z(i-1,j))*(\Theta_{xz}(i-1,j-1)/(2.0*\Omega(i-1,j-1)))*(x(i-1,j-1)-x(i,j))+ \\
& (z(i+1,j)-z(i,j-1))*(\Theta_{xz}(i,j-1)/(2.0*\Omega(i,j-1)))*(x(i+1,j-1)-x(i,j))- \\
& (x(i,j-1)-x(i-1,j))*(\Theta_{xz}(i-1,j-1)/(2.0*\Omega(i-1,j-1)))*(z(i-1,j-1)-z(i,j))+ \\
& (x(i+1,j)-x(i,j-1))*(\Theta_{xz}(i,j-1)/(2.0*\Omega(i,j-1)))*(z(i+1,j-1)-z(i,j))+ \\
& (x(i+1,j)-x(i,j-1))*(\Theta_{zz}(i-1,j-1)/(2.0*\Omega(i-1,j-1)))*(x(i-1,j-1)-x(i,j)- \\
& (x(i+1,j)-x(i,j-1))*(\Theta_{zz}(i,j-1)/(2.0*\Omega(i,j-1)))*(x(i+1,j-1)-x(i,j)))/(2.0*VN_{i,j}),
\end{aligned}
\tag{B.1.7}
$$

$$
\begin{aligned}
C_{i-1,j+1} = {} & ((z(i+1,j)-z(i,j-1))*(\Theta_{xx}(i,j-1)/(2.0*\Omega(i,j-1)))*(z(i,j-1)-z(i+1,j))- \\
& (z(i+1,j)-z(i,j-1))*(\Theta_{xz}(i,j-1)/(2.0*\Omega(i,j-1)))*(x(i,j-1)-x(i+1,j))- \\
& (x(i+1,j)-x(i,j-1))*(\Theta_{xz}(i,j-1)/(2.0*\Omega(i,j-1)))*(z(i,j-1)-z(i+1,j))+ \\
& (x(i+1,j)-x(i,j-1))*(\Theta_{zz}(i,j-1)/(2.0*\Omega(i,j-1)))*(x(i,j-1)-x(i+1.j)))/(2.0*VN_{i,j}),
\end{aligned}
\tag{B.1.8}
$$

and

$$
C_{i,j} = -(C_{i+1,j}+C_{i-1,j}+C_{i,j-1}+C_{i,j+1}+C_{i+1,j-1}+C_{i-1,j-1}+C_{i-1,j+1}+C_{i+1,j+1}),
\tag{B.1.9}
$$